

AN ABSTRACT OF THE DISSERTATION OF

Tal Sharf for the degree of Doctor of Philosophy in Physics presented on August 27, 2014.

Title: Liquid-Gated Carbon Nanotube Transistor Noise Sources and Sensitivity Limits

Abstract approved: _____

Ethan D. Minot

Low-dimensional electronic materials offer a platform to observe biological processes with unprecedented spatial and temporal resolution. Carbon nanotubes (CNTs) are the closest physical analog to an ideal 1D system and can be scaled and integrated into multiplexed electronic circuitry. The molecular structure of a CNT is also biocompatible, making them an ideal platform to simultaneously interface and interrogate the biological world at the nanometer scale. The major theme of this dissertation is the investigation of the physical origins of electronic signals produced in CNT field-effect transistors (FETs) in physiological environments.

Electronic signals measured in CNT FET biosensors are the result of electrostatic changes in the environment surrounding the CNT. Biological molecules in close proximity to a CNT can dominate the local electrostatic landscape surrounding it. The activity of these biological molecules can in turn modulate electronic transport in 1D CNT systems.

The sensitivity of CNT FETs is ultimately limited by ever-present noise in the electrostatic environment. This noise is often due to the stochastic fluctuation of charge traps, which are inherent to nanometer scale material interfaces at ambient conditions. In order to push the detection limits of CNT FETs and

enhance our ability to resolve biological signals, we must first minimize this unwanted noise.

In order to probe the major sources of noise in CNT FETs, we have systematically controlled the environment surrounding a CNT. We quantify the noise generated by the substrate, surface adsorbates, and biological molecular interactions with a CNT's surface. We show that electrostatically induced disorder at the CNT interface is a significant source of parasitic noise. By removing the substrate interaction and surface adsorbates, we find a 19-fold reduction in the power spectrum of electronic noise. To further investigate the microscopic origins of noise, we examine a correlation between the protonation state of charged biological moieties at the CNT interface and the magnitude of electronic noise.

In some cases, the electrostatic perturbation generated by a single charge trap in close proximity to a CNT can dominate the noise in a CNT FET. The charge trap creates a scattering site in the CNT. When the trap is occupied, device conductance can be significantly reduced, leading to random telegraph signals (RTS), in constant-bias current. We experimentally and theoretically demonstrate that the amplitude of the RTS depends strongly on the Fermi energy and polarity of the free carriers. The high signal-to-noise ratio that we observe demonstrates that it is possible to detect the fields generated by the fluctuations of a single electron charge at room temperature.

©Copyright by Tal Sharf
August 27, 2014
All Rights Reserved

Liquid-Gated Carbon Nanotube Transistor Noise Sources and Sensitivity Limits

by
Tal Sharf

A DISSERTATION

submitted to

Oregon State University

in partial fulfillment of
the requirements for the
degree of

Doctor of Philosophy

Presented August 27, 2014

Commencement June 2015

Doctor of Philosophy dissertation of Tal Sharf presented on August 27, 2014

APPROVED:

Major Professor, representing Physics

Chair of the Department of Physics

Dean of the Graduate School

I understand that my dissertation will become part of the permanent collection of Oregon State University libraries. My signature below authorizes release of my dissertation to any reader upon request.

Tal Sharf, Author

CONTRIBUTION OF AUTHORS

Josh Kevek contributed to the device fabrication of suspended and surface-based carbon nanotube devices in Chapters 2-4. Tristan DeBorde performed scanning photocurrent measurements and Raman spectroscopy to identify single pristine suspended carbon nanotube circuits in Chapter 3. Neng-Ping Wang performed the theoretical scattering calculations in the carbon nanotube transistors for Chapter 4. Morgan Brown contributed to device fabrication and electrical measurements in Chapter 4. Heather Wilson contributed to the electrical measurements in Chapter 4. Ethan Minot provided insight, guidance and motivation for all aspects of the work presented in this dissertation.

TABLE OF CONTENTS

	<u>Page</u>
1. Introduction.....	1
1.1 Nanoscale biotechnology	2
1.2 Bioelectronic fields	2
1.3 Carbon nanotubed as bioelectronic probes	3
1.4 Liquid-gating and the electric double layer	5
1.5 Subthreshold swing.....	8
1.6 Sensitivity and noise	10
1.7 Johnson noise	11
1.8 Shot noise.....	12
1.9 $1/f$ noise.....	13
1.10 Length dependence of charge noise	15
1.11 Random telegraph signals.....	17
1.12 Graduate work not included in this thesis.....	18
1.13 References.....	22
2. Fabrication of low-noise carbon nanotube field effect transistors biosensors	26
2.1 Introduction.....	27
2.2 Biosensor fabrication	27
2.3 Electronic properties of a suspended CNT	32
2.4 Summary and conclusion.....	36
2.5 Acknowledgements.....	36
2.6 References.....	37
3. Origins of charge noise in carbon nanotube field effect transistor biosensors.....	39
3.1 Introduction.....	40
3.2 suspended CNT device architecture.....	40
3.3 suspended CNT charaterization	42
3.4 Electronic measurements in a liquid environment.....	42
3.5 The charge noise model	43

TABLE OF CONTENTS (Continued)

	<u>Page</u>
3.6 Microscopic origins of noise.....	47
3.7 Conclusions.....	49
3.8 Acknowledgement	49
3.9 Supporting information.....	50
3.10 References.....	52
4. Single electron charge sensitivity of liquid-gated carbon nanotube transistors	55
4.1 Introduction.....	56
4.2 Device architecture	57
4.3 Substrate induced RTS noise in CNT FETs	58
4.4 Gate-dependence of trap occupation.....	60
4.5 Doping vs. mobility effect.....	61
4.6 Theoretical modeling of RTS amplitude.....	62
4.7 Dependence of RTS amplitude on carrier type.....	66
4.8 Conclusion	67
4.9 Methods.....	67
4.10 Acknowledgements.....	68
4.11 Supporting information.....	69
4.12 References.....	72
5. Concluding discussion	75
6. Curriculum vitae	79
7. Bibliography	81
8. Appendices.....	89
Appendix A. PMMA transfer of aligned CNTs.....	90
Appendix B. Lysozyme conjugation to a CNT.....	95
Appendix C. Thermolysin conjugation to a CNT	100
References.....	103

LIST OF FIGURES

<u>Figure</u>	<u>Page</u>
Figure 1.1. Diagram of a CNT and the protein thrombin	4
Figure 1.2. Diagram of CNT gate geometry with transistor curves.....	5
Figure 1.3. Diagram of liquid gate geometry.....	6
Figure 1.4. Current noise from a CNT	11
Figure 1.5. RC circuit diagram	11
Figure 1.6. Model diagram of a diffusive CNT	15
Figure 1.7. Band diagram of the effects of charge traps on a CNT	18
Figure 2.1. Fabrication process of a suspended CNT	28
Figure 2.2. SEM scans of platinum electrode degradation	31
Figure 2.3. SEM scan of a suspended CNT	32
Figure 2.4. Suspended CNT FET device characteristics	33
Figure 2.5. Power spectral density of suspended CNT current noise	34
Figure 2.6. Charge noise model fit to CNT current noise.....	36
Figure 3.1. Pristine suspended CNT device charaterisites.....	41
Figure 3.2. Suspended CNT FET properties in liquid	43
Figure 3.3. Environmental charge noise of CNT FETs	46
Figure 3.4. pH dependece of transitors curves.....	48
Figure 3.5. Device variability at CNT-trench interface	50
Figure 3.6. Suspended CNT device exposure to HHCC.....	50
Figure 3.7. Suspended CNT device exposure to poly-L-lysine	51
Figure 4.1. Diagram of suspended and substrate-bound CNT FETs	58
Figure 4.2. Substrate induced RTS noise.....	59
Figure 4.3. Gate-voltage dependence of RTS amplitude.....	60

LIST OF FIGURES (Continued)

<u>Figure</u>	<u>Page</u>
Figure 4.4. Change in resistance from RTS noise	65
Figure 4.5. Dependence of RTS amplitude on carrier type	66
Figure 4.6. Low and high current RTS level statistics.....	69
Figure 4.7. Simulated free carrier screening lengths	70
Figure 4.8. General resistance fluctuations for several devices.....	71
Figure A.1. PMMA transfer of aligned CNTs	90
Figure A.2. Diagram of top-gate CNT circuit.....	93
Figure B.1. Lysozyme conjugation to a CNT	95
Figure B.2. SDS-PAGE gel of T4 lysozyme s90c mutant.....	98
Figure B.3. Unfiltered T4 lysozyme coating SiO ₂ substrate.....	98
Figure C.1. AFM scan of 400 nM thermolysin incubation.....	101
Figure C.2. AFM scan of 4 μM thermolysin incubation	102

LIST OF TABLES

<u>Table</u>	<u>Page</u>
Table 3. 1. CNT noise increase after protein coating	51

Liquid-Gated Carbon Nanotube Transistor Noise Sources and Sensitivity limits

CHAPTER 1

Introduction

1.1 Nanoscale biotechnology

The synthesis, manipulation, and integration of materials at the nanometer scale have ushered in a new era of scientific inquiry, one that straddles the traditional boundaries of physics, chemistry, and the biological sciences. Control of materials at the nanometer scale has opened the doors to observe, probe, and interface with the fundamental biological building blocks of life. These technological advances are the basis for a new approach to quantitative systems biology, offering a platform to investigate the origins of emergent-level biological function that arises from the complex interactions of its constituent components.^{1,2}

The development of nanoscale field-effect transistor (nanoFET) technologies such as carbon nanotubes (CNTs), silicon nanowires, and graphene are an important part of this new paradigm. These nanoFET platforms have allowed scientists to detect previously uncharted biological interactions at the nanoscale, including probing protein-antibody interactions,³ unraveling the kinetics of individual DNA-hybridization events,⁴ resolving biochemical reactions at the single molecule level⁵ and the observation of real-time protein dynamics.⁶ These nanotechnology tools provide a platform to interrogate the fundamental biological processes at the nanoscale, and can also be scaled and multiplexed to explore the origins of emergent biological behavior.

The scope of the following discussion is to examine electrostatic interactions at the nanometer scale, developing a framework to understand sensing mechanisms and sources of noise in nanoFET biological sensors.

1.2 Bioelectronic fields

The ‘machinery’ of the biological world is governed by dynamic processes that involve both the spatial and temporal modulation of electric fields. The modulation of these fields is the result of physical charge transfer, or the movement of charged molecules. These electrostatic perturbations are the underlying mechanisms controlling critical processes ranging from the catalytic activity of proteins and enzymes⁷ to the cellular signaling of neuronal networks.²

A classic example of dynamic spatial movement at the nanoscale is illustrated in the behavior of the protein lysozyme. As a crucial biological defender, lysozyme ‘attacks’ invading foreign cell bodies by cleaving structural components of the foreign cell wall. The ‘attack’ process is the result of two distinct configurations. Each configuration creates a unique electrostatic surface. The interconversion between the two configurations enables the catalytic action of the protein. The protein structures were first discovered through protein crystallography in the 1960s,⁸ and subsequent research has focused on measuring the time dynamics of the interconversion process.⁶ Protein structure, function and biochemical interactions are responsible for the regulation and welfare of large-scale cellular systems.⁷

While the above example highlights the importance of electrostatics at the single molecule level, electrostatics also plays a critical role at the cellular level. Cells communicate with each other through electric potentials that are initiated by the physical pumping of Na^+ and K^+ ions.⁹ The coordinated effort of these pumps forms electric potential spikes known as action potentials, and generates the complex electronic signals in the brain and nervous system. Understanding the correlation between electronic signals at the single cell level to the mesoscopic network scale is a critical step towards understanding and treating degenerative diseases in the brain such as Alzhiemers.¹⁰

Deciphering the links between bioelectronic potentials at the microscopic level to emergent systems-level biological phenomena would revolutionize the field of life sciences.

1.3 Carbon nanotubes as bioelectronic probes

Single-walled carbon nanotubes have a typical diameter (d) of approximately $\sim 1\text{-}2$ nm, with an order of magnitude similar to that of the ‘building blocks of life’, DNA, RNA, and proteins. A pictorial representation of a CNT and the protein thrombin (a critical molecule in the formation of blood clotting) is shown in Figure 1.1. The size, chemical inertness, and exceptional

electronic properties of CNTs make them ideal nanometer-scale bioelectronic probes.¹¹

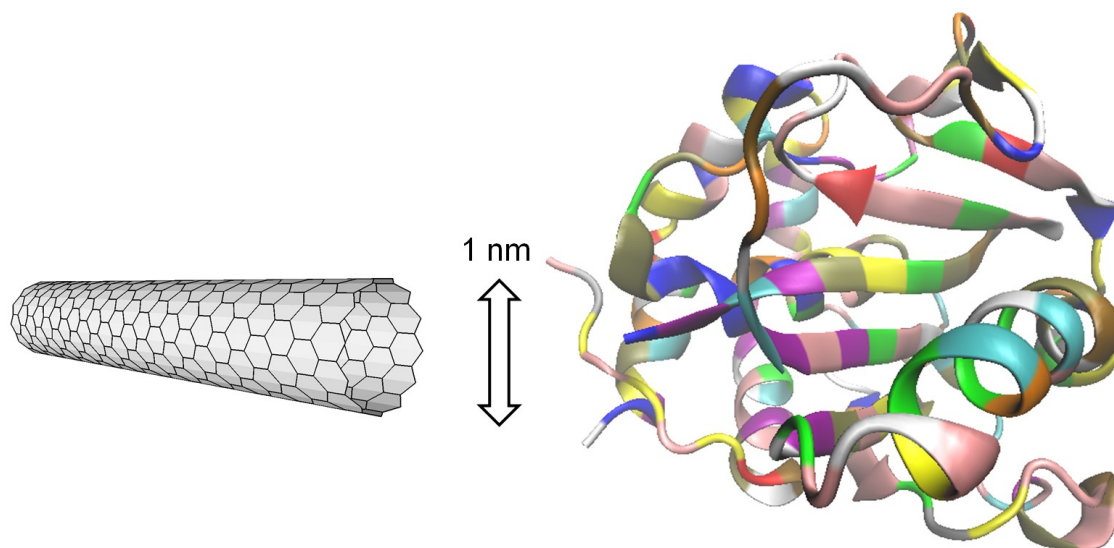


Figure 1.1. A single-walled carbon nanotube and the protein thrombin.

In addition to their small size, CNTs have exceptional electronic properties. Semiconducting CNTs can be integrated into the field-effect transistor geometry, where the number of carriers can be tuned by an external potential.¹² Figure 1.2a depicts a CNT FET device integrated in the traditional back-gate configuration. Current (I_{sd}) measured through the device while operating under constant source-drain bias is plotted as a function of gate-voltage (V_g), as shown in Figure 1.2b. This field-effect response makes the CNT an ideal candidate to probe bioelectric fields at the nanometer scale.

To study biological systems, CNT FETs must be operated and characterized in physiological environments. Figure 1.2d shows a transistor curve taken in the liquid-gate configuration using 10 mM phosphate buffer (PB). A comparison with the back-gate configuration reveals two striking differences (Figure 1.2b). The first is a dramatic reduction in hysteresis compared to the back-gate configuration, and the second is a significant increase in the gate-coupling efficiency to the CNT channel in the liquid-gate geometry. These properties, low-

hysteresis and strong gate coupling, make liquid-gated CNTs well suited to probe nanoscale bioelectronic fields (see the work of Heller et al. for an overview of CNT biosensing mechanisms¹³⁻¹⁵).

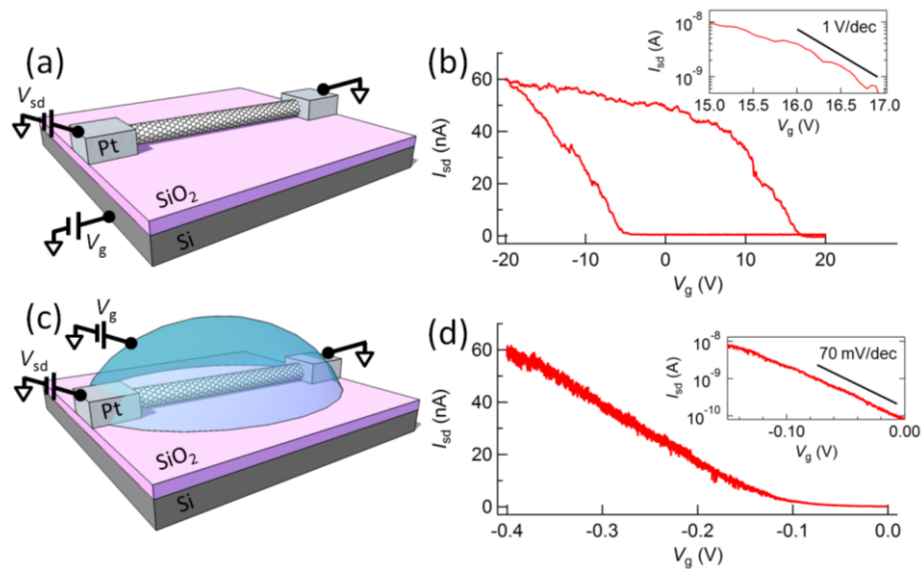


Figure 1.2. (a) Back-gate geometry of a CNT FET. (b) Current vs. back-gate voltage measured in a CNT device with a source-drain bias of 25 mV. The Si back-gate is separated by 500 nm thermal SiO₂. (c) Liquid-gate configuration of a CNT FET. (d) Current vs. liquid-gate voltage measured in 10 mM PB. The inset highlights the subthreshold slope.

1.4 Liquid-gating and the electric double layer

The strong gate coupling for liquid gated CNT FETs is the result of electrostatic interactions between ions in solution and the CNT channel. At the CNT-liquid interface, mobile ions are electrostatically drawn to charged free carriers (holes/electrons) of charge, q_i , that reside on the CNT surface, as shown in Figure 1.3a. The electric potential outside the CNT is a superposition of screened Coulomb potentials formed by the collective distribution of q_i on its surface. The potential generated by each charge is given by the Debye-Hückel equation¹⁶

$$\phi(r) \propto \sum_i \frac{q_i}{r} e^{-r/\lambda_D}, \quad (1.1)$$

where λ_D is the Debye screening length. As a consequence of Eq.1.1, the liquid potential ϕ_{liquid} (set by V_g) will transition rapidly to the potential of the CNT ϕ_{CNT} as diagrammed to the right of Figure 1.3a. The characteristic screening length is given by λ_D , found when $\phi(r)$ falls off by a factor of $1/e$, and given by

$$\lambda_D \approx \frac{0.3}{\sqrt{[C]}} nm \cdot \sqrt{M}, \quad (1.2)$$

which depends on the Molar concentration (M) of ions in solution [C], assuming monovalent ion species.¹⁶ For a 10 mM phosphate buffer solution, the bulk liquid potential (ϕ_{liquid} set by V_g) transitions to the resting CNT potential (ϕ_{CNT}) over a distance of ~ 3 nm. This is equivalent to the cylindrical gate circuit geometry, as illustrated in Figure 1.3b.

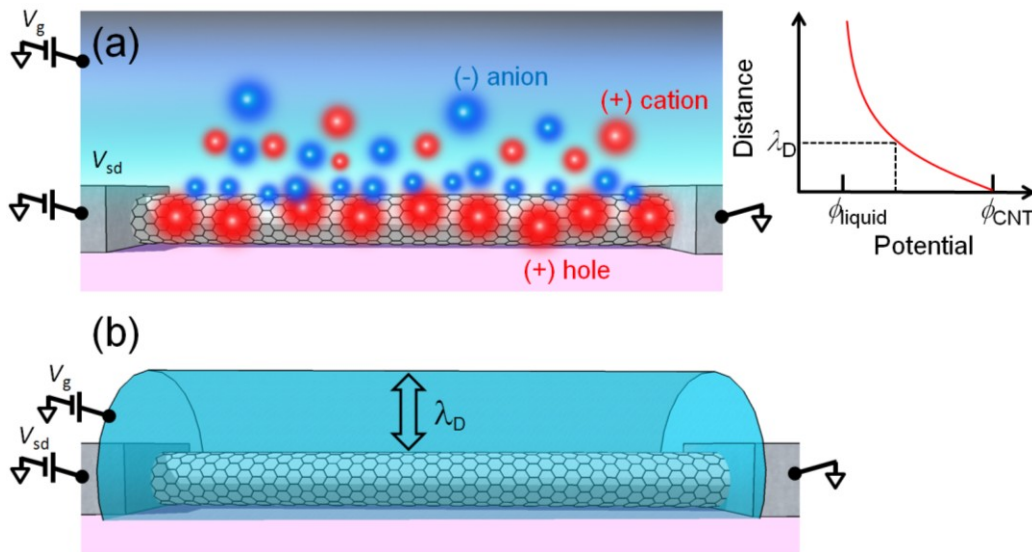


Figure 1.3. (a) Cartoon of the electric double layer formed at the CNT-liquid interface. Negatively-charged anions (blue circles) are attracted to the positive holes in the CNT (red circles in the CNT). (b) Equivalent circuit diagram of (a) with a cylindrical gate placed at a λ_D .

The physical structure of the CNT FET gate geometry plays a crucial role in the ability both to tune and hold the free carrier concentration at a fixed value.

The amount of charge (ΔQ) that can be electrostatically induced in the CNT channel follows the simple relation $\Delta Q = C_g \cdot \Delta V_g$, where C_g is the gate capacitance. The major difference between the transistor curves taken in the back-gate (Figure 1.2b) and liquid-gate (Figure 1.2d) configurations is the high gate capacitance achieved in the liquid-gated geometry.

To calculate C_g for a liquid-gated CNT, we need to consider both the geometric capacitance and the potential energy cost required for an electron to occupy a new state. The number of states (n) available per unit energy (ε) per unit length in the 1D CNT system is given by¹⁷

$$D(\varepsilon) = \Delta n / \Delta \varepsilon = \frac{4}{\pi \cdot v_F \cdot \hbar}, \quad (1.3)$$

where v_F and \hbar are the Fermi velocity of the free carrier and Plank's constant, respectively. Consequently, the potential energy cost required to add a free carrier to a CNT is quantized, and gives rise to the quantum capacitance (per unit length)

$$C_q = \frac{e^2}{\Delta \varepsilon} = \frac{4e^2}{\pi \cdot v_F \cdot \hbar} = 3.86 \times 10^{-10} F, \quad (1.4)$$

with $v_F = 8 \times 10^5$ m/s. The total gate capacitance is then a sum of the quantum and geometric capacitors in series $C_g = (1/C_q + 1/C_{geom})^{-1}$. For a back-gated CNT (Figure 1.2a), C_{geom} per unit length is given by¹⁸

$$C_{geom}^{back} = \frac{4\pi\varepsilon_r\varepsilon_0}{2\ln(2Z_{gate}/R_{CNT})} = 2.93 \times 10^{-11} F, \quad (1.5)$$

where Z_{gate} (500 nm) and R_{CNT} (1 nm) are the gate dielectric ($\varepsilon_r = 4$) thickness and CNT radius, respectively. For the liquid-gated CNT (Figure 1.2c), the geometric capacitance per unit length (assuming a cylindrical gate, as shown in Figure 1.3b) is

$$C_{geom}^{liquid} = \frac{2\pi\epsilon_r\epsilon_0}{\ln(Z_{gate}/R_{CNT})} = 2.48 \times 10^{-9} F, \quad (1.6)$$

with Z_{gate} at a radial distance, λ_D , (3 nm for 10 mM PB) from the CNT sidewall and a dielectric constant of $\epsilon = 80$ for water. In this case, the back-gate capacitance is ~ 10 times smaller than C_q , and the system is therefore governed by geometrical capacitance. In the case of the liquid-gate configuration, $C_q \approx 10 \cdot C_{geom}^{liquid}$, and the system will be governed by the quantum of capacitance.

1.5 Subthreshold swing

To experimentally measure the gate-coupling efficiency, we can examine electron transport in the subthreshold regime of a CNT FET. In this regime, thermally-activated carriers (holes/electrons) are dominant. The chemical potential of free carriers is on the order of a few $k_B T$ above the band edge (ϵ_b) and is within the band-gap. The mechanism populating free carriers into the valence band is driven by a thermally-activated process, which follows the Fermi-Dirac distribution function,¹⁷

$$f(\epsilon) = \frac{1}{e^{(\epsilon-\mu)/k_B T} + 1}, \quad (1.7)$$

where μ is the chemical potential of the system, which is set by V_g . The total number of free carriers, n_{free} , is given by

$$n_{free} = \int_{\epsilon_b}^{\infty} D(\epsilon) f(\epsilon) d\epsilon. \quad (1.8)$$

In the limit where $\mu - \epsilon_b \gg k_B T$, we can determine how varying the chemical potential from the initial state, $\mu_i = \epsilon_b + \epsilon_i$, to the final state, $\mu_f = \epsilon_b + \epsilon_f$, impacts n_{free} . The ratio of free carriers in these two states is given by

$$\frac{n_{free}^f}{n_{free}^i} = \frac{\int_{\varepsilon_b}^{\infty} D(\varepsilon) e^{-(\varepsilon - \mu_i)/k_B T} d\varepsilon}{\int_{\varepsilon_b}^{\infty} D(\varepsilon) e^{-(\varepsilon - \mu_f)/k_B T} d\varepsilon} = \frac{e^{\mu_i/k_B T} \int_{\varepsilon_b}^{\infty} D(\varepsilon) e^{-\varepsilon/k_B T} d\varepsilon}{e^{\mu_f/k_B T} \int_{\varepsilon_b}^{\infty} D(\varepsilon) e^{-\varepsilon/k_B T} d\varepsilon} = e^{\Delta\varepsilon/k_B T}, \quad (1.9)$$

where $\Delta\varepsilon = \varepsilon_i - \varepsilon_f$. The change in band energy scales linearly with ΔV_g , such that $\Delta\varepsilon = e \cdot \alpha \cdot \Delta V_g$, where $\alpha = C_g / C_q \leq 1$ is the gate-coupling efficiency and e is the charge of an electron. In the subthreshold, device conductivity scales linearly with the number free carriers,¹⁷ the ratio $n_{free}^f / n_{free}^i = I_{sd}(V_g^f) / I_{sd}(V_g^i)$, where V_g^f and V_g^i are the final and initial values of V_g . The magnitude of ΔV_g required to change I_{sd} by one decade (factor of ten) is called the subthreshold swing, and is given by

$$Swing = \frac{\ln(10)k_B T}{\alpha \cdot e}, \quad (1.10)$$

which yields a room-temperature limit of $Swing \approx 60$ mV/decade, when $\alpha = 1$. As shown in the inset of Figure 1.2d, a liquid-gated CNT FET can approach the room temperature limit, with $Swing \approx 70$ mV/decade. The liquid-gate configuration is limited by the quantum capacitance, a result that was first demonstrated by Rosenblatt et al.¹⁹

Subthreshold swing is a direct measure of the geometric capacitance of a FET, since $\alpha = C_g / C_q$. We can use $Swing$ as a metric to quantify the gate-coupling enhancement of the liquid-gate to the back-gate configurations (see Figure 1.2) by taking the ratio $Swing_{back} / Swing_{liquid} \approx C_q / C_g^{back} \approx 10$. The liquid-gate geometry offers a 10-fold increase in gate coupling efficiency over the traditional back-gate geometry. In Chapter 3 we show that pristine suspended CNTs form an ideal cylindrical gate in liquid environments that approach the room temperature limit of $\alpha = 1$.²⁰

1.6 Sensitivity and noise

The trend to shrink transistor technologies to the nanometer scale presents an inescapable problem, where the magnitude of electronic noise scales inversely to the size of the system.²¹ As a device approaches nanoscale dimensions, surface interactions and disorder at this scale can dominate the noise of these systems.²²⁻²⁴ To better understand the performance and limitations of CNTs, we must identify the dominant sources of electronic noise.

Figure 1.4a shows the constant-bias current passing through a CNT FET operating in a physiological environment. The power spectrum of current fluctuations (S_I) is shown in Figure 1.4b as a solid red line. The frequency spectrum of current noise is a crucial consideration in determining the viability of a device as an electronic sensor. In the case of monitoring biological activity, many biological processes involve millivolt scale fluctuations that occur over millisecond time scales. Some examples include the activity of proteins and enzymes undergoing changes in conformational states,⁶ and the firing of action potentials in neurons, nerve, and muscle cells.² Therefore understanding both the magnitude and spectral dependence of electronic noise in CNT FETs is a critical parameter in the design of bioelectronic sensors. In Chapters 2 and 3 we discuss the design principles and measurement techniques required to investigate noise in CNT FET biosensors.²⁵

Noise in electrical circuit elements is typically classified as Johnson noise, shot noise, or $1/f$ noise. These types of noise are briefly reviewed in the following sections.

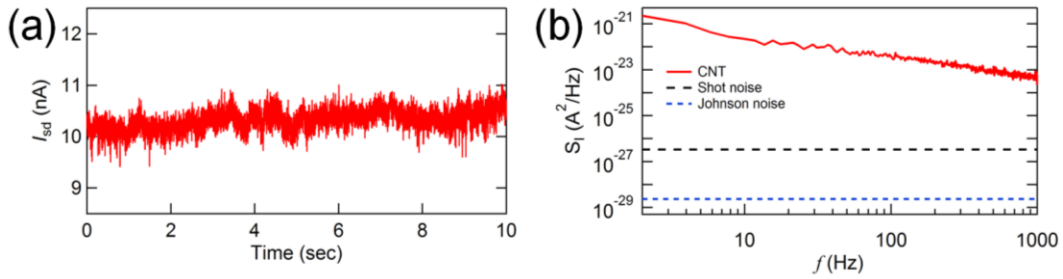


Figure 1.4. (a) Current measured as a function of time for a CNT operating under constant bias, $V_{sd} = 25$ mV. (b) Power spectral density of the current noise taken from (a), shown as a red solid line. The dotted black and blue lines are the respective shot and Johnson noise magnitudes for current and resistances values equivalent to (a).

1.7 Johnson noise

We first consider the effects of temperature-induced electronic noise called ‘Johnson noise’. A circuit element with resistance R at finite temperature T will exhibit spontaneous voltage fluctuations V_s . We can derive the essential physical principles of this thermally-induced noise by analyzing a model RC circuit. First, we consider a series circuit with a voltage source, V_s , capacitor, C , and resistor, R , as illustrated in Figure 1.5.

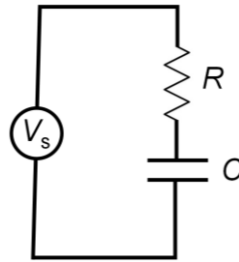


Figure 1.5. Diagram of an RC -circuit with source V_s corresponding to thermally induced voltage fluctuations.

Our goal is to calculate the magnitude and spectrum of V_s . At a finite temperature, the time-averaged potential energy stored in C will be equivalent to the time-averaged kinetic energy of thermally-driven carries in R , and given by the equipartition theorem,

$$\frac{1}{2} k_B T = \frac{1}{2} C \cdot \overline{V_C^2}, \quad (1.11)$$

assuming one normal mode of electric oscillation in the circuit, where $\overline{V_C}^2$ is the mean square voltage across C .²⁶ Using the voltage divider equation, we can determine the frequency (f) dependent square of the voltage signal across C

$$V_C^2 = \frac{V_s^2}{(2\pi \cdot f \cdot R \cdot C)^2 + 1}. \quad (1.12)$$

The mean square voltage is simply the integral of Eq. 1.12 over all f ,

$$\overline{V_C}^2 = \int_0^{\infty} V_C^2 df = \frac{S_V}{4R \cdot C}, \quad (1.13)$$

where $S_V = V_s^2$ is the power spectral density of thermally-induced voltage fluctuations. Combining Eq.1.13 with Eq. 1.11, we arrive at the expression for the thermally-induced voltage noise of a resistor power spectrum

$$S_V^{John} = 4k_B T \cdot R, \quad (1.14)$$

and the equivalent current noise power spectrum is given by the Thevenin equivalent

$$S_I^{John} = \frac{4k_B T}{R}. \quad (1.15)$$

For circuit elements with a resistance R that is frequency independent, Johnson noise has a uniform spectral distribution over all frequencies. The CNT shown in Figure 1.4b has $R = 2.4 \text{ M}\Omega$, therefore $S_I^{John} = 6.6 \times 10^{-27} \text{ A}^2/\text{Hz}$, which is lower than experimental measurements. Johnson noise corresponding to the resistance of the CNT channel is not a significant noise source in the frequency range of interest.

1.8 Shot noise

Electrical currents are not composed of a continuous and even distribution of charge, but rather come in quantized units. This form of noise is termed ‘shot

noise'. The magnitude of noise generated by the flux of electrons through a circuit element follows the principles of Poisson statistics. For example, if N electrons (on average) pass through a circuit over a given time interval, ΔT , then the standard deviation in the number of electrons per unit time is

$$\sigma_N = \sqrt{N} = \sqrt{\frac{I_0 \cdot \Delta T}{e}}, \quad (1.16)$$

where I_0 and e are the baseline current levels and charge of the electron. The variation in current per unit time is given by

$$\Delta I_{RMS} = \frac{e}{\Delta T} \sigma_N = \sqrt{I_0 \cdot q \cdot 2 \cdot \Delta f}. \quad (1.17)$$

The measurement window is limited by the Nyquist frequency, $\Delta f = 1/(2 \cdot \Delta T)$, since both the minima and maxima of a periodic signal are required to gain knowledge of f . The power spectrum of current fluctuations for shot noise measured over a given bandwidth is

$$S_I^{shot} = \frac{(\Delta I_{RMS})^2}{\Delta f} = 2 \cdot q \cdot I_0. \quad (1.18)$$

Shot noise also has flat spectral distribution that only depends on the magnitude of the current. The CNT shown in Figure 1.4b has $I_0 \sim 10$ nA, therefore $S_I^{shot} = 3.2 \times 10^{-27}$ which is significantly lower than experimental measurements. The source-drain current used to operate CNT FETs is typically large enough so that shot noise is not a significant noise source.

1.9 1/f noise

Current noise in CNT FETs has a power spectrum that scales as $1/f$, as shown in Figure 1.4b. The amplitude of this noise is several orders of magnitude larger than both the Johnson and shot noise calculated above. This $1/f$ spectrum is a ubiquitous property of semiconducting devices and is attributed to the

superposition of thermally activated trapping and de-trapping of charged defects at the semiconductor-gate dielectric interface.²³ This process creates fluctuations in conductance with the following power spectrum,²¹

$$S_I = \frac{A \cdot I^2}{f}, \quad (1.19)$$

where A is a parameter set by the material. Empirical observations have shown that for a broad class of semiconducting materials $A \propto 1/n_{free}$, a result known as the Hooge model.²¹

Low dimensional systems with large scattering lengths such as CNTs are dominated by ballistic transport.¹² Theoretical predictions by Tersoff²² have shown that in the ballistic CNT system

$$A = \frac{(\delta V)^2}{I_{sd}^2} \left(\frac{dI_{sd}}{dV_g} \right)^2, \quad (1.20)$$

where δV is equivalent to a fluctuating gate-voltage. Combining Eq.1.19 and Eq.1.20 yield the simple relationship

$$S_I = S_V \cdot \left(\frac{dI_{sd}}{dV_g} \right)^2, \quad (1.21)$$

where $S_V \propto 1/f$ and is the power spectrum of voltage fluctuations. Equation 1.21 is easily interpreted. The current noise is caused by a time varying fluctuation in the effective gate voltage, $\delta V(t)$, and produces time-dependent current noise $\delta I(t)$ that scales directly with transconductance

$$\delta I(t) = \delta V(t) \cdot \frac{dI_{sd}}{dV_g}. \quad (1.22)$$

This model is coined the ‘charge-noise’ model, and has been experimentally confirmed to be the dominant noise source in CNT²⁷ and graphene transistors in liquid environments.²⁸

Attempts to control $1/f$ noise in CNT FETs have been previously performed by removing substrate and conventional lithography-based residues.^{24,29} The interpretation of these results relies on the Hooge model, which fails to accurately capture the gate-voltage dependent behavior of CNT noise, and therefore remains ambiguous. In Chapter 3, we systematically control the environment surrounding a CNT and utilize the ‘charge-noise’ model to quantify the contributions of substrate, polymer, and biomolecular interactions to the electronic noise floor of a CNT FET.²⁰

1.10 Length dependence of charge noise

We next consider how the magnitude of ‘charge-noise’ changes with channel length (L_{CNT}). To construct a model for diffusive transport, we first decompose the CNT channel into a series sum of short segments of length L as shown in Figure 1.5, where L is somewhat longer than the phonon scattering length (see Purewal et al. for a discussion on phonon scattering in CNTs.³⁰)

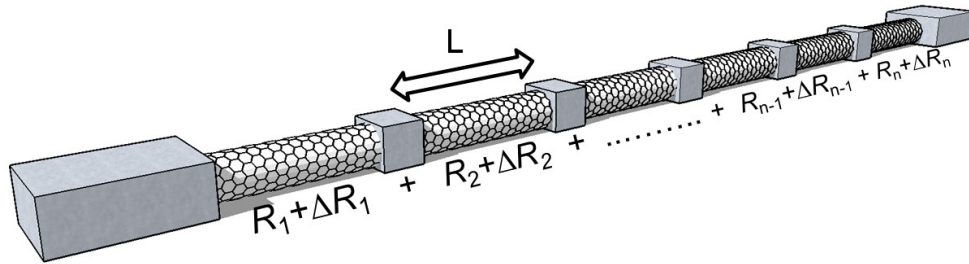


Figure 1.6. Equivalent circuit diagram of a CNT composed of the series sum of diffusive segments with length L .

The net resistance of the CNT is a summation of individual segments, and is given by

$$R = \sum_{i=1}^n R_i + \sum_{i=1}^n \Delta R_i = R_{DC} + \Delta R, \quad (1.23)$$

where R_i is the DC resistance of segment length L , and ΔR_i the resistance fluctuation due to ‘charge- noise’. The total resistance sums to a DC component (R_{DC}) that includes the effects of finite contact resistance and fluctuating component ΔR . The channel conductance ($G=1/R$) can be written in the following form

$$G = \frac{1}{R_{DC} \left(1 + \frac{\Delta R}{R_{DC}} \right)}. \quad (1.24)$$

Under the condition that $\Delta R / R_{DC} \ll 1$, we arrive at the following expression

$$G \approx \frac{1}{R_{DC}} - \frac{\Delta R}{R_{DC}^2}. \quad (1.25)$$

The first term of Eq.1.25 is the mean DC conductance, while the second term is the fluctuating ‘charge-noise’ component of the channel conductance, δG . If the resistance fluctuations are uncorrelated and the electrostatic fluctuations for each segment of the channel are uniform, $\Delta R = \Delta R_i / \sqrt{n}$. The fluctuation in channel conductance is given by the following expression,

$$\delta G = \frac{1}{R_{DC}^2} \frac{\Delta R_i}{\sqrt{n}} = \frac{1}{R_{DC}^2} \frac{\Delta R_i}{\sqrt{L_{CNT}/L}}. \quad (1.26)$$

In light of the ‘charge noise’ model, the voltage noise ‘felt’ by a CNT channel in the diffusive limit is given by

$$\delta V = \frac{\delta G}{(dG/dV_g)} = \frac{1}{\sqrt{L_{CNT}}} \frac{\zeta}{(dI_{sd}/dV_g)}, \quad (1.27)$$

with $\zeta = V_{sd} \cdot \Delta R_i / (R_{DC}^2 \sqrt{L})$. The voltage-noise scales inversely with the square root of channel length. This result can be utilized to optimize both the geometry and performance of CNT transistors.²⁷

1.11 Random telegraph signals

Stochastic fluctuations of charge traps in the vicinity of a semiconducting channel give rise to $1/f$ noise, as previously discussed. The potential energy landscape of a semiconducting channel is distorted as a result of these fluctuating charge traps, see Figure 1.6a. These fluctuations modulate the free carrier density in the CNT, but do not cause significant scattering.

If a charge trap is close to the channel, it can cause scattering as well as modulate the free carrier density.^{23,31-33} Figure 1.6b illustrates the electrostatic potential energy along a CNT as the result of a charge trap in close proximity to the sidewall of a CNT. These fields are screened over the nanometer scale, leading to an electrostatic barrier that is only a few nanometers wide.³⁰ Free carriers encountering this electrostatic perturbation have a finite probability of scattering.¹⁷

The time-dependent occupation of the charge trap is a thermally activated process,³¹ and produces time-dependent fluctuation in carrier mobility, which is observed as random telegraph signals (RTS) in current noise as shown in the lower portion of Figure 1.6b. The amplitude of RTS current noise is intimately linked to the Fermi energy of free carriers, and depends strongly on both the polarity of the trap state and carrier type.³³

Recent work performed by Sorgenfrei et al,⁴ Choi et al,^{6,34} and Simms et al.³⁵ has demonstrated that a single, biologically active molecule in close proximity to a CNT FET will produce RTS current fluctuations. The physical mechanism generating biologically-induced RTS fluctuations in CNTs lacks a general consensus, and experimental results have been interpreted as both doping³⁴ and mobility effects.⁴ In Chapter 4, we investigate the amplitude of RTS current fluctuations in CNT FETs. Our results demonstrate that these signals depend on V_g in a manner that is consistent with the mobility fluctuations previously proposed by Wang et al.³³

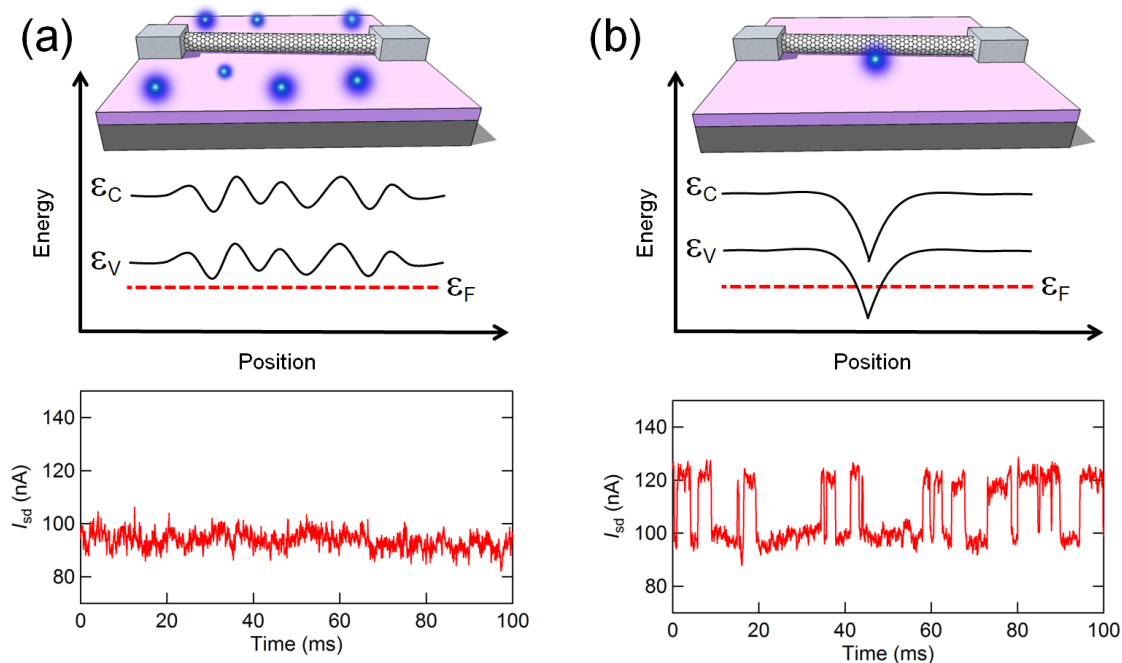


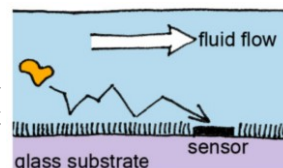
Figure 1.7. (a) Band diagram of several charge trap fluctuations in the vicinity of a CNT channel. The fluctuations in current shown below arise from fluctuations in the free carrier density, which follows the ‘charge noise’ model. (b) Band diagram of a single charge trap in close proximity to a CNT channel. Current noise dominated by a single trap is shown below, which is the result of mobility fluctuations as described by the Landauer scattering formalism.

1.12 Graduate work not included in this thesis

I have been involved in several projects that lie outside the scope of this dissertation. Below are brief summaries of the peer-reviewed work to which I have contributed as a co-author, along with descriptions of my involvement in each project. The work is divided into two subsets: (1) Biosensing and (2) Optoelectronics.

Biosensing

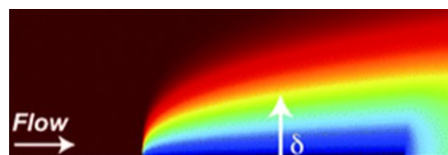
- 1) M. R. Leyden, C. Schuman, **T. Sharf**, J. W. Kevek, V. T. Remcho, and E.D. Minot, 'Fabrication and Characterization of Carbon Nanotube Field-Effect Transistor Biosensors', *Proc. of SPIE*, 7779 (2010)



Developing ‘label-free’ electronic biosensing technologies offer a platform for cheap and affordable point of care medical diagnostics. Here, the

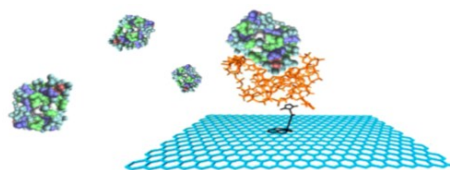
fabrication, preparation and development of sensing protocols are described for CNT biosensors. My contribution to this work was the development of a microfluidic interface used to control and deliver biomolecules in solution to a CNT circuit.

- 2) M. R. Leyden, R. J. Messinger, C. Schuman, **T. Sharf**, V. T. Remcho, T. M. Squires, and E. D. Minot, 'Increasing the Detection Speed of an All-Electronic Real-Time Biosensor', *Lab on a Chip*, 12 (2012)



In this work we studied biosensor response time, which is strongly dependent on the binding rate of biomolecules to the surface of a sensor. We utilize protein repellent coatings to limit the non-specific binding of proteins to undesired region of the sensors surface. We observe over a 2.5-fold increase in the protein flux to the active sensing area when the upstream binding sites are blocked. Our results demonstrate a new methodology for characterizing nanoelectronic biosensor performance, and demonstrate a mass transport optimization strategy that is applicable to a wide range of microfluidic based biosensors. I developed the microfluidic delivery system for these experiments, which allowed for the precise control of fluid flow rates over the sensors surface.

- 3) G. Saltzgaber, P. Wojcik, **T. Sharf**, M. R. Leyden, J. L. Wardini, C.A. Heist A.A. Adenuga, V. T. Remcho, and E.D. Minot, 'Scalable Graphene Field-Effect Sensors for Specific Protein Detection', *Nanotechnology*, 24 (2013)

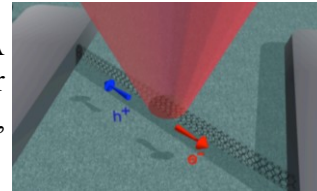


We demonstrate that micron-scale graphene field-effect transistor biosensors can be fabricated in a scalable fashion from large-area chemical vapor deposition derived graphene. We electrically detect the real-time binding and unbinding of a protein biomarker, thrombin, to and from aptamer-coated graphene surfaces. Our sensors have low background noise and high transconductance, comparable to exfoliated graphene devices. The devices are

reusable and have a shelf-life greater than one week. I designed and fabricated a pneumatic fluid delivery system that eliminated parasitic electronic noise associated with commercial electronic syringe pumps.

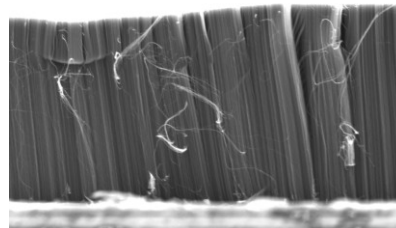
Optoelectronics

- 4) T. Deborde, J.W. Kevek, **T. Sharf** and E.D. Minot, 'A Spectrally-Tunable Photocurrent Microscope for Characterizing Nanoelectronic Devices', *Nanotechnology (IEEE-NANO)*, 11 (2011)



Scanning photocurrent microscopy is a unique tool that facilitates both device characterization and the study of fundamental properties of optoelectronic nanomaterials. We have built a scanning photocurrent microscope that incorporates a super continuum laser as the light source. The microscope illuminates nanoelectronic devices with a micron scale light spot and a photon energy that is tunable from 0.67 eV to 2.7 eV. We describe the design of our microscope and present measurements of carbon nanotube transistor devices. These measurements highlight the features of our microscope, particularly the advantages of combining spatial and spectral resolution when characterizing nanoelectronic devices. I contributed to the device design and fabrication of suspended CNT devices for this project.

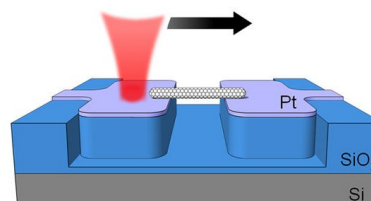
- 5) M. J. Paul, N. A. Kuhta, J. L. Tomaino, A. D. Jameson, L. P. Maizy, **T. Sharf**, N. L. Rupesinghe, K. B. K. Teo, S. Inampudi, V. A. Podolskiy, E. D. Minot, and Y. S. Lee, 'Terahertz Transmission Ellipsometry of Vertically Aligned Multi-Walled Carbon Nanotubes', *Applied Physics Letters*, 101 (2012)



We demonstrate time-resolved terahertz transmission ellipsometry of vertically aligned multi-walled carbon nanotubes. The angle-resolved transmission measurements reveal anisotropic characteristics of the terahertz electro-dynamics in multi-walled carbon nanotubes. The anisotropy is, however, unexpectedly weak: the ratio of the tube-axis conductivity to the

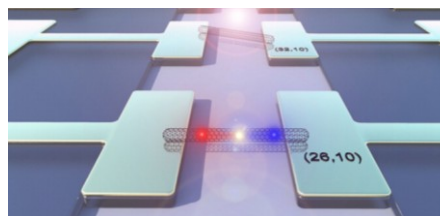
transverse conductivity, $\sigma_z/\sigma_{xy} \cong 2.3$, is nearly constant over the broad spectral range of 0.4–1.6 THz. The relatively weak anisotropy and the strong transverse electrical conduction indicate that THz fields readily induce electron transport between adjacent shells within multi-walled carbon nanotubes. I performed measurements using scanning electron microscope to determine the length of the vertically aligned CNT films. These measurements were a critical parameter in determining the transmission of the terahertz radiation as a function of sample thickness.

- 6) T.DeBorde, L. Aspitarte, **T.Sharf**, J.W. Kevek, and E.D. Minot 'Photothermoelectric effect in suspended semiconducting carbon nanotubes', *ACS Nano*, 8 (2014)



We have performed scanning photocurrent microscopy measurements of field-effect transistors (FETs) made from individual ultraclean suspended carbon nanotubes (CNTs). We investigate the spatial-dependence, polarization-dependence, and gate-dependence of photocurrent and photovoltage in this system. While previous studies of surface-bound CNT FET devices have identified the photovoltaic effect as the primary mechanism of photocurrent generation, our measurements show that photothermoelectric phenomena play a critical role in the optoelectronic properties of suspended CNT FETs. We have quantified the photothermoelectric mechanisms and identified regimes where they overwhelm the photovoltaic mechanism. I contributed to the device design and fabrication of suspended CNT devices for this project.

- 7) T.DeBorde, L. Aspitarte, **T.Sharf**, J.W. Kevek, and E.D. Minot 'Determining the chiral index of semiconducting carbon nanotubes using photoconductivity resonances', *Journal of Physical Chemistry C*, (2014)



We utilize photoconductivity spectroscopy to identify the unique chiral structure of individual carbon nanotubes (CNTs). Peaks in photoconductivity are measured throughout the visible and near-IR wavelength ranges. Photoconductivity peaks associated with individual CNTs are referenced against existing Rayleigh scattering measurements to uniquely identify chiral indices. We find close agreement between our assigned exciton resonances and the previously published exciton resonances. The typical net energy mismatch is ≤ 20 meV. By enabling chiral identification of CNTs after the completion of device fabrication, the technique offers a facile method for investigating relationships between CNT structure and electronic/optoelectronic properties. I contributed to the device design and fabrication of suspended CNT devices for this project.

1.13 References

- 1 Alivisatos, A. P. *et al.* The Brain Activity Map Project and the Challenge of Functional Connectomics. *Neuron* **74**, 970-974, doi:DOI 10.1016/j.neuron.2012.06.006 (2012).
- 2 Alivisatos, A. P. *et al.* Nanotools for Neuroscience and Brain Activity Mapping. *Acs Nano* **7**, 1850-1866, doi:Doi 10.1021/Nn4012847 (2013).
- 3 Cui, Y., Wei, Q. Q., Park, H. K. & Lieber, C. M. Nanowire nanosensors for highly sensitive and selective detection of biological and chemical species. *Science* **293**, 1289-1292 (2001).
- 4 Sorgenfrei, S. *et al.* Label-free single-molecule detection of DNA-hybridization kinetics with a carbon nanotube field-effect transistor. *Nat Nanotechnol* **6**, 125-131, doi:DOI 10.1038/nnano.2010.275 (2011).
- 5 Goldsmith, B. R., Coroneus, J. G., Kane, A. A., Weiss, G. A. & Collins, P. G. Monitoring single-molecule reactivity on a carbon nanotube. *Nano Lett* **8**, 189-194, doi:Doi 10.1021/N10724079 (2008).
- 6 Choi, Y. K. *et al.* Single-Molecule Lysozyme Dynamics Monitored by an Electronic Circuit. *Science* **335**, 319-324, doi:DOI 10.1126/science.1214824 (2012).
- 7 Petsko, G. A. & Ringe, D. *Protein Structure and Function*. (New Science Press, 2004).

- 8 Matthews, B. W. Determination of Position of Anomalously Scattering Heavy Atom Groups in Protein Crystals. *Acta Crystallogr* **20**, 230-&, doi:Doi 10.1107/S0365110x6600046x (1966).
- 9 Huang, S. C. J. *et al.* Carbon Nanotube Transistor Controlled by a Biological Ion Pump Gate. *Nano Lett* **10**, 1812-1816, doi:Doi 10.1021/NI100499x (2010).
- 10 Kosik, K. S. Study neuron networks to tackle Alzheimer's. *Nature* **503**, 31-32 (2013).
- 11 Allen, B. L., Kichambare, P. D. & Star, A. Carbon nanotube field-effect-transistor-based biosensors. *Adv Mater* **19**, 1439-1451, doi:DOI 10.1002/adma.200602043 (2007).
- 12 Javey, A. & Kong, J. *Carbon nanotube electronics*. (Springer, 2009).
- 13 Heller, I. *et al.* Identifying the mechanism of biosensing with carbon nanotube transistors. *Nano Lett* **8**, 591-595, doi:Doi 10.1021/NI072996i (2008).
- 14 Heller, I. *et al.* Influence of Electrolyte Composition on Liquid-Gated Carbon Nanotube and Graphene Transistors. *J Am Chem Soc* **132**, 17149-17156, doi:Doi 10.1021/Ja104850n (2010).
- 15 Heller, I., Mannik, J., Lemay, S. G. & Dekker, C. Optimizing the Signal-to-Noise Ratio for Biosensing with Carbon Nanotube Transistors. *Nano Lett* **9**, 377-382, doi:Doi 10.1021/NI8031636 (2009).
- 16 Larrimore, L. *Chemical and biological sensing with carbon nanotubes in solution* PhD thesis, Cornell, (2008).
- 17 Kittel, C. *Introduction to solid state physics*. (John Wiley & Sons, Inc., 2005).
- 18 Sazonova, V. *et al.* A tunable carbon nanotube electromechanical oscillator. *Nature* **431**, 284-287, doi:Doi 10.1038/Nature02905 (2004).
- 19 Rosenblatt, S. *et al.* High performance electrolyte gated carbon nanotube transistors. *Nano Lett* **2**, 869-872, doi:Doi 10.1021/NI025639a (2002).
- 20 Sharf, T., Kevek, J. W., DeBorde, T., Wardini, J. L. & Minot, E. D. Origins of Charge Noise in Carbon Nanotube Field-Effect Transistor Biosensors. *Nano Lett* **12**, 6380-6384, doi:Doi 10.1021/NI303651t (2012).

- 21 Hooge, F. N. 1/F Noise Sources. *Ieee T Electron Dev* **41**, 1926-1935 (1994).
- 22 Tersoff, J. Low-frequency noise in nanoscale ballistic transistors. *Nano Lett* **7**, 194-198, doi:Doi 10.1021/NI062141q (2007).
- 23 Clement, N., Nishiguchi, K., Fujiwara, A. & Vuillaume, D. One-by-one trap activation in silicon nanowire transistors. *Nat Commun* **1**, doi:Doi 10.1038/Ncomms1092 (2010).
- 24 Lin, Y. M., Tsang, J. C., Freitag, M. & Avouris, P. Impact of oxide substrate on electrical and optical properties of carbon nanotube devices. *Nanotechnology* **18**, doi:Doi 10.1088/0957-4484/18/29/295202 (2007).
- 25 Sharf, T., Kevek, J. W. & Minot, E. D. Fabrication of low-noise carbon nanotube field-effect transistor biosensors. *Nanotechnology (IEEE-NANO), 2011 11th IEEE Conference on* **11**, 122-125, doi:10.1109/NANO.2011.6144640 (2011).
- 26 Nyquist, H. Thermal agitation of electric charge in conductors. *Physical Review* **32**, 110 (1928).
- 27 Mannik, J., Heller, I., Janssens, A. M., Lemay, S. G. & Dekker, C. Charge noise in liquid-gated single-wall carbon nanotube transistors. *Nano Lett* **8**, 685-688, doi:Doi 10.1021/NI073271h (2008).
- 28 Heller, I. *et al.* Charge Noise in Graphene Transistors. *Nano Lett* **10**, 1563-1567, doi:Doi 10.1021/NI903665g (2010).
- 29 Sangwan, V. K., Ballarotto, V. W., Fuhrer, M. S. & Williams, E. D. Facile fabrication of suspended as-grown carbon nanotube devices. *Appl Phys Lett* **93**, doi:Doi 10.1063/1.2987457 (2008).
- 30 Purewal, M. S. *et al.* Scaling of resistance and electron mean free path of single-walled carbon nanotubes. *Phys Rev Lett* **98**, doi:Doi 10.1103/Physrevlett.98.186808 (2007).
- 31 Ralls, K. S. *et al.* Discrete Resistance Switching in Submicrometer Silicon Inversion-Layers - Individual Interface Traps and Low-Frequency (1-F Questionable) Noise. *Phys Rev Lett* **52**, 228-231, doi:DOI 10.1103/PhysRevLett.52.228 (1984).
- 32 Peng, H. B., Hughes, M. E. & Golovchenko, J. A. Room-temperature single charge sensitivity in carbon nanotube field-effect transistors. *Appl Phys Lett* **89**, doi:Doi 10.1063/1.2399942 (2006).

- 33 Wang, N. P., Heinze, S. & Tersoff, J. Random-telegraph-signal noise and device variability in ballistic nanotube transistors. *Nano Lett* **7**, 910-913, doi:Doi 10.1021/NI062742h (2007).
- 34 Choi, Y. *et al.* Dissecting Single-Molecule Signal Transduction in Carbon Nanotube Circuits with Protein Engineering. *Nano Lett* **13**, 625-631, doi:Doi 10.1021/NI304209p (2013).
- 35 Sims, P. C. *et al.* Electronic Measurements of Single-Molecule Catalysis by cAMP-Dependent Protein Kinase A. *J Am Chem Soc* **135**, 7861-7868, doi:Doi 10.1021/Ja311604j (2013).

CHAPTER 2

Fabrication of Low-Noise Carbon Nanotube Field-Effect Transistor Biosensors

Tal Sharf, Joshua W. Kevek, and Ethan D. Minot

Nanotechnology (IEEE-NANO), 2011 11th IEEE Conference on **2011**, 11, 122-
125

The fabrication of suspended carbon nanotube field effect transistors (CNT FETs) designed for biological sensing applications is discussed. We compare the electrical properties of our suspended CNT FET design to standard surface based CNT FETs. In particular, we show a reduction in environmental noise, suggesting that the new sensor design is a promising candidate for low-noise sensing applications.

2.1 Introduction

The two-terminal resistance of a semiconducting carbon nanotube (CNT) device is sensitive to the binding of biomolecules onto the CNT surface. Several groups have demonstrated this effect using CNTs lying on substrates¹, however, there are compelling reasons to perform biosensor experiments using suspended CNT devices. Suspended CNTs are a significant distance away from charge traps in the dielectric substrate. These charge traps introduce environmental noise and limit the sensitivity of CNT-based electronic sensors²⁻⁴. Suspended CNT devices also allow measurements of the interactions between biomolecules and CNTs without interference from the substrate.

Here we describe the development of suspended carbon nanotube field effect transistors (CNT FETs) that are specifically designed for biological sensing applications. Our fabrication process produces suspended CNTs with clean surfaces and minimal environmental noise. The electrode layout is compatible with a microfluidic system for delivering biological molecules to the sensor.

2.2 Biosensor Fabrication

Our suspended CNT FET biosensors satisfy the following design constraints:

- (i) Transistor channels consist of a single semiconducting CNT that does not touch the underlying dielectric substrate.
- (ii) The CNT surface is free of contaminants such as photoresist residue.
- (iii) The electrode geometry is compatible with fluid delivery.
- (iv) The fabrication process is time/cost effective.

The key fabrication steps are based on previous work by Kong *et al.*⁵ and Cao *et al.*⁶ These steps are illustrated in Figure 1. An important modification to previous recipes is the introduction of a reactive ion etch (Fig. 1c) which streamlines the process.

Our starting substrate is a 6 inch $\text{Si}_3\text{N}_4/\text{SiO}_2/\text{Si}$ wafer. The top layer consists of CVD grown Si_3N_4 (100 nm thickness) on top of thermally grown SiO_2 (1 μm thickness). For future devices we plan to omit the Si_3N_4 layer because it is not necessary.

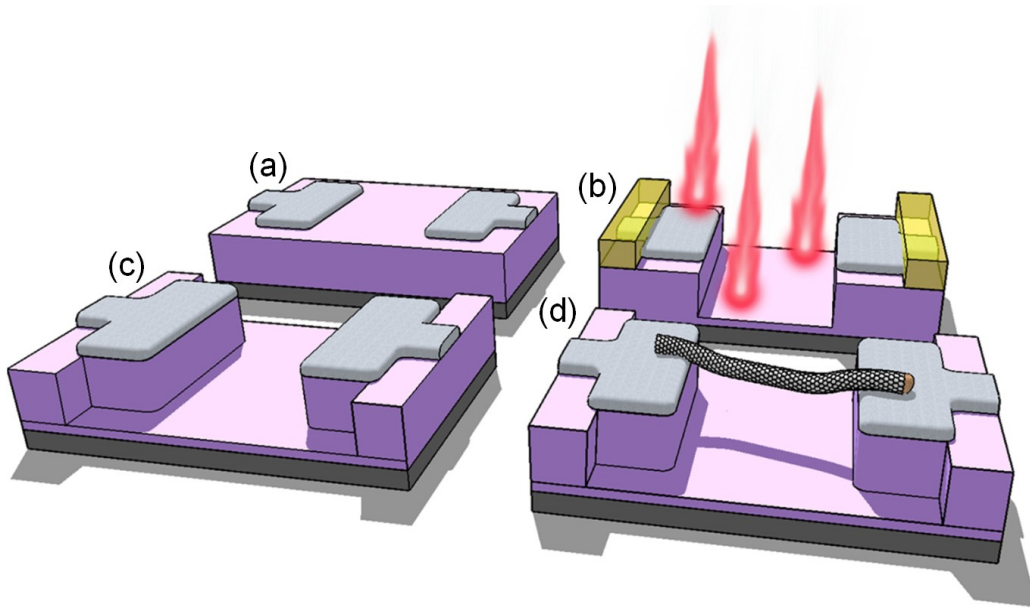


Figure 2.1. Fabrication process to produce ultra-clean suspended CNTs. (a) Metal electrodes were formed by depositing a 1nm Ti sticking layer followed by 100nm Pt, forming a 1 μm electrode gap. (b-c) A 20 μm wide photoresist window was patterned to serve as a mask for a 1 μm deep reactive ion etch. (d) Alumina supported catalyst was patterned on the Pt followed by a CVD fast heat growth, producing an ultra-clean suspended CNT device.

Platinum electrodes are patterned using standard photolithography and metal deposition techniques (Shipley 1813, image reversal, electron beam evaporation of a Ti sticking layer of 1 nm thickness, and a Pt layer of 100 nm thickness). The gap between the electrodes is 1 μm . It has been previously established that suspended CNTs can withstand the forces associated with liquid wetting if the suspended length is 3 μm or less.⁷ The Pt electrodes extend a distance of approximately 1 cm away from the gap. The long electrode length makes it possible to clamp microfluidic channels onto the device while still performing electrical characterization.

A second patterning step is used to etch the SiO₂ substrate. A 20 μm window is created in a photoresist layer (Shipley 1813) and reactive ion etching (RIE) is used to remove the 100 nm Si₃N₄ layer and 900 nm of SiO₂ (Fig. 2b-c). The dielectric is masked by both the photoresist and the Pt electrodes, creating an etch pattern that is self-aligned to the electrodes. The RIE is an anisotropic process that produces a trench with vertical side walls.

A third patterning step is used to place CNT catalyst on the Pt electrodes (Fig 1d). Windows with dimension 4 μm x 14 μm are patterned in the photoresist layer. The windows are positioned on the Pt electrode and are set back 2 μm from the edge. After patterning the photoresist, the wafer is diced into 30 individual pieces and stored until the final processing step.

The final processing step is CNT growth. Directly before CNT growth, a catalyst is deposited on the chip (3.3 mM Iron(iii) nitrate nonahydrate, 1 mM Molybdenum(vi) dioxide bis(acetyl-acetonate), 9.8 mM Alumina prepared in DI H₂O solution). The liquid suspension catalyst is drop cast onto the surface, allowed to sit for 5 minutes and followed promptly by a N₂ blow dry. The chip was then rinsed with a DI H₂O squirt and followed by PR removal by a sequential rinse with acetone, IPA, DI H₂O and followed by an N₂ blow dry.

Fast-heat chemical vapor deposition (CVD) growth was utilized to produce pristine CNTs on top of the Pt electrodes⁵. The fast-heat method minimizes the time that Pt electrodes are exposed to high temperature conditions. Figure 2 shows scanning electron micrographs of the Pt surface after being exposed to different high temperature conditions either with or without the fast-heat method. Figure 2a shows a severely damaged Pt surface after a standard CVD growth. Temperature was ramped to $T_{\text{growth}} = 850 \text{ C}^\circ$ in H₂ (0.45 SLM), followed by a 5 minute growth (0.45 SLM H₂ and 1.8 SLM CH₄), and cooling in Ar (1 SLM); during all steps the chip remained in the active heat zone of the furnace. Clearly, this standard CVD growth method does not preserve the

integrity of the Pt electrodes. Moreover, the alumina supported catalyst becomes encapsulated in Pt and no CNT growth is observed.

The fast heat method reduces the time that the chip is exposed to the hot zone of the growth furnace. A quartz shuttle inside the one inch growth tube is used to rapidly load the substrate in and out of the hot zone. A steel washer on the cool end of the shuttle allows the operator to move the shuttle by sliding a small permanent magnet along the outside of the quartz tube. With the chip outside the hot zone, the furnace is ramped up to T_{growth} , then the chip is slid inside the hot zone for 5 minutes. Figure 2b shows the Pt surface after a fast heat growth at $T_{\text{growth}} = 850^{\circ}\text{C}$. There is a clear improvement compared to standard growth, however, to fully preserve the integrity of the Pt we found that fast heating at $T_{\text{growth}} = 820^{\circ}\text{C}$ is preferable (Fig. 2c). This growth temperature is still high enough to produce a good yield of CNT devices.⁷

For higher density growth of CNTs, it is possible to deposit more catalyst on the Pt electrode. To increase the amount of catalyst, we drop cast the liquid suspension catalyst on the chip and then evaporate all water by placing the chip on a 90°C hotplate. The resulting “mountain” of catalyst is seen in Fig. 2d. We also find that substituting CH_4 -based growth with an alcohol vapor growth increases growth density. The growth conditions in Fig. 2d are $T_{\text{growth}} = 820^{\circ}\text{C}$, 0.45 SLM H_2 , 0.3 SLM Ar bubbled in ice cold ethanol and 0.15 SLM Ar bubbled in ice cold methanol. Several CNTs are visible in the top of Fig. 2d.

When using optimized CNT growth parameters we obtain 1 or 2 devices per chip that show electrical characteristics that are consistent with an individual semiconducting CNT bridging the gap between electrodes.

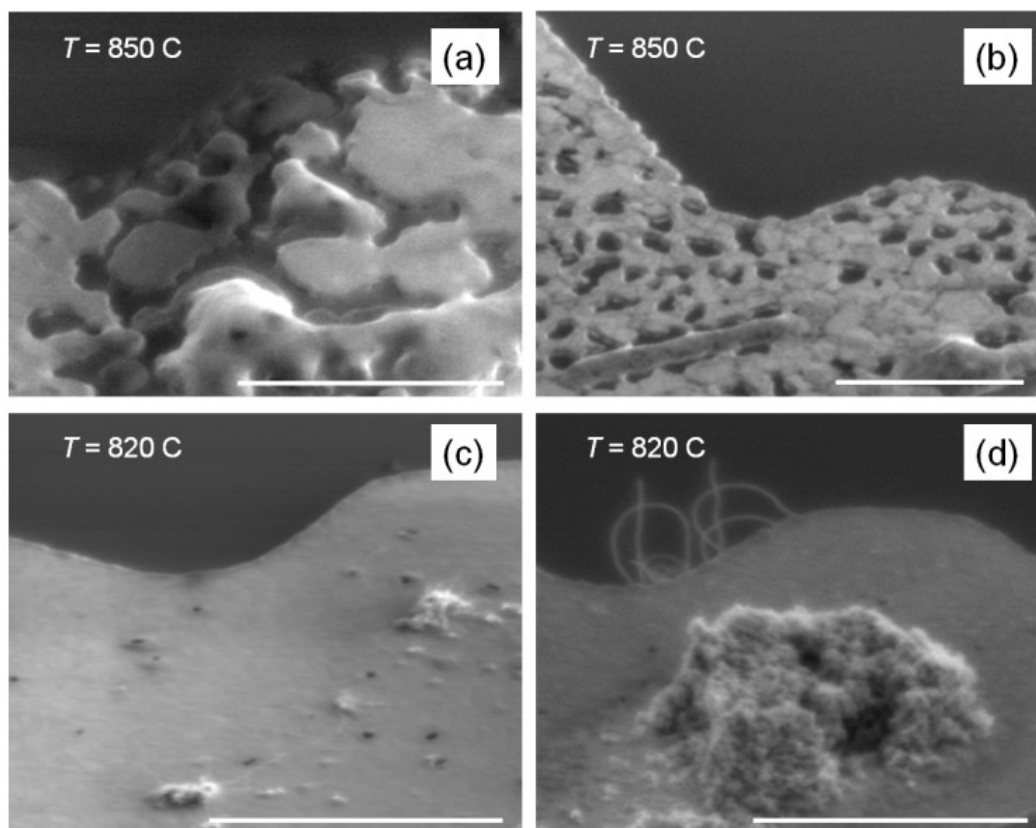


Fig. 2.2. SEM scans (5 μm scale bars) showing the Pt electrodes after various CVD growth time and durations. (a) Ramp up and cool in the active heat zone of furnace at 850C, CH_4 growth. (b) Fast heat CH_4 growth at 850C for 5 minutes (c) Fast heat growth CH_4 820C for 5 minutes (d) Fast heat alcohol growth with increased catalyst density, 820C for 5 minutes.

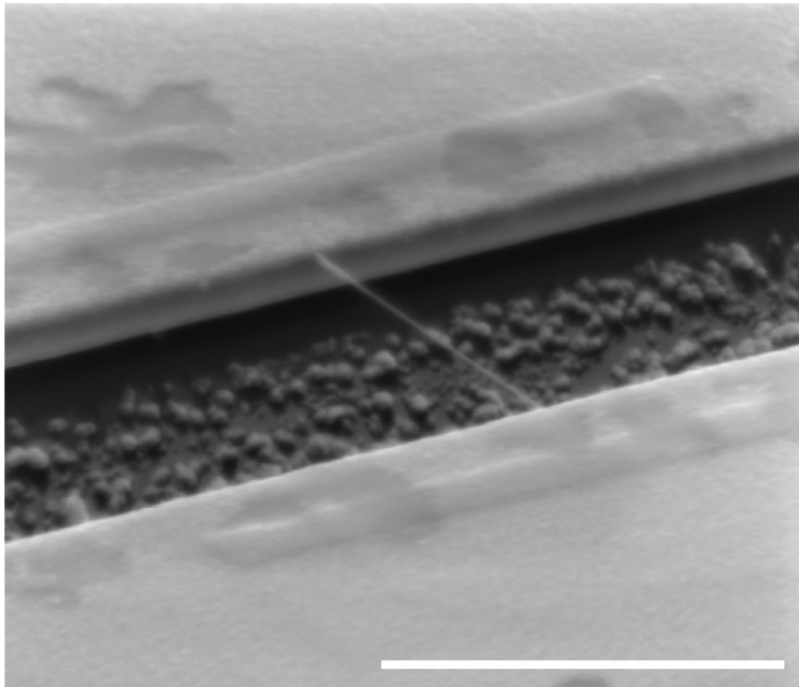


Figure 2.3. SEM image (3 μm scale bar) of a single CNT bridging a gap between two gold electrodes. The CNT was placed over the trench by means of a PMMA assisted transfer, using a technique described by Jiao *et al.*⁸ Due to time constraints the authors were unable to attain an SEM scan of the current devices under investigation.

2.3 Electronic Properties of a Suspended CNT

Suspending a CNT above a dielectric surface (rather than touching the dielectric surface) can dramatically reduce the environmental noise associated with charge fluctuations at dielectric surfaces^{2,9,10}. An SEM image of a suspended CNT device is shown in Fig. 3 illustrating the structure of our suspended CNT sensors. The CNT is well above the underlying oxide as it hangs between the two metal electrodes.

Figure 5a shows transistor characteristics of a suspended semiconducting CNT device that was produced following the fabrication process described in Section II. The characteristics were obtained in ambient conditions (room temperature, exposed to air) with a source-drain bias $V_{\text{sd}} = 25$ mV. For comparison, Fig. 4b shows a typical transistor characteristic of a non-suspended

CNT device. As observed by previous authors, the suspended CNT device has substantially less hysteresis^{2,9,10}.

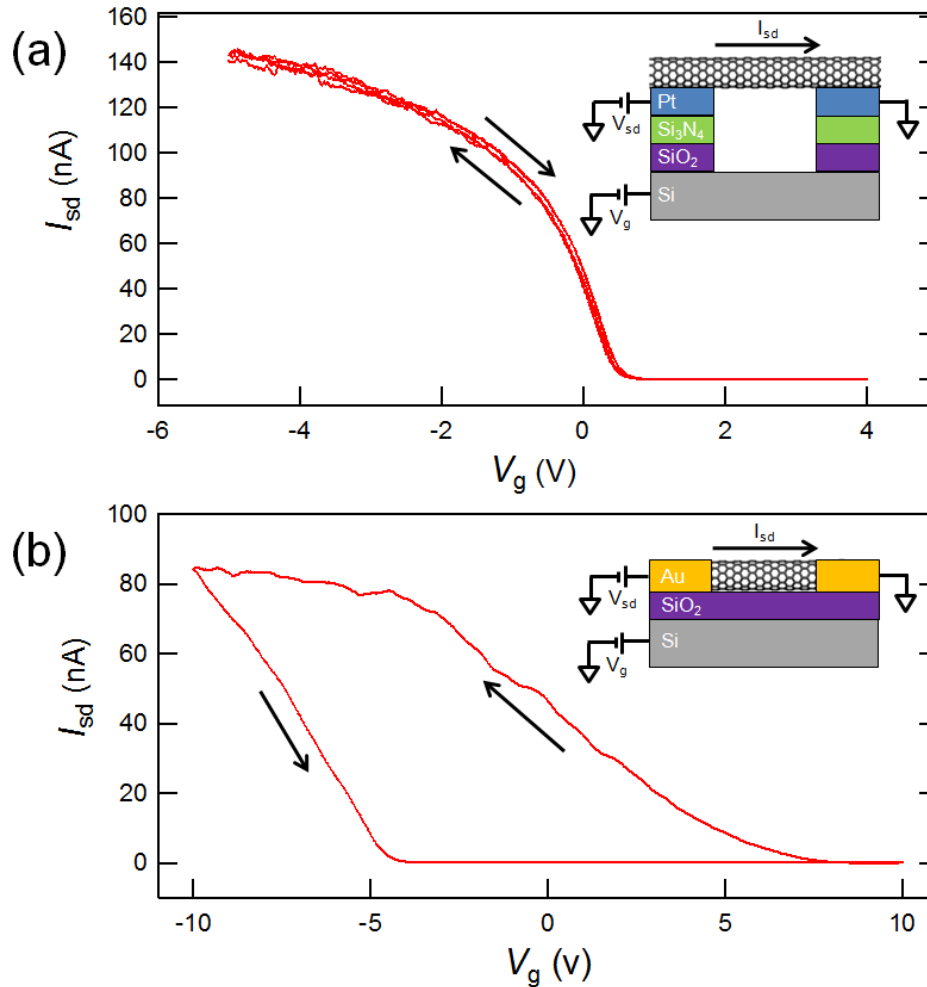


Figure 2.4. Source-Drain current as a function of gate voltage (sweep rate $dV_g/dt = 1$ V/sec). (a) Suspended CNT grown on Pt shows very little hysteresis. (b) Surface based CNT exhibits a comparatively larger hysteresis offset.

To quantify the capacitive coupling between the global backgate and the suspended CNT, C_g/C_{total} , we have measured $I(V_g)$ in the subthreshold regime where current drops exponentially over several decades (Fig. 5a)¹¹. The subthreshold slope is 300 mV/dec, differing by a factor 5 from the room temperature limit of 60 mV/dec. The subthreshold slope suggests a capacitive coupling $C_g/C_{total} = 0.2$.

The goal of our work is to produce sensitive transistor devices with very low levels of background noise. To investigate noise levels in a suspended CNT FET we have measured current fluctuations over a range of different gate voltages. Figure 5b shows the power spectral density of current fluctuations, $S_I(f)$, at five different values of V_g . Similar power spectral densities ($S_I \sim 1/f$) have been previously reported for CNT devices¹².

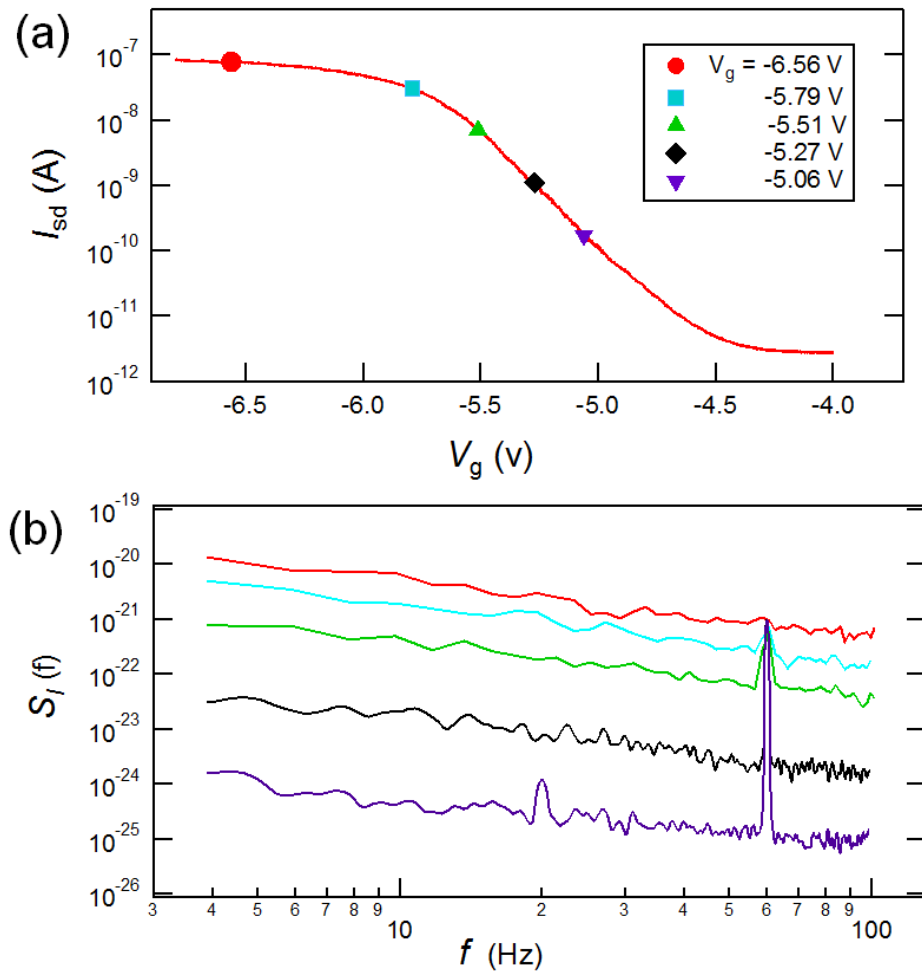


Figure 2.5. (a) Semi-log plot of source-drain current as a function of gate voltage (gate sweep 10mV/sec). (b) Visualization of the Power Spectral Density for 5 different gating values, clearly showing $1/f$ dependence.

We analyze the current fluctuations using the charge noise model that was first introduced by Tersoff¹³ and later experimentally verified by Mannik et al.¹²

The charge noise model assumes that fluctuations in current are caused by fluctuations in the electrostatic environment such that

$$S_I(f) = S_{input}(f) \left(\frac{dI}{dV_g} \right)^2, \quad (2.1)$$

where $S_{input}(f)$ has units of V^2/Hz . Equation (1) is equivalent to the statement that $\delta I = (dI/dV_g)\delta V_g$ where δI is a fluctuation in current caused by a fluctuation in effective gate voltage δV_g .

We fit Eq. 2.1 to our measured data using one free parameter. Figure 6 shows measured values of S_I at $f = 10$ Hz compared to the line $S_{input}(10 \text{ Hz}) \cdot (dI/dV_g)^2$. The best fit value of $S_{input}(10 \text{ Hz})$ is $0.005 \text{ mV}^2/Hz$. This is equivalent to an rms environmental noise of 0.75 mV when measured over a bandwidth of $0.1 - 100 \text{ Hz}$.

Previous experimental measurements of charge noise by Mannik et al. yielded $S_{input} = 0.05 \text{ mV}^2/Hz$ at 10 Hz for surface-bound CNT devices with a channel length of $1 \mu\text{m}$. This previous report of S_{input} is 10 times larger than our current measurement.

The measurements of Mannik et al. were performed in electrolyte solution, therefore, it is possible that the electrolyte solution dominates environmental noise rather than charge noise in the dielectric substrate. To test this possibility, we are currently measuring our suspended CNT devices in electrolyte solutions.

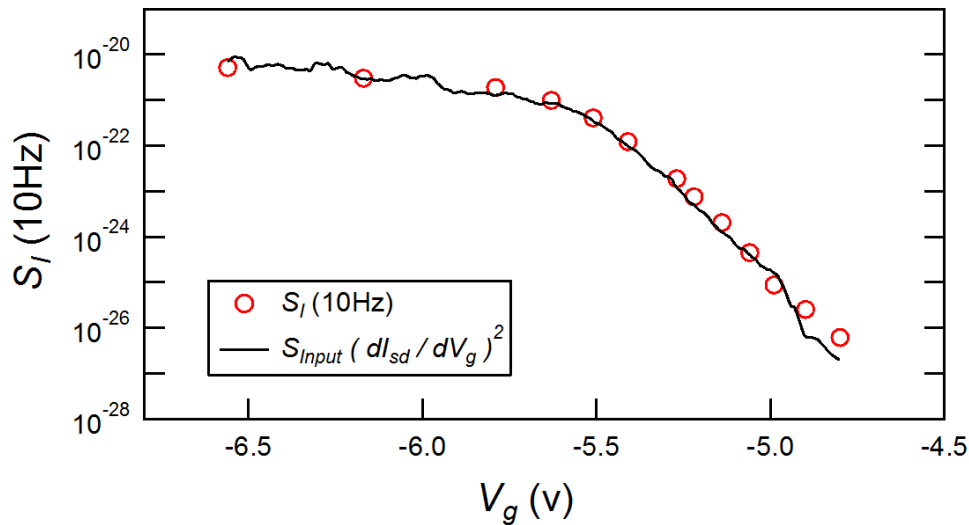


Figure 2.6. Measured power spectral density S_I (10Hz) shown as red dots. The black line is the square of the numerical derivative of the source-drain current with respect to V_g multiplied by the fitting parameter $S_{input}(10\text{ Hz})$.

2.4 Summary and Conclusion

We have fabricated suspended carbon nanotube field effect transistors that have electrode geometries suitable for integration in biological environments. We observe evidence that electrostatic fluctuations in the environment of the suspended CNT are minimized. We determine an rms electrostatic noise (stochastic modulation of the effective gate voltage) of 0.75 mV when measured over a bandwidth of 0.1 – 100 Hz. This environmental noise is significantly less than the electrostatic signals that are expected from charged proteins¹⁴. Therefore, suspended CNTs are a promising platform for high sensitivity biosensing applications.

2.5 Acknowledgment

This work is supported by the Oregon Nanoscience and Microtechnologies Institute (ONAMI). Sample fabrication was performed at the Cornell node of the National Nanofabrication Infrastructure Network, which is supported by the National Science Foundation (Grant ECS-0335765).

2.6 References

- 1 Allen, B. L., Kichambare, P. D. & Star, A. Carbon nanotube field-effect-transistor-based biosensors. *Adv Mater* **19**, 1439-1451, doi:DOI 10.1002/adma.200602043 (2007).
- 2 Lin, Y. M., Tsang, J. C., Freitag, M. & Avouris, P. Impact of oxide substrate on electrical and optical properties of carbon nanotube devices. *Nanotechnology* **18**, - (2007).
- 3 Lee, J. S. *et al.* Origin of gate hysteresis in carbon nanotube field-effect transistors. *J Phys Chem C* **111**, 12504-12507, doi:Doi 10.1021/Jp074692q (2007).
- 4 Kim, W. *et al.* Hysteresis caused by water molecules in carbon nanotube field-effect transistors. *Nano Lett* **3**, 193-198, doi:Doi 10.1021/Nl0259232 (2003).
- 5 Kong, J., LeRoy, B. J., Lemay, S. G. & Dekker, C. Integration of a gate electrode into carbon nanotube devices for scanning tunneling microscopy. *Appl Phys Lett* **86**, - (2005).
- 6 Cao, J., Wang, Q. & Dai, H. Electron transport in very clean, as-grown suspended carbon nanotubes. *Nat Mater* **4**, 745-749, doi:Doi 10.1038/Nmat1478 (2005).
- 7 Xu, Y. Q., Barnard, A. & McEuen, P. L. Bending and Twisting of Suspended Single-Walled Carbon Nanotubes in Solution. *Nano Lett* **9**, 1609-1614, doi:Doi 10.1021/Nl803861c (2009).
- 8 Jiao, L. Y. *et al.* Creation of nanostructures with poly(methyl methacrylate)-mediated nanotransfer printing. *J Am Chem Soc* **130**, 12612-+ (2008).
- 9 Muoth, M. *et al.* Hysteresis-free operation of suspended carbon nanotube transistors. *Nat Nanotechnol* **5**, 589-592, doi:Doi 10.1038/Nnano.2010.129 (2010).
- 10 Sangwan, V. K., Ballarotto, V. W., Fuhrer, M. S. & Williams, E. D. Facile fabrication of suspended as-grown carbon nanotube devices. *Appl Phys Lett* **93**, - (2008).
- 11 (The gate voltage range in Fig. 5a differs from Fig. 4a even though the same device is being measured. For the measurement in Fig. 5a, the device was held at -6.7 V for several minutes which lead to an exaggerated hysteretic effect.).

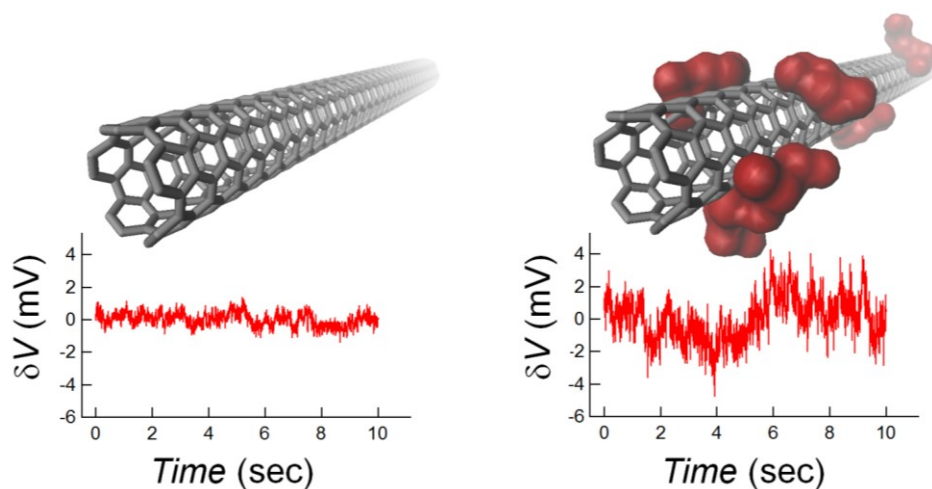
- 12 Mannik, J., Heller, I., Janssens, A. M., Lemay, S. G. & Dekker, C. Charge noise in liquid-gated single-wall carbon nanotube transistors. *Nano Lett* **8**, 685-688, doi:Doi 10.1021/NI073271h (2008).
- 13 Tersoff, J. Low-frequency noise in nanoscale ballistic transistors. *Nano Lett* **7**, 194-198, doi:Doi 10.1021/NI062141q (2007).
- 14 Prisbrey, L., Schneider, G. & Minot, E. Modeling the Electrostatic Signature of Single Enzyme Activity. *J Phys Chem B* **114**, 3330-3333 (2010).

CHAPTER 3

Origins of Charge noise in Carbon Nanotube Field-Effect Transistor Biosensors

Tal Sharf, Joshua W. Kevek, Tristan DeBorde, Jenna L. Wardini and Ethan D. Minot

Nano Letters **2012**, 12, (12), 6380-6384



Determining the major noise sources in nanoscale field-effect transistor (nanoFET) biosensors is critical for improving bio-electronic interfaces. We use the carbon nanotube (CNT) FET biosensor platform to examine the noise generated by substrate interactions and surface adsorbates, both of which are present in current nanoFET biosensors. The charge noise model is used as a quantitative framework to show that insulating substrates and surface adsorbates are both significant contributors to the noise floor of CNT FET biosensors. Removing substrate interactions and surface adsorbates reduces the power spectral density of background voltage fluctuations by 19-fold.

3.1 Introduction

Low-dimensional nanoscale field-effect transistors (nanoFETs) based on carbon nanotubes (CNTs), silicon nanowires (SiNWs) and graphene have demonstrated exceptional potential as biological sensors. NanoFETs have enabled electronic detection of single molecule dynamics,¹⁻³ highly localized measurements of intracellular electrophysiology⁴⁻⁷, and all-electronic label-free detection of disease-related biomarkers.⁸ In all these biosensing examples, the nanoFET devices are used to detect millivolt-scale changes in electrostatic potential. Such measurements are ultimately limited by a background of millivolt-scale fluctuations. Uncovering the major sources of this background noise is a crucial step in pushing the detection limits of nanoelectronic devices.

In this work we investigate the origins of electronic noise in CNT FETs operating in liquid. We build upon the theoretical work of Tersoff⁹ and experimental work of Mannik et al.¹⁰ which established a clear framework, the charge noise model, for quantifying the electrostatic background fluctuations felt by nanoFETs. By systematically controlling the environment in contact with the CNT, we quantify the noise contributions from substrate interactions and surface adsorbates. Neither factor has been previously investigated in the framework of the charge noise model.

Our experiments are performed with ultra-clean suspended CNT devices. Similar devices have been used by other researchers to demonstrate fundamental phenomena such as the Mott-Insulator transition in one-dimension,¹¹ electron-phonon coupling,¹² Klein tunneling¹³ and one-dimensional phase transitions.¹⁴ Our results show that these devices can also be used in biological sensing experiments where they offer significantly improved signal-to-noise ratios.

3.2 Suspended CNT device architecture

Figure 3.1a shows a scanning electron micrograph (SEM) of a typical device consisting of a single suspended CNT bridging a trench between two metal electrodes. Suspended CNTs were grown at the final stage of fabrication using “fast-heat” chemical vapor deposition (CVD).¹⁵ Because the CNT is grown last,

the CNT surface is free from any fabrication residues such as photoresist (PR) residue. This is a significant advantage over fabrication methods in which HF etching is used to remove SiO_2 from underneath a surface-bound CNT.¹⁶ Device fabrication is described in detail elsewhere.¹⁷ Briefly, metal electrodes (1 nm Ti, 100 nm Pt) were patterned on Si/ SiO_2 substrates, or Si/ SiO_2 / Si_3N_4 substrates. The chip was then exposed to a reactive ion etch (RIE) to create a 1 μm deep trench between the electrodes (Fig. 1b). The electrodes serve as the RIE mask. The electrodes were then capped by e-gun deposited SiO_2 . An 80 nm layer of SiO_2 reliably blocked the electrochemical currents that can occur during liquid gating. Exposed metal was left only at the probing pads and the tips of the source and drain electrodes. Alumina supported Fe catalyst was then patterned on the tips of the source and drain electrodes, followed by fast-heat CVD to produce a pristine suspended CNT device. For control experiments on surface-bound CNTs, the RIE step was foregone.

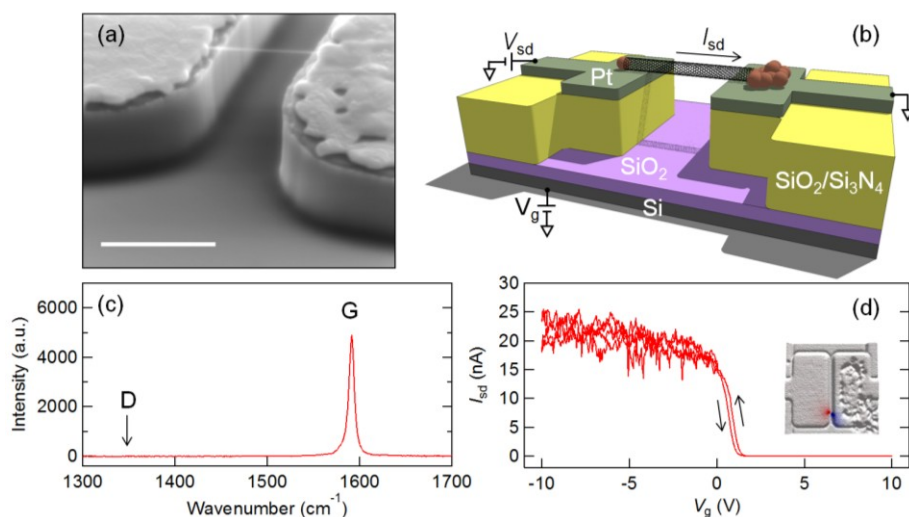


Figure 3.1. (a) SEM image of a suspended CNT bridging the gap between two Pt electrodes, the scale bar is 1 μm . (b) Diagram of suspended CNT device with channel length of 1 μm and trench depth of 1 μm . (c) Raman spectra from a suspended CNT grown by fast heat CVD. (d) Transistor curve of a suspended device operating in air under ambient conditions with no hysteresis, source-drain bias $V_{sd} = 25$ mV. The inset of (d) is photocurrent response used to identify single CNT devices. The colored dots are the photocurrent response superposed on top of the reflectance image.

3.3 Suspended CNT characterization

Raman spectroscopy was used to quantify disorder in the suspended CNT lattice. Figure 3.1c shows the Raman spectra from a suspended CNT. We observe no defect peak at 1350 cm^{-1} , which indicates that the CNT is free of lattice defects and impurities.¹⁸ Transistor curves measured in ambient conditions show little to no hysteresis. Figure 3.1d shows a typical transistor curve of a suspended, adsorbant-free and defect-free semiconducting CNT.¹⁹⁻²¹ The yield for such devices is 2 – 4 devices per chip (each chip has 24 electrode gaps).

To pre-screen devices prior to experiments in liquid, scanning photocurrent microscopy was used as a non-invasive method to identify devices with single CNTs.²² The inset of Figure 3.1d shows a typical photo-generated current at the metal-CNT interfaces of a device containing a single electrically-connected CNT.

3.4 Electronic measurements in a liquid environment

For measurements in liquid, devices were interfaced with a PDMS liquid reservoir containing solution of 5 mM phosphate buffer (PB), unless mentioned otherwise. Some measurements were repeated in a home-built flow cell and equivalent results were obtained. The solution potential was set by a liquid-gate voltage (V_{lg}) applied to an Ag/AgCl reference electrode,²³ as shown in the inset of Figure 3.2a. Faradaic currents between V_{lg} and the CNT-electrode interface were kept to a small fraction of the source-drain current. The power spectral density fluctuations in the Faradaic current were of order $10^{-27}\text{ A}^2/\text{Hz}$, which is a negligible contribution compared to the CNT intrinsic noise levels.

Figure 3.2a shows the measured current I_{sd} as a function of liquid gate potential V_{lg} for a suspended CNT ($L = 1\text{ }\mu\text{m}$) operating in 5 mM PB with an applied source-drain bias V_{sd} of 25 mV. The device exhibits near-ideal gating efficiency with a 66 mV/dec subthreshold slope, just shy of the 60 mV/decade room temperature limit.²⁴ We measured current fluctuations ($I_{sd}(t)$ at constant V_{lg}) at a number of points along the transistor curve (marked as dots on Fig. 2a). The

power spectral density of these current fluctuations (S_I) is plotted in Figure 3.2b. As previously reported, S_I follows a $1/f$ dependence.²⁵⁻²⁷

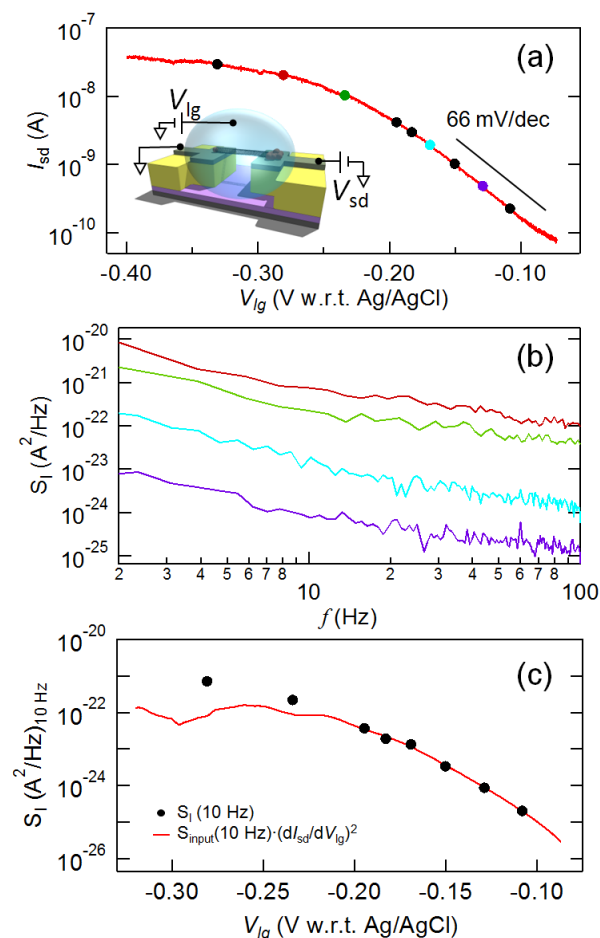


Figure 3.2. (a) Transistor curve for a liquid gated suspended CNT FET operating in 5 mM PB, the circles show where the noise measurements were conducted. (b) Power spectral density of current fluctuations measured at the colored circles from (a). (c) Circles are the Power spectral density of current fluctuation at 10 Hz plotted as a function of liquid gate voltage. The solid line is a fit to the charge noise model.

3.5 The charge noise model

The noise data shown in Figure 3.2 is consistent with the charge noise model developed by Tersoff.⁹ The charge noise model predicts that environmental charge fluctuations are the dominant source of electronic noise in CNT FETs when operating in the subthreshold regime. The environmental charge

fluctuations are equivalent to a fluctuating liquid-gate voltage δV . The resulting fluctuations in the current $\delta I_{sd}(t)$ are given by

$$\delta I_{sd}(t) = \frac{dI_{sd}}{dV_{lg}} \delta V(t), \quad (3.1)$$

and the power spectral density of $\delta I_{sd}(t)$ is $S_I(f) = S_{input}(f) \cdot (dI_{sd}/dV_{lg})^2$, where $S_{input}(f)$ is the power spectral density of $\delta V(t)$. Experimentally measured values of S_I (10 Hz) are shown in Figure 3.2c (circles) with a fit to the charge noise model (solid line). The quantity dI_{sd}/dV_{lg} was attained by numerical differentiation of the transistor curve shown in Figure 3.2a. A single parameter $S_{input}(10 \text{ Hz})$, was used to fit the noise in the subthreshold regime.

The charge noise model accurately describes current fluctuations for all 16 suspended CNT FETs we have measured in the subthreshold regime. This agrees with the previous work of Mannik et al. who verified the charge noise model for surface-bound CNTs.¹⁰ Compared to the work of Mannik et al., the noise magnitude is much less for our ultra-clean suspended CNTs. The fluctuations shown in Fig. 2 are consistent with $S_{input}(1 \text{ Hz}) = 0.028 \pm 0.003 \text{ mV}^2/\text{Hz}$. (Note that $S_{input}(1 \text{ Hz}) \approx 10S_{input}(10 \text{ Hz})$). Our result is 19 times smaller than previous measurements of $S_{input}(1 \text{ Hz})$ from surface-bound CNTs with a similar channel length of $1 \mu\text{m}$.¹⁰

To translate $S_{input}(f)$ into a meaningful detection limit one must integrate $S_{input}(f)$ over the measurement bandwidth to find the rms gate-voltage noise that is picked up by the CNT sensor. For the device shown in Figure 3.2, integrating over a bandwidth of 0.1 – 100 Hz and taking the square root yields $\delta V_{rms} = 0.44 \pm 0.14 \text{ mV}$. Previous measurements of surface-bound CNT FET biosensors yielded $\delta V_{rms} = 1.9 \text{ mV}$ for this same bandwidth.¹⁰ The signal-to-noise ratio for a nanoFET biosensor is typically determined by the ratio of the signal voltage (the change in electrostatic potential induced by a coating of biological molecules) to δV_{rms} . Comparing our ultraclean CNT device to standard surface-based CNT FET biosensors we find a 4.4-fold improvement in signal-to-noise ratio.

We observe device-to-device variability in δV_{rms} . The lowest value we have observed is $\delta V_{\text{rms}} = 0.44$ mV, while other devices show $\delta V_{\text{rms}} = 0.5 - 1.2$ mV. A likely source of variability is the Pt electrode geometry. The Pt electrodes are sharply defined before the CNT growth process, however, the high temperature CVD process softens the metal and rearranges the structure. Scanning electron microscopy imaging reveals that the Pt often creeps back from the edge of the trench and leaves exposed insulator (see supporting information Figure 3.6). Contact between the CNT and the exposed insulator could significantly affect charge noise.

Regardless of device-to-device variability, our suspended CNT devices are significantly quieter than standard CNT FET biosensors. Therefore, the suspended CNT biosensor platform allows us to search for the noise sources in traditional CNT FET biosensors. In particular, we have investigated electrostatic noise associated with substrate interactions and surface adsorbates, both of which are present in standard CNT FET biosensors.

In the experiments described below we determine δV_{rms} directly from transconductance measurements and $\delta I_{\text{sd}}(t)$. Using Eq. 1, $\delta V(t)$ is calculated from $\delta I_{\text{sd}}(t)$ and $dI_{\text{sd}}/dV_{\text{lg}}$. Given $\delta V(t)$, it is straightforward to find δV_{rms} . As a consistency check, δV_{rms} is measured at several values of $dI_{\text{sd}}/dV_{\text{lg}}$. As predicted by the charge noise model, we find that our measured values of δV_{rms} are invariant (within experimental uncertainty) across the subthreshold regime.

We first discuss measurements of δV_{rms} before and after exposing ultra-clean suspended CNTs to adsorbate molecules. A pristine suspended device with initial $\delta V_{\text{rms}} = 0.79 \pm 0.04$ mV was exposed to a 1 μM concentration of horse heart cytochrome-c (HHCC) purchased from Sigma-Aldrich. Horse heart cytochrome-c is a globular protein which has been shown previously to bind to CNTs.^{28,29} After introducing 1 μM HHCC and observing a shift in the transistor curve (Supporting Information figure 3.7), the device was returned to the original buffer system where charge noise measurements showed $\delta V_{\text{rms}} = 1.26 \pm 0.15$ mV (Figure 3.3c). This HHCC coating experiment was performed on 5 more suspended devices, in

all cases δV_{rms} increased (Supporting Information Table S1). Additional molecular-coating experiments were performed using 25 kDa poly-L-lysine (PLL) purchased from NANOCS. Similar increases in δV_{rms} were observed after adsorption of PLL on the suspended CNTs (Supporting Information Table S1). In all cases the noise spectrum retained a $1/f$ dependence.

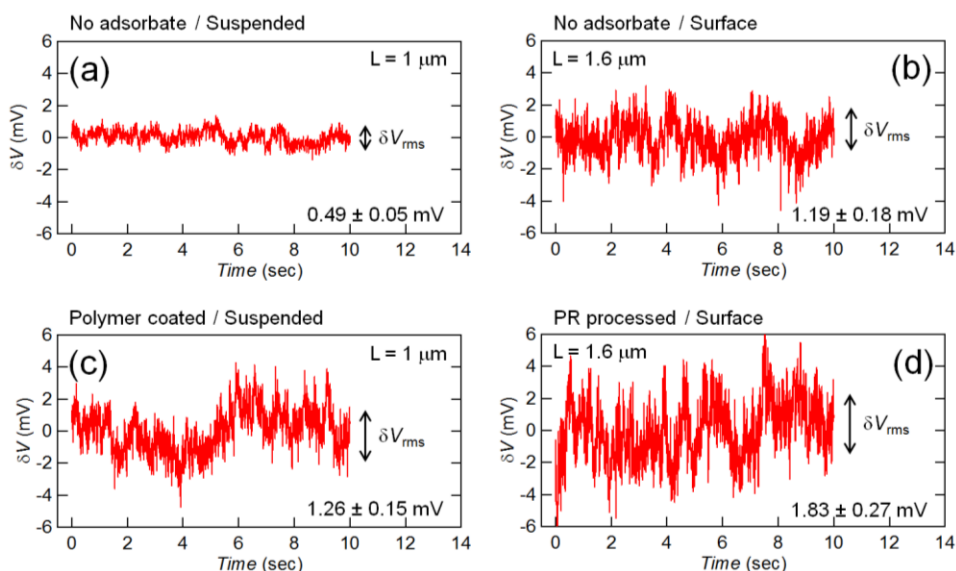


Figure 3.3. Environmental charge noise of single CNT devices operating in solution of 5 mM PB. (a) Pristine suspended CNT. (b) Pristine surface-bound CNT. (c) HHCC coated suspended CNT. (d) Photoresist processed surface-bound CNT.

We also performed measurements of δV_{rms} on surface-bound CNTs before and after exposure to adsorbate molecules. The surface-bound CNTs were produced by the fast-heat CVD method to ensure they were initially adsorbate free. Initial charge noise measurements in PB showed $\delta V_{\text{rms}} = 1.19 \pm 0.18$ mV (channel length $L = 1.6$ μm) (Figure 3.3b). The device was then covered in PR (Shipley S1813) and baked at 115 $^{\circ}\text{C}$ for 90 seconds. The PR was removed with hot acetone and charge noise measurements were repeated, showing $\delta V_{\text{rms}} = 1.83 \pm 0.27$ mV (Figure 3.3d). The charge noise measured from this ‘doubly dirty’ device (both substrate interactions and adsorbates) is in close agreement with the previous results of Mannik et al.¹⁰

By comparing δV_{rms} between different environments (as illustrated in Fig. 3) we can estimate the relative contributions of different noise sources. Differences in channel length can be accounted for by noting that $\delta V_{\text{rms}} \sim L^{-1/2}$.¹⁰ We assume that “intrinsic noise”, substrate noise and adsorbate noise are uncorrelated such that:

$$(\delta V_{\text{rms}})^2 = (\delta V_{\text{rms}}^{\text{intrinsic}})^2 + (\delta V_{\text{rms}}^{\text{adsorbate}})^2 + (\delta V_{\text{rms}}^{\text{substrate}})^2. \quad (2)$$

For measurements taken before and after the addition of adsorbates, we assume that the noise increase is due to $\delta V_{\text{rms}}^{\text{adsorbate}}$. Using Eq.2, we find an average value for $\delta V_{\text{rms}}^{\text{adsorbate}}(L = 1 \mu\text{m}) = 1.1 \text{ mV}$ for a HHCC and PLL coatings. The PR experiment that was performed with a surface-bound CNT with $L = 1.6 \mu\text{m}$, suggests that $\delta V_{\text{rms}}^{\text{adsorbate}}(L = 1 \mu\text{m}) = 1.8 \text{ mV}$ for a PR coating. Lastly, comparing the adsorbate-free surface-bound CNT to our lowest-noise suspended CNT suggests $\delta V_{\text{rms}}^{\text{substrate}}(L = 1 \mu\text{m}) = 1.4 \text{ mV}$. We conclude that substrate interactions and molecular coatings contribute similar levels of electrostatic noise. The quietest devices are suspended and free of protein or polymer adsorbates.

3.6 Microscopic origins of noise

We finish by considering the microscopic origins of charge noise in nanoFET biosensor systems. Previous authors have discussed how the trapping/detrapping of charge inside oxides and on oxide surfaces can lead to $1/f$ noise in nanoFETs (see for example Ref. 16). However, charge traps in oxides cannot explain our observations of suspended CNTs and the effect of adsorbates. Surface adsorbates likely introduce new types of charge traps. One possibility is weak acid/base groups that trap protons from aqueous solution. Following this reasoning, we speculate that a source of charge noise in our biosensor system is the protonation/deprotonation of chemical moieties such as silanol groups on a SiO_2 substrate, and carboxy or amine groups on proteins/polymers. It is already known that such acid/base groups are responsible for the pH sensitivity of

nanoFET biosensors,³⁰ and that increasing the surface density of acid/base groups will increase the sensor's response to a pH change. Therefore, we predict a positive correlation between charge noise and the sensor's response to a pH change.

We tested this prediction by measuring the pH-induced shift in threshold voltage ΔV_{th} of suspended CNTs before and after exposure to PLL and HHCC. As shown in Figure 3.4a, before the PLL coating, we measure $\Delta V_{th} = 5$ mV (measured in 5 mM MES at pH = 7 versus pH = 6). This intrinsic pH sensitivity of the clean suspended CNT may be due to protonation of the CNT surface.³¹ The same device after the PLL coating shows a measurable increase in ΔV_{th} as shown in Figure 3.4c. Increased pH-sensitivity of ΔV_{th} was also observed after pristine suspended CNTs were exposed to HHCC. In all measurements of suspended CNTs, increased pH-sensitivity was correlated with larger δV_{rms} . Additional measurements were conducted on surface-bound CNTs. The pH sensitivity of a clean CNT on a SiO₂ surface is shown in Fig 4b. Both the δV_{rms} and ΔV_{th} are larger than compared to the pristine suspended CNT. However, upon addition of PR residue to the clean surface-bound CNT, ΔV_{th} decreased (Fig. 4d).

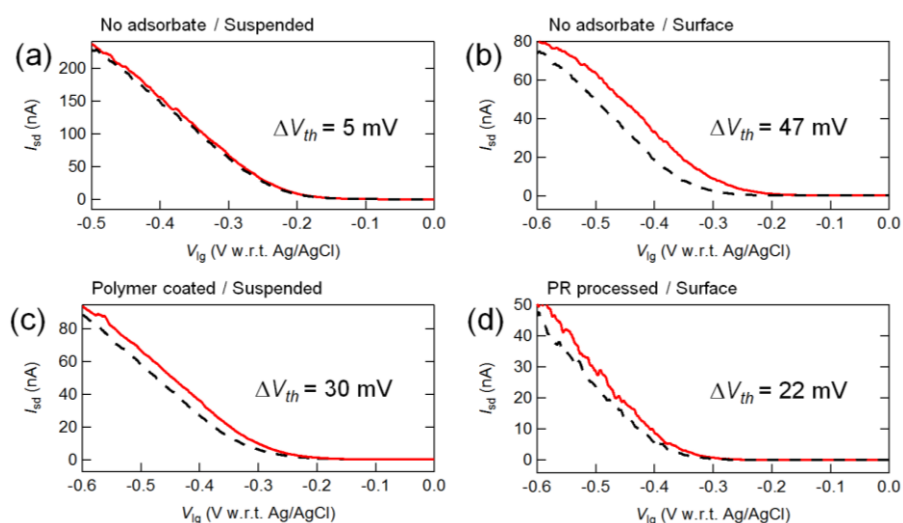


Figure 3.4. Transistor curves taken in 5 mM MES at pH 6 (dashed line) and pH 7 (solid line). (a) Pristine suspended CNT. (b) Pristine surface-bound CNT. (c) PLL coated suspended CNT. (d) Photoresist processed surface-bound CNT.

Figure 3.4 shows that $\Delta V_{th} > 5$ mV is a clear indication that a CNT is in contact with proteins/polymers or a SiO₂ surface. The data also demonstrates that CNT conductance is coupled to the protonation/deprotonation state of nearby surfaces. While δV_{rms} and ΔV_{th} both increase when a clean CNT comes into contact with proteins/polymers or a SiO₂ surface, we cannot use ΔV_{th} alone as a simple predictor of δV_{rms} . As shown in Fig. 3d and Fig. 4d, the combination of PR residue and a SiO₂ surface leads to smaller ΔV_{th} , yet larger δV_{rms} . One possible explanation is that PR residue slows down the time scales of protonation/deprotonation of silanol groups, leading to a larger power spectral density in our measurement bandwidth. Alternatively, PR residue might create an additional type of interface charge trap that is not pH sensitive. Further experiments and simulations will be necessary to verify which type of charge trap dominates the charge noise in a particular situation.

3.7 Conclusion

In conclusion, we have demonstrated that contact with substrates and adsorbates significantly increases the charge noise in CNT FET biosensors. For a 1 μ m channel length, and a measurement bandwidth of 0.1-100Hz, the effective gate voltage fluctuations are approximately 0.5 mV (pristine suspended), 1.1 mV (with PLL or HHCC), 1.8 mV (with substrate interactions), 2.3 mV (with substrate interactions and PR residue). We speculate that the fluctuating protonation state of chemical moieties near the CNT can account for this noise. Our results bring to light new design considerations for nanoFETs that are used to interface biological systems with electronics.

3.8 Acknowledgement

We thank Kerstin Blank and Sophie Ripp for valuable discussions. This work was supported by the Oregon Nanoscience and Microtechnologies Institute (ONAMI) and the Human Frontiers Science Program (HFSP). Sample fabrication was performed at the MaSC Facility at Oregon State University and the Cornell node of the National Nanofabrication Infrastructure Network, which is supported by the National Science Foundation (Grant ECS-0335765).

3.9 Supporting Information

A. Supporting information for Figure 3.6: Variability of Platinum electrode at the trench interface

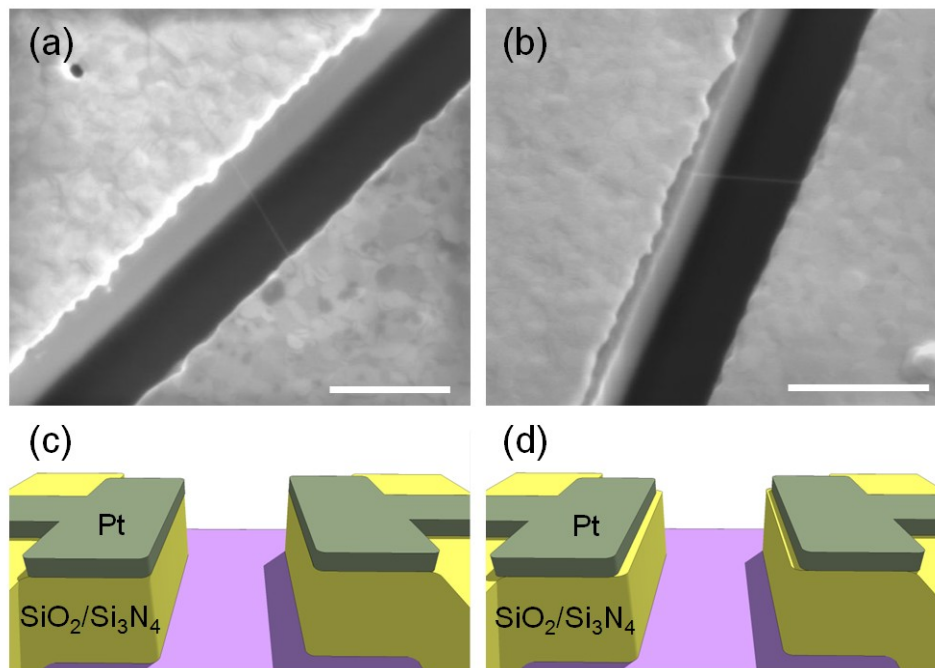


Figure 3.5. SEM images illustrating device variability at the CNT-trench interface occurring after the fast-heat CVD CNT growth process, scale bars are 1 μm . (a) Ideal electrode geometry with Pt electrodes extending to the edge of the trench. (b) Non-ideal electrode geometry. The Pt has receded from the edge of the trench. The CNT can touch the exposed insulating surface before crossing the trench. (c) Schematic of the ideal electrode geometry. (d) Schematic of the non-ideal electrode geometry.

B. Supporting information for Figure 3.7: Pristine suspended device exposed to 1 μM HHCC

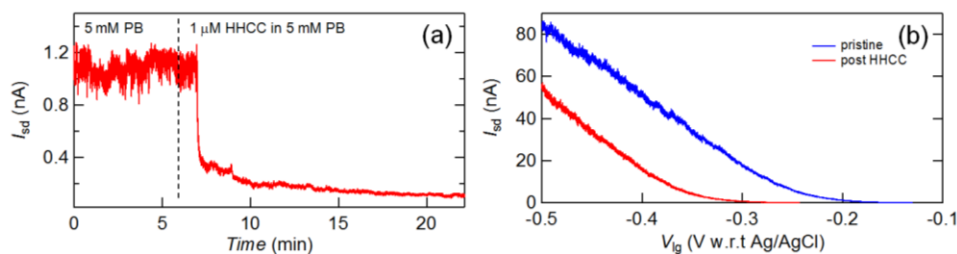


Figure 3.6. Horse heart cytochrome-c (HHCC) binding to the surface of a clean suspended CNT. (a) Current vs. time as a 1 μM concentration of HHCC is introduced. $V_{\text{sd}} = 25 \text{ mV}$ and $V_{\text{lg}} = -200 \text{ mV}$. (b) Current vs. V_{lg} before and after exposure to HHCC. $V_{\text{sd}} = 25 \text{ mV}$.

C. Supporting information for Figure 3.8: Pristine suspended device exposed to 200 nM PLL

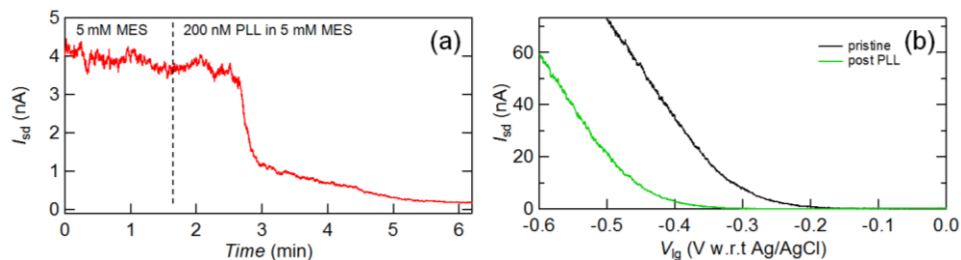


Figure 3.7. Poly-L-lysine (PLL) binding to the surface of a clean suspended CNT. (a) Current vs. time as a 200 nM concentration of PLL is introduced. $V_{sd} = 25$ mV and $V_{ig} = -250$ mV. (b) Current vs. V_{ig} before and after exposure to PLL. $V_{sd} = 25$ mV.

D. Supporting information for Table 3.1: Suspended CNT noise increase after protein coating

Protein	$\delta V_{rms}^{before} (mV)$	$\delta V_{rms}^{after} (mV)$	$\delta V_{rms}^{adsorbate} (mV)$
HHCC	0.79	1.26	0.98
HHCC	1.14	1.44	0.88
HHCC	1.18	1.41	0.77
HHCC	0.85	2.86	2.73
HHCC	0.63	0.83	0.54
PLL	0.87	1.67	1.42
PLL	1.12	1.46	0.94
PLL	0.65	0.91	0.64
			$\langle \delta V_{rms}^{adsorbate} \rangle = 1.11 \pm 0.71$

Table 3.1 shows a large spread in $\delta V_{rms}^{adsorbate}$ values. The source of this variance is currently unknown and warrants further study. It is possible that the variance reflects the way that adsorbates pack on the CNT surface.

3.10 References

- 1 Choi, Y. K. *et al.* Single-Molecule Lysozyme Dynamics Monitored by an Electronic Circuit. *Science* **335**, 319-324, doi:DOI 10.1126/science.1214824 (2012).
- 2 Choi, Y. *et al.* Single-Molecule Dynamics of Lysozyme Processing Distinguishes Linear and Cross-Linked Peptidoglycan Substrates. *J Am Chem Soc* **134**, 2032-2035, doi:Doi 10.1021/Ja211540z (2012).
- 3 Sorgenfrei, S. *et al.* Label-free single-molecule detection of DNA-hybridization kinetics with a carbon nanotube field-effect transistor. *Nat Nanotechnol* **6**, 125-131, doi:DOI 10.1038/nnano.2010.275 (2011).
- 4 Duan, X. J. *et al.* Intracellular recordings of action potentials by an extracellular nanoscale field-effect transistor. *Nat Nanotechnol* **7**, 174-179, doi:Doi 10.1038/Nnano.2011.223 (2012).
- 5 Gao, R. X. *et al.* Outside Looking In: Nanotube Transistor Intracellular Sensors. *Nano Lett* **12**, 3329-3333, doi:Doi 10.1021/Nl301623p (2012).
- 6 Jiang, Z., Qing, Q., Xie, P., Gao, R. X. & Lieber, C. M. Kinked p-n Junction Nanowire Probes for High Spatial Resolution Sensing and Intracellular Recording. *Nano Lett* **12**, 1711-1716, doi:Doi 10.1021/Nl300256r (2012).
- 7 Robinson, J. T. *et al.* Vertical nanowire electrode arrays as a scalable platform for intracellular interfacing to neuronal circuits. *Nat Nanotechnol* **7**, 180-184, doi:Doi 10.1038/Nnano.2011.249 (2012).
- 8 Allen, B. L., Kichambare, P. D. & Star, A. Carbon nanotube field-effect-transistor-based biosensors. *Adv Mater* **19**, 1439-1451, doi:DOI 10.1002/adma.200602043 (2007).
- 9 Tersoff, J. Low-frequency noise in nanoscale ballistic transistors. *Nano Lett* **7**, 194-198, doi:Doi 10.1021/Nl062141q (2007).
- 10 Mannik, J., Heller, I., Janssens, A. M., Lemay, S. G. & Dekker, C. Charge noise in liquid-gated single-wall carbon nanotube transistors. *Nano Lett* **8**, 685-688, doi:Doi 10.1021/Nl073271h (2008).
- 11 Deshpande, V. V. *et al.* Mott Insulating State in Ultraclean Carbon Nanotubes. *Science* **323**, 106-110, doi:DOI 10.1126/science.1165799 (2009).

- 12 Bushmaker, A. W., Deshpande, V. V., Bockrath, M. W. & Cronin, S. B. Direct observation of mode selective electron-phonon coupling in suspended carbon nanotubes. *Nano Lett* **7**, 3618-3622, doi:DOI 10.1021/NI071840f (2007).
- 13 Steele, G. A., Gotz, G. & Kouwenhoven, L. P. Tunable few-electron double quantum dots and Klein tunnelling in ultraclean carbon nanotubes. *Nat Nanotechnol* **4**, 363-367, doi:Doi 10.1038/Nnano.2009.71 (2009).
- 14 Wang, Z. H. *et al.* Phase Transitions of Adsorbed Atoms on the Surface of a Carbon Nanotube. *Science* **327**, 552-555, doi:DOI 10.1126/science.1182507 (2010).
- 15 Kong, J., LeRoy, B. J., Lemay, S. G. & Dekker, C. Integration of a gate electrode into carbon nanotube devices for scanning tunneling microscopy. *Appl Phys Lett* **86**, Doi 10.1063/1.1883301 (2005).
- 16 Lin, Y. M., Tsang, J. C., Freitag, M. & Avouris, P. Impact of oxide substrate on electrical and optical properties of carbon nanotube devices. *Nanotechnology* **18**, Doi 10.1088/0957-4484/18/29/295202 (2007).
- 17 Sharf, T., Kevek, J. W. & Minot, E. D. Fabrication of low-noise carbon nanotube field-effect transistor biosensors. *Nanotechnology (IEEE-NANO), 2011 11th IEEE Conference on* **11**, 122-125, doi:10.1109/NANO.2011.6144640 (2011).
- 18 Dresselhaus, M. S., Dresselhaus, G., Saito, R. & Jorio, A. Raman spectroscopy of carbon nanotubes. *Phys Rep* **409**, 47-99, doi:DOI 10.1016/j.physrep.2004.10.006 (2005).
- 19 Lee, J. S. *et al.* Origin of gate hysteresis in carbon nanotube field-effect transistors. *J Phys Chem C* **111**, 12504-12507, doi:Doi 10.1021/Jp074692q (2007).
- 20 Kim, W. *et al.* Hysteresis caused by water molecules in carbon nanotube field-effect transistors. *Nano Lett* **3**, 193-198, doi:Doi 10.1021/NI0259232 (2003).
- 21 Muoth, M. *et al.* Hysteresis-free operation of suspended carbon nanotube transistors. *Nat Nanotechnol* **5**, 589-592, doi:Doi 10.1038/Nnano.2010.129 (2010).
- 22 Balasubramanian, K., Burghard, M., Kern, K., Scolari, M. & Mews, A. Photocurrent imaging of charge transport barriers in carbon nanotube devices. *Nano Lett* **5**, 507-510, doi:Doi 10.1021/NI050053k (2005).

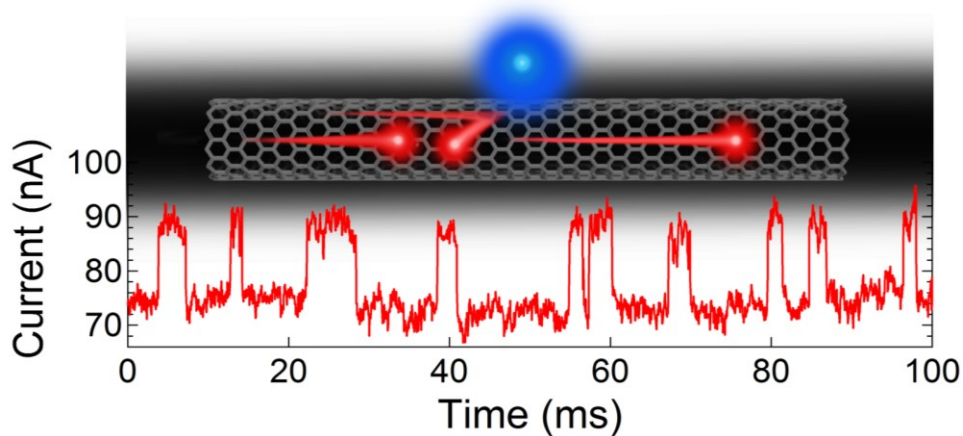
- 23 Minot, E. D. *et al.* Carbon nanotube biosensors: The critical role of the reference electrode. *Appl Phys Lett* **91**, doi:Artn 093507 Doi 10.1063/1.2775090 (2007).
- 24 Rosenblatt, S. *et al.* High performance electrolyte gated carbon nanotube transistors. *Nano Lett* **2**, 869-872, doi:Doi 10.1021/Nl025639a (2002).
- 25 Collins, P. G., Fuhrer, M. S. & Zettl, A. 1/f noise in carbon nanotubes. *Appl Phys Lett* **76**, 894-896 (2000).
- 26 Ishigami, M. *et al.* Hooge's constant for carbon nanotube field effect transistors. *Appl Phys Lett* **88**, doi:Artn 203116 Doi 10.1063/1.2206685 (2006).
- 27 Briman, M., Bradley, K. & Gruner, G. Source of 1/f noise in carbon nanotube devices. *J Appl Phys* **100**, doi:Artn 013505 Doi 10.1063/1.2210570 (2006).
- 28 Heering, H. A., Williams, K. A., de Vries, S. & Dekker, C. Specific vectorial immobilization of oligonucleotide-modified yeast cytochrome c on carbon nanotubes. *Chemphyschem* **7**, 1705-1709, doi:DOI 10.1002/cphc.200600108 (2006).
- 29 Heller, I. *et al.* Identifying the mechanism of biosensing with carbon nanotube transistors. *Nano Lett* **8**, 591-595, doi:Doi 10.1021/Nl072996i (2008).
- 30 Cui, Y., Wei, Q. Q., Park, H. K. & Lieber, C. M. Nanowire nanosensors for highly sensitive and selective detection of biological and chemical species. *Science* **293**, 1289-1292 (2001).
- 31 Strano, M. S. *et al.* Reversible, band-gap-selective protonation of single-walled carbon nanotubes in solution. *J Phys Chem B* **107**, 6979-6985, Doi 10.1021/Jp027664a (2003).

CHAPTER 4

Single Electron Charge Sensitivity of Liquid-Gated Carbon Nanotube Transistors

Tal Sharf, Neng-Ping Wang, Joshua W. Kevek, Morgan A. Brown, Heather Wilson, and Ethan D. Minot

Just accepted: Nano Letters 2014



Random telegraph signals corresponding to activated charge traps were observed with liquid-gated CNT FETs. The high signal-to-noise ratio that we observe demonstrates that single electron charge sensing is possible with CNT FETs in liquids at room temperature. We have characterized the gate-voltage dependence of the random telegraph signals and compared to theoretical predictions. The gate-voltage dependence clearly identifies the sign of the activated trapped charge.

4.1 Introduction

The pursuit to miniaturize transistor technologies down to nanometer scale dimensions has been driven by a demand for low power, high performance and high sensitivity electronic applications. Carbon nanotube field-effect transistors (CNT FETs) are promising candidates to satisfy these demands. Technological advances in device designs have paved the way for scalable CNT based digital switches,^{1,2} which combined with recent advances in CNT synthesis offer an alternate route to silicon based technologies.^{3,4} Additionally, the remarkable sensitivity of CNT FET sensors has recently been used to measure single-molecule processes such as DNA hybridization,⁵ single chemical reactions⁶ and single enzyme activity.⁷ These measurements are sensitive to molecules carrying a handful of charges, suggesting that CNTs can reach single electron charge sensitivity in liquids at room temperature.

The high sensitivity of CNT FETs comes at the price of ever-present charge noise. Charge noise is typically manifested as stochastic current fluctuations with a power spectral density that scales inversely with frequency (f). In typical CNT devices this $1/f$ noise spectrum is attributed to a large number of charge traps near the CNT channel. The charge noise model developed by Tersoff assumes a capacitive coupling between these fluctuating charge traps and the CNT channel.⁸ Tersoff's model has been experimentally verified for both liquid-gated CNT FETs and graphene FETs.^{9,10}

In small devices, such as CNT FETs, a single charge trap can have a disproportionately large influence, leading to the observation of a random telegraph signal (RTS) when measuring conductance vs. time.¹¹⁻¹⁸ For example, one charge trap might be located a few Angstroms from the CNT channel, while all other traps are more distant. Random telegraph signals in CNT FETs have been studied extensively at low temperature,¹³⁻¹⁸ and two studies have reported RTS at room temperature, demonstrating that single charge sensitivity is possible

in air and vacuum.^{11,12} This previous work has also verified the gate-dependent capture time and emission time can be understood in a framework developed for RTS in metal-oxide-semiconductor FET devices.¹⁹

In this work we explore RTS at room temperature in electrolyte-gated CNT FETs. The electrolyte gate ensures almost perfect coupling between the gate voltage and the Fermi level in the CNT, allowing clear comparisons between experiment and theory. The elevated temperature ensures that charge hopping between the CNT and the trap state occurs over a wide range of gate voltages. While previous experiments have characterized RTS switching dynamics (capture times and emission times), we focus on the gate-dependent amplitude of the RTS signal. We compare our results to non-equilibrium Green's function (NEGF) calculations of scattering from a Coulomb potential created by a point charge. Our measurements confirm theoretical predictions for the gate voltage dependence of the RTS amplitude.²⁰ Our results are a key test of the NEGF modeling approach and open a path to rational design of single molecule electronic detectors.

4.2 Device architecture

Carbon nanotube devices were fabricated using standard photolithography and metal deposition techniques (see Methods). Figure 4.1a shows a schematic diagram of the device geometry utilized for performing measurements on surface-bound CNT FETs while operating in liquid environments. The CNTs were grown as a final processing step using 'fast heat' chemical vapor deposition which yields ultra-clean devices.²¹ Devices with single CNTs were verified by AFM characterization as shown in Figure 4.1c. Semiconducting CNT devices were chosen for electronic measurements with a diameter range of 1-2 nm. For measurements on suspended CNT devices, a reactive ion etch was used to remove the SiO₂/Si₃N₄ between a 1 μm source-drain electrode gap, producing an ideal geometry to grow ultra-clean suspended CNT devices (Figure 4.1b,d).²² A home-built laminar flow cell was used to interface the CNT devices with 10 mM phosphate buffer (PB). The Debye screening length of this electrolyte solution is

~ 3 nm. The solution potential V_g was set by a Ag/AgCl reference electrode²³ or on-chip Pt electrode. Electrochemical currents between the liquid and the CNT device never exceeded 100 pA.

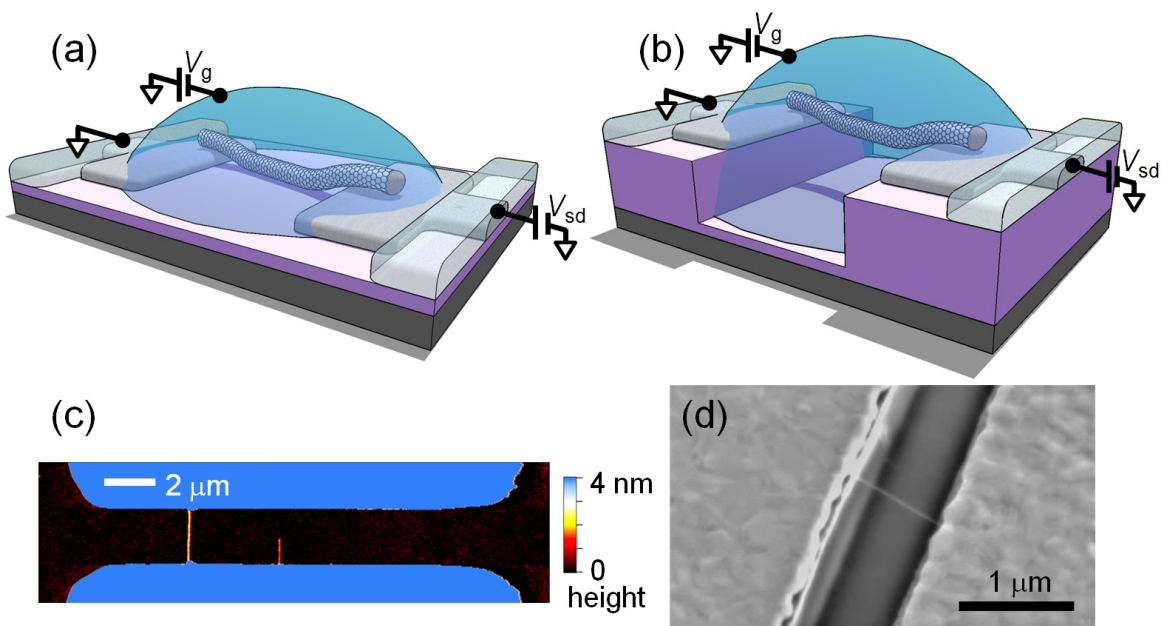


Figure 4.1. (a) Schematic diagram of a single CNT device operating in liquid. (b) Diagram of a suspended CNT device (c) Surface topology map of a single CNT device measured by AFM. (d) Scanning electron micrograph of a single suspended CNT device.

4.3 Substrate induced RTS noise in CNT FETs.

Figure 4.2a shows current versus time, $I(t)$, measured from a single surface-bound CNT operating in a solution of 10 mM PB. Switching events occur between two well-defined levels of current, which are defined by a high-current state I_{high} and a low-current state I_{low} . Random telegraph signals such as Figure 4.2a were observed in 8 out of 24 surface-bound devices (see Supporting Info part A for CNT and charge trap spatial overlap probabilities). The other 16 surface-bound devices exhibited fluctuating $I(t)$ about a single current level. The power spectral density of these $I(t)$ fluctuations exhibited a $1/f$ spectrum as previously reported by Mannik et al.⁹ Figure 4.2b shows an equivalent measurement performed on an ultra-clean suspended device in similar conditions. We measured

a total of 16 suspended CNTs and none showed RTS. For these suspended CNTs, the power spectral density of $I(t)$ fluctuations was also significantly less.²²

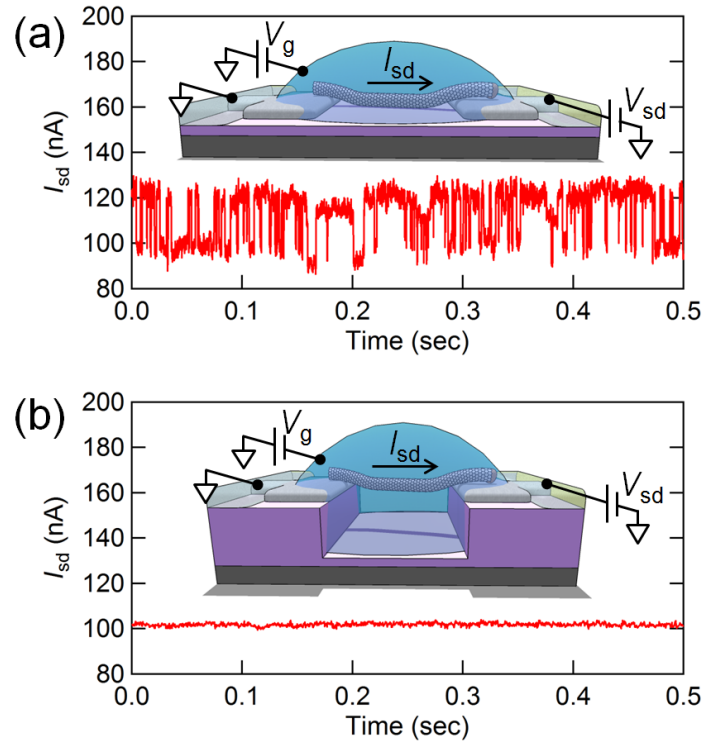


Figure 4.2. (a) Two-level current noise exhibited by a single surface-bound CNT device operating in 10 mM PB. (b) Current measured through a suspended device operating in the same conditions as (a).

Based on the comparison of surface-bound and suspended CNTs (Fig. 2) we conclude that the dielectric substrate is responsible for the observed RTS. When the chemical potential for electrons in the CNT coincides with the energy level of trap state, the occupancy of the trap can fluctuate. Following previous work, we attribute I_{low} and I_{high} to the fluctuating occupancy of such a trap.

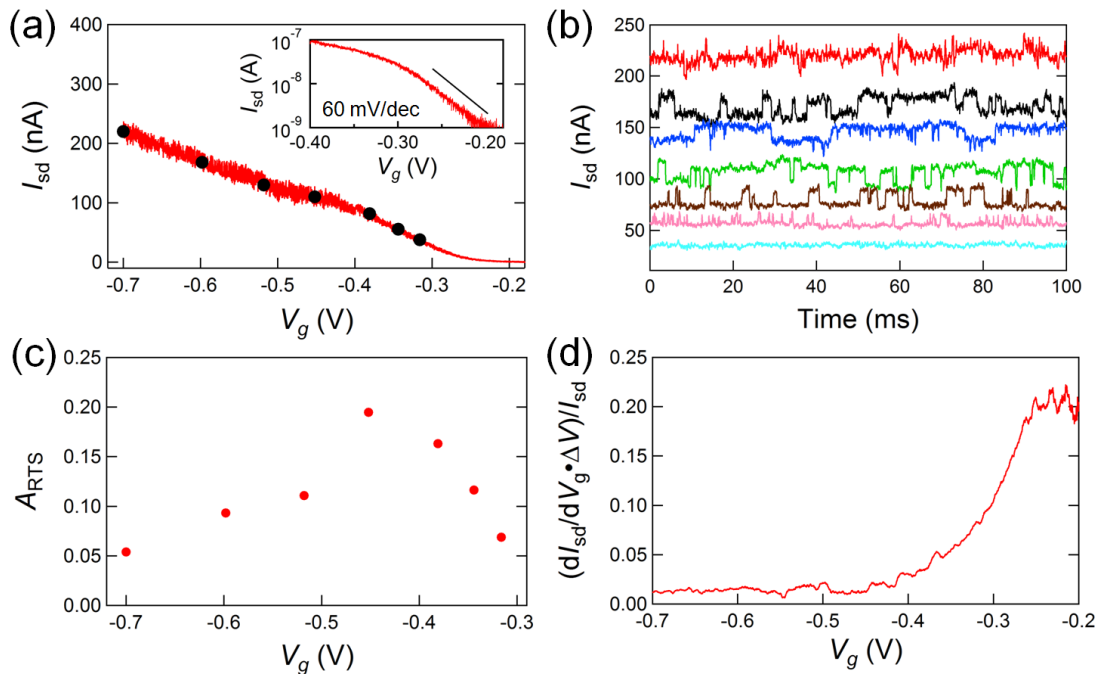


Figure 4.3. (a) Transistor curve of a surface-bound CNT FET exhibiting RTS current noise in 10 mM PB. The solid circles show where current was collected. The inset shows the exponential subthreshold regime. (b) Current noise measured as at fixed values of V_g shown as solid circles in (a). (c) Fractional change in current (A_{RTS}) plotted as a function of gate voltage. (d) Fractional change in current predicted by doping mechanism for fixed jump in potential of $\Delta V = 5$ mV.

4.4 Gate-dependence of trap occupation

We first examine the relative probability of finding the device in the I_{high} state versus the I_{low} state. Figure 4.3 shows RTS measured from a surface-bound CNT at a variety of gate voltages, V_g . The $I(V_g)$ characteristic of the device is shown in Figure 4.3a. At $V_g < \sim -0.3$ V the CNT is p-doped and has relatively high conductance. For $V_g > \sim -0.3$ V, the conductance begins to follow an exponential decay (see inset of Figure 4.3a), indicative of the subthreshold regime where the Fermi level enters the bandgap. Figure 4.3b shows time traces, $I(t)$, obtained at different values of V_g . The time-averaged current drops as V_g is increased from -0.7 to -0.2 V. At negative gate voltages, the high-current state is favored. At positive gate voltages, the low-current state is favored. Following the interpretation of Ralls et al.¹⁹ we conclude that a negative scattering center turns

on by electron capture. i.e. at negative gate voltages the trap state is neutral, at positive gate voltages an electron spills out of the CNT into the trap state, at intermediate gate voltages the trap fluctuates between filled and empty (see Supporting Info part B).

Two out of 8 devices showed gate-dependent trap occupation that was consistent with electron capture by a neutral trap state. In other devices, the liquid gate voltage had no effect on emission and capture times. A possible explanation for unperturbed emission and capture times is an extreme proximity between the trap and the CNT. If the capacitive coupling between the trap and the CNT is extremely strong, the liquid gate voltage will not change the relative energy difference.

4.5 Doping effect vs. mobility effect

When a trap state captures a charge, both the doping level and the effective mobility of the CNT are affected. NEGF simulations give insight into distinguishing these two effects. A distant charge will cause a smooth variation in potential and effectively change the doping level in the CNT. If the charge is more than ~ 3 nm away from the CNT, NEGF simulations predict that the change in current is simply proportional dI_{sd}/dV_g .²⁰ Experiments that measure conductance fluctuations in CNT FETs (the collective result of many charge traps) support this model.^{9,22} In contrast, when the charge is closer than ~ 3 nm, NEGF simulations predict that electron scattering becomes significant and the change in current is not simply proportional to dI_{sd}/dV_g .

To determine whether our RTS measurements can be described by doping, we plot the prediction for A_{RTS} ($A_{RTS} = (I_{high} - I_{low})/I_{high}$) caused by a distant charge trap (Fig. 3d). The slope of the transistor curve, dI_{sd}/dV_g , has been multiplied by a fitting parameter, 5 mV, and divided by I_{sd} , yielding a peak $A_{RTS} = 0.2$. The maximal value of A_{RTS} occurs in the subthreshold, and stays constant throughout the subthreshold. In contrast, our measured values of A_{RTS} peak in the on-state, before the subthreshold, and decay in the subthreshold (Fig. 3c). We

carried out detailed $A_{\text{RTS}}(V_g)$ measurements on 3 other devices that exhibited RTS current noise and observed similar trends. We conclude that carrier scattering must be considered to describe the measured RTS.

4.6 Theoretical modeling of RTS amplitude

Wang et al. previously calculated A_{RTS} for a ballistic CNT FETs interacting with a fluctuating single charge (either positive or negative).²⁰ We first discuss the qualitative conclusions from these simulations. For a positive charge trap interacting with a p-type device, $A_{\text{RTS}}(V_g)$ increases monotonically as V_g is tuned from the p-doping to the subthreshold. For a negative charge trap, there is a peak in $A_{\text{RTS}}(V_g)$ when V_g is near the transition between p-doping and the subthreshold regime. Based on these qualitative results, we conclude that our measured $A_{\text{RTS}}(V_g)$ is consistent with the coming and going of a negative charge near the CNT.

We have extended the previous work of Wang et al. to give a more quantitative understanding of our particular experimental system. Our new calculations take into account non-Ohmic contacts between the CNT and the metal electrodes, inelastic scattering in the CNT and the liquid gate geometry. We begin with NEGF simulations of an Ohmically-contacted (13, 0) CNT (diameter 1.04 nm) with a channel length of 200 nm, surrounded by a dielectric of either $\epsilon = 4$ or 10, a cylindrical gate of radius 16 nm, and a negative charge (or no charge) near the sidewall of the CNT (separation distance $d = 0.5$ nm or 1.5 nm). The source-drain voltage is 50 mV and $T = 300$ K. Current is calculated at different gate voltages, both with and without the single electron charge next to the CNT.

First, the parameters used in the NEGF simulation should be consistent with the liquid gated environment. Free ions diffusing in the water lead to an electrostatic screening length of ~ 3 nm, but the simulations only account for screening by free carriers in the CNT. However, the simulated free-carrier screening lengths were 3 nm and shorter when the CNT was p-doped (higher hole concentration at negative gate voltages leads to shorter screening lengths, see

Supporting Info part C), therefore, screening by free ions in the water can be neglected to first order. Similarly, electrolyte gating is not explicitly modeled. Instead, the model uses a perfect cylindrical gate (see Figure 4.4b inset), which allows us to obtain comparable turn-on characteristics to the experimental device. Lastly, the experimental geometry includes two dielectrics, water ($\epsilon = 80$) and SiO₂ ($\epsilon = 4$), but the simulations are performed with a single dielectric constant. Since the charge trap is in the SiO₂, initial calculations were performed with $\epsilon = 4$. Additional calculations with a higher effective epsilon ($\epsilon = 10$) yielded A_{RTS} values that were a factor 2 smaller. If the effective dielectric constant is indeed 10 or higher, the proximity of the charge trap to the CNT, d , must be reduced to obtain agreement between experiment/theory values of A_{RTS} . Our current experiments cannot resolve this uncertainty in ϵ and d .

To translate the results of the NEGF simulations (ballistic transport, Ohmic contacts) into predictions for a diffusive 1d system with non-Ohmic contacts, we make use of the Landauer formalism for addition of incoherent barriers.²⁴ In a diffusive 1d system, the Coulomb barrier associated with a charge trap adds a fixed amount of resistance ΔR to the overall system. ΔR is independent of channel length and contact resistance (see Supporting Info part D for more details). Results from the NEGF simulations allow us to approximate ΔR by calculating $\Delta R^{\text{sim}} = R_0^{\text{sim}} - R_Q^{\text{sim}}$, where R_0^{sim} is the simulated resistance with no charge, and R_Q^{sim} is the simulated resistance with a single charge. The simulated value ΔR^{sim} includes interference effects caused by coherent multiple reflections. These effects are not present in the diffusive transport regime of our experiment, however, multiple reflections are a small correction in the situations studied here ($A_{\text{RTS}} < 0.2$).

Figure 4.4a shows CNT device resistance plotted as a function of gate voltage $R(V_g)$ for both experimental and NEGF simulated results. Our experimental devices have channel lengths of 2 μm (see Fig 1c), which is ~ 3 times larger than the phonon scattering length at room temperature.²⁵ Therefore,

we expect the experimentally measured channel resistance to be 3x more resistive than simulated NEGF data (channel resistance scales linearly with channel length in the diffusive limit²⁵). This insight allows us to map the experimental values of V_g onto the simulated values of V_g (differences between experimental and simulated V_g values are caused by factors such as the choice of liquid gate electrode and surface charges on the SiO_2). The experimentally measured $R(V_g)$ curve has been translated on the V_g access so that the experimental subthreshold resistance is 3 times the subthreshold resistance of the simulation.

Figure 4.4b shows a comparison between ΔR^{sim} and our experimental measurements. The ΔR extracted from the RTS measurements varies from $\sim 7 \text{ k}\Omega$ in the on-state to $\sim 60 \text{ k}\Omega$ near the subthreshold regime (see Supporting Info part E for ΔR data from additional devices). The NEGF simulation results follow a similar trend. In Fig. 4c, the ΔR values have been divided by R_0^{expt} to show the fractional change in resistance. Both NEGF and experiments show that the fractional change is maximized as the device transitions from the on-state to subthreshold regimes.

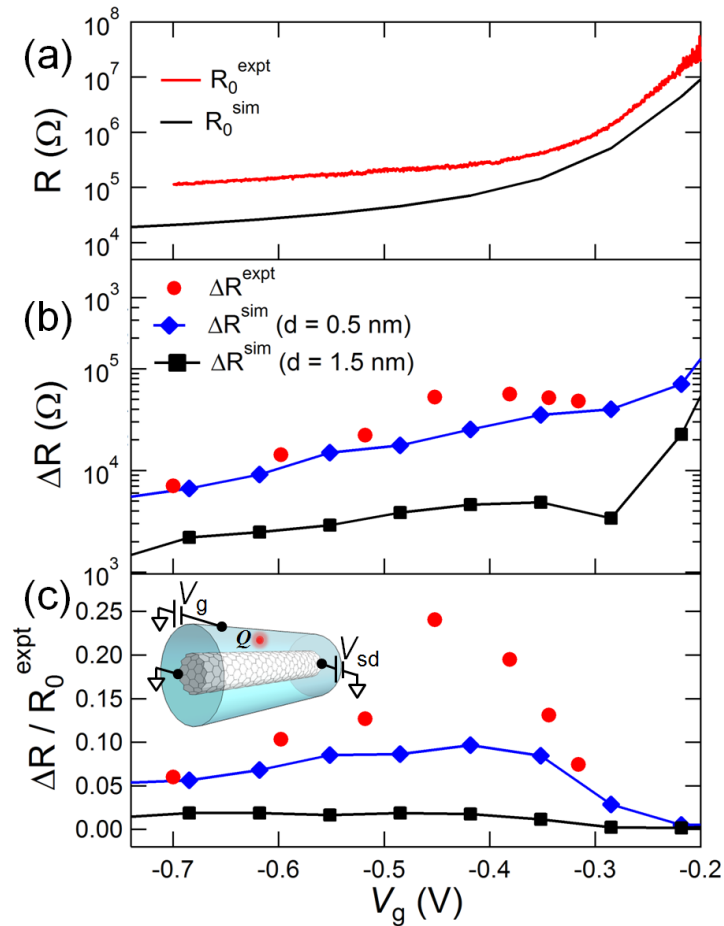


Figure 4.4. (a) Experimentally measured (red line) and NEGF simulated (black line) CNT resistance vs. gate voltage. (b) Change in CNT resistance produced by RTS noise measured as a function gate voltage. Red circles are experimental results extracted from Fig. 3b. Blue diamonds and black squares are NEGF predictions for scattering from a $-1e$ charge placed a distance of 0.5 nm and 1.5 nm from the CNT sidewall respectively. (c) Fractional resistance change where data from (b) is normalized by the baseline experimental resistance R_0^{expt} .

Figure 4.4c highlights the influence of R_0^{expt} on RTS amplitude (note that $\Delta R/R_0^{\text{expt}}$ equals A_{RTS} to within a correction factor of order unity; $\Delta R/R_0^{\text{expt}} = A_{\text{RTS}} \cdot I_0/I_Q$). Large values of the baseline resistance R_0^{expt} will suppress A_{RTS} , therefore, small R_0^{expt} is desirable for sensor applications. Previous work has shown $R_0^{\text{expt}} = \rho L + R_c$, when $L > \lambda_{\text{in}}$; ρ is 1-D resistivity, R_c is contact resistance, L is the channel length, and λ_{in} is the inelastic scattering length.²⁵ Optimal $\Delta R/R_0^{\text{expt}}$ is expected when $L \sim \lambda_{\text{in}}$. Smaller L will not reduce R_0^{expt} , but smaller L will increase background noise ($1/f$ noise) which scales as $1/\sqrt{L}$.⁹

4.7 Dependence of RTS amplitude on carrier type

As a final test of our model, we have measured RTS in n-type CNT FETs. By changing the sign of charge carriers in the CNT channel, we expect a dramatic change in the gate-dependent scattering probability.

Figure 4.5 shows a side-by-side comparison of A_{RTS} in a p-type channel and an n-type channel (measurements from two different devices). The overall A_{RTS} magnitude is similar for the two devices, but the V_g dependence is strikingly different. As discussed above, all p-type devices in our study exhibited maximal A_{RTS} in the on-state. In contrast, the n-type device exhibits maximal A_{RTS} in the subthreshold (blue shaded region), with A_{RTS} remaining approximately constant within the subthreshold. We have observed this behavior for a total of 3 n-type devices.

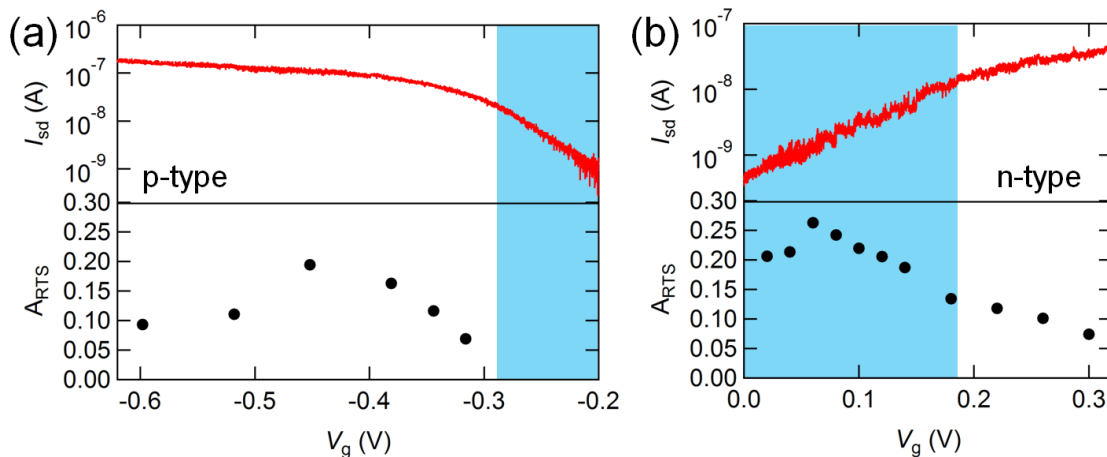


Figure 4.5. Comparison between p-type and n-type CNT FETs that exhibit RTS. (a) Transistor curve for a p-type CNT circuit exhibiting RTS. Fractional change in current is shown in the lower graph. (b) Transistor curve for an n-type CNT circuit exhibiting RTS. Fractional change in current is shown in the lower graph.

The $A_{\text{RTS}}(V_g)$ signature shown in Fig. 5b is consistent with predictions for n-type carriers scattering from a negative charge trap.²⁰ For a trap charge and carrier charge of similar polarity, $\Delta R^{\text{sim}}/R_0^{\text{sim}}$ reaches a maximal plateau in the subthreshold regime. The height of this plateau depends strongly on separation distance d and baseline resistance R_0^{expt} . The data shown in Fig. 5b are consistent

with a separation distance of a few nanometers. From the V_g dependence shown in Fig. 5b we conclude that the relative sign of the trap charge and carrier charge is indeed a critical parameter in determining $A_{\text{RTS}}(V_g)$.

4.8 Conclusion

In a room-temperature liquid environment, CNT FETs are capable of detecting signals generated by the coming and going of a single electron charge. The sign of the charge can be determined by measuring the gate-sensitivity of the RTS magnitude. We find good agreement between our measurements and the predictions of NEGF simulations, opening a path to optimizing the design of single-molecule bioelectronic sensors. Our measurements highlight the need to eliminate charge traps in the dielectrics of high-fidelity nanoelectronic devices, and confirm the exciting possibility of detecting single charges in room-temperature biological environments.

4.9 Methods

Device fabrication. Metal electrodes (1 nm Ti, 50 nm Pt) were patterned on top of Si/SiO₂ (600 μm / 1 μm) substrates or Si/SiO₂/Si₃N₄ (600 μm / 1 μm / 100 nm). The metal electrode leads were passivated with 80 nm of e-gun deposited SiO₂ (excluding the source-drain electrode tips and probe contacts) to prevent Faradaic currents that occur during liquid gating. Catalyst islands (1 nm Ti, 40 nm SiO₂, 1 nm Fe) of dimension 10 μm x 5 μm were patterned on the electrode tips a distance of 4 μm from the edge of the source-drain electrode gap (2 μm). The devices were then diced into 2 mm chips. To prevent electrode degradation during the high temperature CNT growth process, it was crucial to limit chip exposure time to high temperatures. This was accomplished by implementing a quartz loading shuttle attached to a steel ball bearing and shuttling the chips in and out of the hot-zone of a 1" quartz tube furnace with an external magnet. The shuttle growth recipe is as follows: (1) Chips were first shuttle annealed in open air at 600 °C for 5 minutes. (2) The furnace was sealed and allowed to cool below 300 °C, purged for 2 minutes flowing the CNT growth gases (Argon bubbled methanol at 0.3 slm, Argon bubbled ethanol at 0.15 slm and H₂ at 0.45 slm), then

flushed with Ar (1 slm) for 2 minutes to clear the growth gases from the chamber. (3) Chips were then shuttle annealed in H₂ (0.45 slm) for 1 minute at 800 °C. (4) The furnace was ramped to 900 °C in H₂ (0.45 slm), switched over to CNT growth gases and chips were shuttled into the furnace for a 5 minute CNT growth. The chips were cooled outside of the heat-zone under Argon (1 slm) until the heat-zone reached 200 °C, then furnace seals were opened to atmosphere. These growth parameters produced ~10% single CNT connections on surface-based devices with a 2 μm source-drain electrode gap. To achieve similar yields on suspended devices with a 1 μm source-drain channel gap, the growth parameters of step (4) were reduced to 800 °C.

Electrical measurements. Single CNT devices were interfaced with a liquid environment (10 mM PB) using a home-built laminar flow cell. Current was measured through the devices using a Stanford Research Systems model SRS570 current preamplifier (sensitivity 100 nA/V, High bandwidth mode, no filters applied). The source-drain bias (25 mV) was supplied by the bias offset of the SRS570 current preamplifier, which was powered by an internal lead-acid battery. The liquid-gate voltage was applied to Ag/AgCl reference electrode (BASi RE-6) interfaced downstream of the flow cell using a Yokogawa GS210 DC voltage source. Equivalent results were obtained using a lithographically defined on-chip Pt electrode of dimensions 200 μm x 1mm. The electrochemical currents between the liquid-gate and source-drain electrodes never exceeded 100 pA. To gain access to n-type regime of semiconducting CNT devices a tungsten electrode was used to control the solution potential.

4.10 Acknowledgements

We thank David Roundy and Alejandro Cortese for valuable discussions. This work was supported by the Oregon Nanoscience and Microtechnologies Institute (ONAMI) and the Human Frontiers Science Program (HFSP) under grant No. RGY0058/2010. Sample fabrication was performed at the MaSC Facility at Oregon State University and the Cornell node of the National Nanofabrication

Infrastructure Network, which is supported by the National Science Foundation (Grant ECS-0335765). N.-P.W. acknowledges financial support from The National Natural Science Foundation of China under Grant No. 61176081

4.11 Supporting Information

A. Trap density of SiO₂

High quality thermal oxides contain a charge trap density of $\sim 10^{10}$ traps/cm² (100 traps/ μm^2).²⁶ A CNT with a diameter of ~ 1.5 nm and channel length of 2 μm has a $\sim 30\%$ chance of spatially overlapping with a charge trap on such a surface.

B. Relative probability of high-current and low-current states as a function of V_g

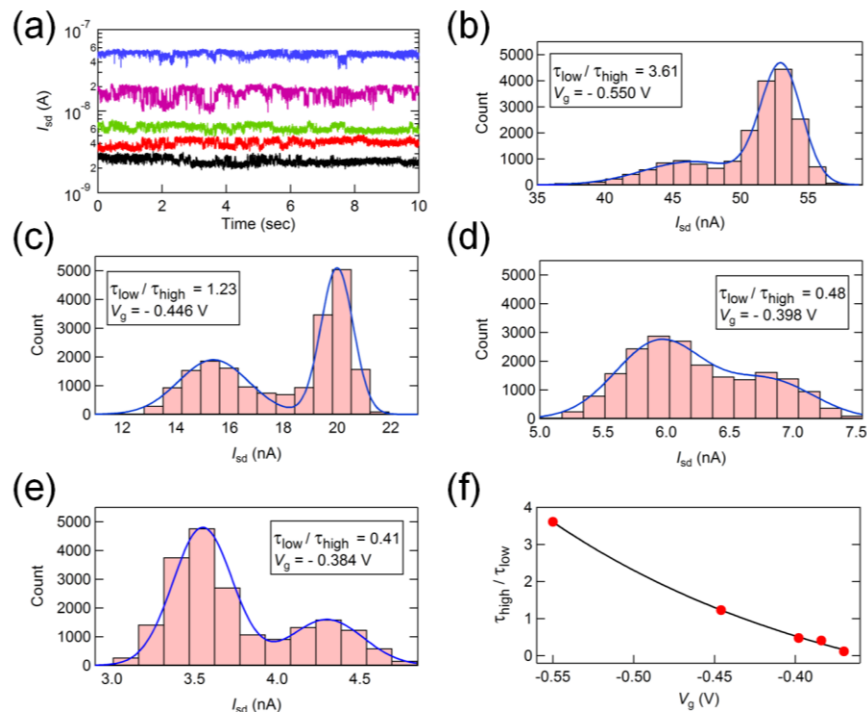


Figure 4.6. (a) Source-drain current measured through a single CNT device with fixed bias ($V_{sd} = 25$ mV) for increasingly negative liquid-gate voltage: $V_g = -0.370$ V (black), -0.384 V (red), -0.398 V (green), -0.446 V (purple), -0.550 V (green). (b-e) Histograms of current vs. time shown in (a). Blue solid line is a fit to a double Gaussian function. (c) Relative ratio of time spent in the high-state current (τ_{high}) to low-state current (τ_{low}) vs. V_g . Black solid line is an exponential fit.

C. Simulated free-carrier screening lengths

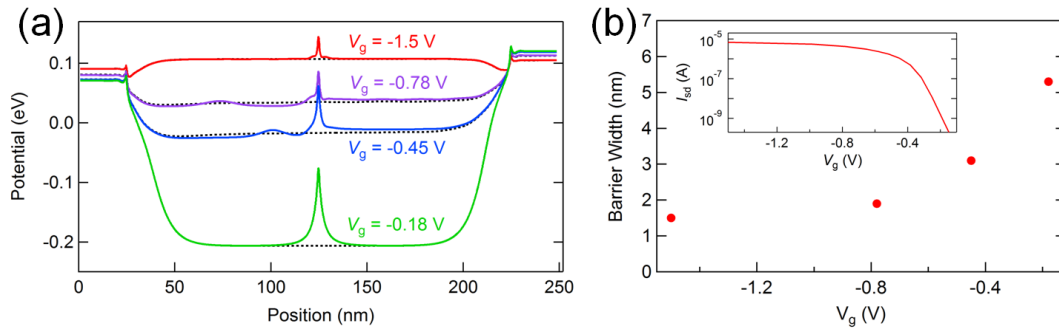


Figure 4.7. (a) Simulated potential along CNT for low ($V_g = -0.18$ V) to high doping ($V_g = -1.5$ V) levels with a charge of $Q = 0$ (dotted lines) and $Q = -1e$ (solid lines) at a distance $d = 0.5$ nm. The source-drain bias is 50 mV. (b) Barrier width (full width half max) the Coulomb potential from (a) as a function of V_g . The inset is the simulated transistor curve for $Q = 0$.

D. The addition of incoherent barriers using the Landauer formalism

In the ballistic limit, the length dependence of A_{RTS} was previously investigated by NEGF simulations.²⁷ In the diffusive limit, which is relevant for describing our current experiments, length dependence can be approximated by considering the Landauer formalism for incoherent addition of barriers in a 1d channel.²⁴ If the electron phase information is destroyed by inelastic scattering from phonons, device resistance is given by

$$R = \frac{h}{4e^2} \left(1 + \sum_i \frac{r_i}{t_i} \right). \quad (4.1)$$

Where r_i and t_i are reflection and transmission probabilities due to interactions with either static barriers or phonons. If an additional static barrier is added, for example, a charged trap with reflection and transmission probabilities r_Q and t_Q , we find

$$R = \frac{h}{4e^2} \left(1 + \sum_i \frac{r_i}{t_i} + \frac{r_Q}{t_Q} \right) = R_0 + \frac{h}{4e^2} \frac{r_Q}{t_Q} = R_0 + \Delta R. \quad (4.2)$$

The baseline resistance, R_0 , can vary widely depending on CNT channel length and contact resistance. However, ΔR is independent of these factors. Therefore, the length dependence of $\Delta R/R_0$ is only due to the length dependence of R_0 .

E. Measurements of ΔR

The magnitude of ΔR was determined for a total of 4 p-type devices (Fig. 4.8). All devices followed the trend reported in the manuscript (A_{RTS} peaks in the on-state and decays in the subthreshold). Comparing experimental ΔR values with NEGF simulations suggests $d < 0.5$ nm in all cases, i.e. the distance between the CNT and the charge trap is less than 0.5 nm. These small values of d are not surprising; if d was much larger, the RTS would be lost in background noise.

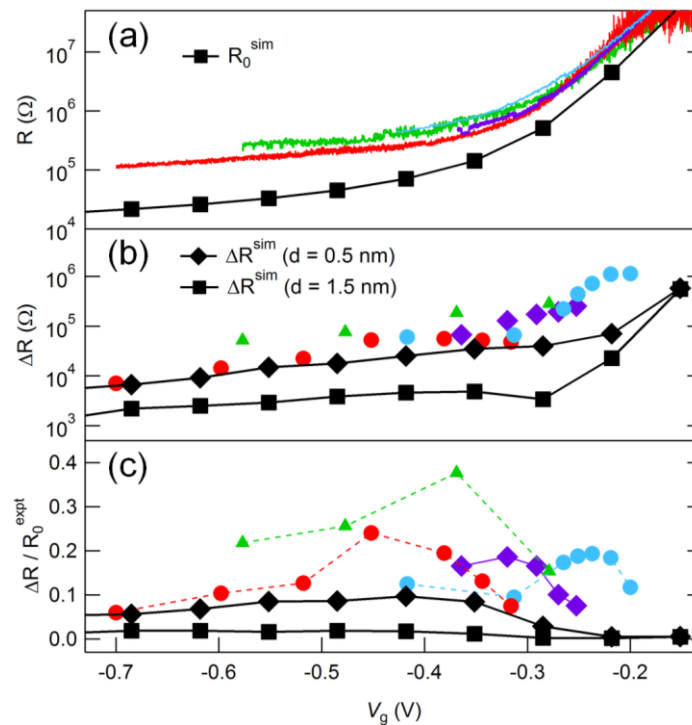


Figure 4.8. (a) Resistance vs. gate-voltage for 4 devices studied experimentally in detail (colored lines). Circles joined by a solid line are the NEGF simulation data for an Ohmically-contacted (13,0) CNT. (b) The change in resistance, ΔR , associated with the RTS. Back diamonds and squares are NEGF predictions for scattering from a $-1e$ charge placed a distance of 0.5 nm and 1.5 nm from the CNT sidewall respectively. (c) Fractional resistance change where data from (b) is normalized by the baseline experimental resistance R_0^{expt} (note that $\Delta R/R_0^{expt}$ equals A_{RTS} to within a correction factor of order unity; $\Delta R/R_0^{expt} = A_{RTS} \cdot I_0/I_Q$).

4.12 References

- 1 Shulaker, M. M. *et al.* Carbon nanotube computer. *Nature* **501**, 526-530, doi:10.1038/nature12502 (2013).
- 2 Franklin, A. D. *et al.* Carbon Nanotube Complementary Wrap-Gate Transistors. *Nano Lett* **13**, 2490-2495, Doi 10.1021/Nl400544q (2013).
- 3 Franklin, A. D. ELECTRONICS The road to carbon nanotube transistors. *Nature* **498**, 443-444 (2013).
- 4 Jin, S. H. *et al.* Using nanoscale thermocapillary flows to create arrays of purely semiconducting single-walled carbon nanotubes. *Nat Nanotechnol* **8**, 347-355, doi:Doi 10.1038/Nnano.2013.56 (2013).
- 5 Sorgenfrei, S. *et al.* Label-free single-molecule detection of DNA-hybridization kinetics with a carbon nanotube field-effect transistor. *Nat Nanotechnol* **6**, 125-131, doi:DOI 10.1038/nnano.2010.275 (2011).
- 6 Goldsmith, B. R., Coroneus, J. G., Kane, A. A., Weiss, G. A. & Collins, P. G. Monitoring single-molecule reactivity on a carbon nanotube. *Nano Lett* **8**, 189-194, doi:Doi 10.1021/N10724079 (2008).
- 7 Choi, Y. K. *et al.* Single-Molecule Lysozyme Dynamics Monitored by an Electronic Circuit. *Science* **335**, 319-324, doi:DOI 10.1126/science.1214824 (2012).
- 8 Tersoff, J. Low-frequency noise in nanoscale ballistic transistors. *Nano Lett* **7**, 194-198, doi:Doi 10.1021/Nl062141q (2007).
- 9 Mannik, J., Heller, I., Janssens, A. M., Lemay, S. G. & Dekker, C. Charge noise in liquid-gated single-wall carbon nanotube transistors. *Nano Lett* **8**, 685-688, doi:Doi 10.1021/Nl073271h (2008).
- 10 Heller, I. *et al.* Charge Noise in Graphene Transistors. *Nano Lett* **10**, 1563-1567, doi:Doi 10.1021/Nl903665g (2010).
- 11 Peng, H. B., Hughes, M. E. & Golovchenko, J. A. Room-temperature single charge sensitivity in carbon nanotube field-effect transistors. *Appl Phys Lett* **89**, Doi 10.1063/1.2399942 (2006).
- 12 Chan, J. *et al.* Reversal of current blockade in nanotube-based field effect transistors through multiple trap correlations. *Phys Rev B* **80**, doi:Artn 033402 Doi 10.1103/Physrevb.80.033402 (2009).

- 13 Liu, F. *et al.* Giant random telegraph signals in the carbon nanotubes as a single defect probe. *Appl Phys Lett* **86**, doi:Artn 163102 Doi 10.1063/1.1901822 (2005).
- 14 Liu, F., Wang, K. L., Li, C. & Zhou, C. W. Study of random telegraph signals in single-walled carbon nanotube field effect transistors. *Ieee T Nanotechnol* **5**, 441-445, doi:Doi 10.1109/Tnano.2006.880906 (2006).
- 15 Liu, F., Bao, M. Q. & Wang, K. L. Determination of the small band gap of carbon nanotubes using the ambipolar random telegraph signal. *Nano Lett* **5**, 1333-1336, doi:Doi 10.1021/NI050578c (2005).
- 16 Liu, F. & Wang, K. L. Correlated random telegraph signal and low-frequency noise in carbon nanotube transistors. *Nano Lett* **8**, 147-151, doi:Doi 10.1021/NI0722774 (2008).
- 17 Liu, F., Bao, M. Q., Wang, K. L., Zhang, D. H. & Zhou, C. W. Coulomb attractive random telegraph signal in a single-walled carbon nanotube. *Phys Rev B* **74**, doi:Artn 035438 Doi 10.1103/Physrevb.74.035438 (2006).
- 18 Kamimura, T., Hayashi, H. & Matsumoto, K. in *Control of Single-Hole Transition in Carbon Nanotube Transistor with Quantum Dot in Gate Insulator at Room Temperature* (ed S. Suzuki) (InTech, 2013).
- 19 Ralls, K. S. *et al.* Discrete Resistance Switching in Submicrometer Silicon Inversion-Layers - Individual Interface Traps and Low-Frequency (1-F Questionable) Noise. *Phys Rev Lett* **52**, 228-231, doi:DOI 10.1103/PhysRevLett.52.228 (1984).
- 20 Wang, N. P., Heinze, S. & Tersoff, J. Random-telegraph-signal noise and device variability in ballistic nanotube transistors. *Nano Lett* **7**, 910-913, doi:Doi 10.1021/NI062742h (2007).
- 21 Kong, J., LeRoy, B. J., Lemay, S. G. & Dekker, C. Integration of a gate electrode into carbon nanotube devices for scanning tunneling microscopy. *Appl Phys Lett* **86**, doi:Artn 112106 Doi 10.1063/1.1883301 (2005).
- 22 Sharf, T., Kevek, J. W., DeBorde, T., Wardini, J. L. & Minot, E. D. Origins of Charge Noise in Carbon Nanotube Field-Effect Transistor Biosensors. *Nano Lett* **12**, 6380-6384, doi:Doi 10.1021/NI303651t (2012).
- 23 Minot, E. D. *et al.* Carbon nanotube biosensors: The critical role of the reference electrode. *Appl Phys Lett* **91**, doi:Artn 093507 Doi 10.1063/1.2775090 (2007).

- 24 Kittel, C. *Introduction to solid state physics*. (John Wiley & Sons, Inc., 2005).
- 25 Purewal, M. S. *et al.* Scaling of resistance and electron mean free path of single-walled carbon nanotubes. *Phys Rev Lett* **98**, doi:Artn 186808 Doi 10.1103/Physrevlett.98.186808 (2007).
- 26 Clement, N., Nishiguchi, K., Fujiwara, A. & Vuillaume, D. One-by-one trap activation in silicon nanowire transistors. *Nat Commun* **1**, doi:Artn 92 Doi 10.1038/Ncomms1092 (2010).
- 27 Wang, N. P. & Xu, X. J. Channel-length scaling for effects of single defects in carbon nanotube transistors. *J Appl Phys* **114**, doi:Artn 073701 Doi 10.1063/1.4818604 (2013).

CHAPTER 5

Concluding discussion

The unifying theme of this work is the physical origins of electronic noise in carbon nanotube field-effect transistors (CNT FETs) operating in liquid environments. To probe electronic noise sources, we utilized the micro-fabrication techniques described in Chapter 2 to control the environment of single, individual semiconducting CNTs. The fabrication geometries include both free-standing suspended CNT circuits and substrate-bound CNT circuits. Whereas conventional fabrication techniques produce CNT circuits that are coated with polymer and chemical processing residues, we have created CNTs with pristine surfaces. We also implemented a microfluidic ‘lab-on-a-chip’ interface to control the interaction of biological and biochemical molecules to CNTs. These techniques provide a methodology to determine the dominant electronic noise sources observed in CNT FETs, as describes in Chapter 3.

Suspended CNT FETs provide an ideal platform to study the intrinsic electronic noise present in physiological environments. In Chapter 3, we utilize the charge noise model as a framework to quantify the intrinsic electronic noise generated by CNT FETs in various physiological environments. Pristine CNT devices were characterized using non-contact scanning photocurrent microscopy, which identified single CNT circuits and avoided surface contamination that is commonly associated with scanning electron microscopy techniques. The pristine structure of these devices was verified by the absence of the defect peak in the Raman response. Measurements of baseline ‘intrinsic’ electronic noise of pristine suspended CNT FETs were performed in liquid environments. Subsequent measurements were performed to systematically control the material interface of CNT FETs. These include the individual and combined effects of the insulating substrate and surface adsorbate interactions with the CNT sidewall. These experimental results reveal that insulating substrates and surface adsorbates generate significant contributions to the electronic noise floor of CNT FETs, which are critical parameters in the design consideration of biosensing platforms.

The microscopic origins of charge noise have been empirically linked to fluctuating charge traps at the CNT-dielectric interface that produce the ubiquitous $1/f$ electronic noise. However, the $1/f$ noise observed in suspended CNTs operating in liquid cannot be explained by charge traps in the dielectric, since the semiconducting channel does not come in contact with an insulating substrate. Therefore, measurements were performed to further investigate the microscopic origins of noise by docking biomolecules to the sidewall of a CNT.

Biomolecular adsorbates were shown to significantly impact the electronic noise floor of pristine CNT FETs. The magnitude of this noise was found to be comparable to the noise generated by substrate interactions with a CNT. These results reveal that biological molecules and polymer adsorbates form a new class of interface charge traps with the CNT.

Both insulating substrates and biomolecules contain weak acid/base groups on their surfaces that capture protons from solution. The charge density of their surfaces is pH dependent. The sensing response of a pristine CNT FET to a change in solution pH showed a dramatic increase after the adsorption of biomolecules to its surface. Similar pH sensitivities were observed with CNTs bound to silanol containing substrates. Both of these effects were linked to larger electronic noise. Polymer residues from photoresist were shown to increase the electronic noise, but reduce the CNT's sensing response to a pH change. We speculate that there may be a link to the fluctuating protonation state of chemical moieties near the CNT.

In Chapter 4, we studied individual charge traps interacting with CNT FETs, in contrast to earlier chapters in which ensembles of electrostatic fluctuators were investigated. We present experimental and theoretical results for charge fluctuations that occur less than ~ 3 nm from the sidewall of a CNT FET in a liquid environment. These electrostatic fluctuations produce random telegraph signals (RTS) in the constant-bias current. Measurements performed on both suspended and substrate-bound CNTs showed that the dielectric substrate is

responsible for the observed RTS. The magnitude of the RTS fluctuations are not consistent with doping effects, but are instead governed by scattering probabilities. Theoretical simulations show that signals generated by a fluctuating charge approaching less than ~ 3 nm from the sidewall of a CNT result in significant scattering of free carriers. The electrostatic fluctuations produce current fluctuations that are not proportional to the transconductance as predicted by the doping mechanism. The experimental and theoretical work discussed in this section present a path to designing optimal single-molecule bioelectronic sensors, eliminating charge traps for high performance switching applications, and offering a platform upon which to study the dynamics of single-charge fluctuations at room temperature.

In summary, the experiments discussed in this work map out the sensitivity limits for CNT FETs functioning as biological probes. This new technology is a promising platform to aid in the investigation of a wide range of biological questions, ranging from the interactions of single molecules to the behavior of cells. Nanometer-scale field effect transistors, such as the CNT, have the potential to transition from the ‘proof-of-concept’ demonstrations highlighted in this work and a large body of additional scientific literature, to a broadly accessible ‘biological-tool-kit’ that can contribute to the life sciences and biomedical community at large.

Education

University of California Santa Barbara	B.S.	2008	Physics
Oregon State University	Ph.D.	2014	Physics

Experience

2009-2014 Oregon State University Corvallis, OR

Graduate research assistant: Minot group

- ❖ Developed microfluidic delivery system to investigate mass transport to nanoelectronic biosensors.^{1,4}
- ❖ Design and fabrication suspended carbon nanotube transistors.^{2,3,5,8,9,10}
- ❖ Graphene bioelectronics.⁷
- ❖ Single-molecule interfaces with carbon nanotube bioelectronics.¹⁰

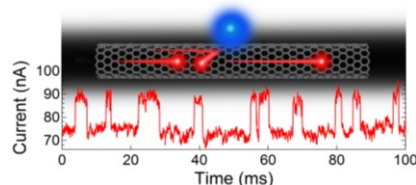
2008-2009 University of California Santa Barbara Santa Barbara, CA

Undergraduate researcher: Ahlers group

- ❖ Heat transport during the onset of turbulence in high Prandtl number fluids.

Publications

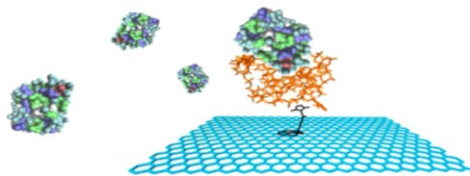
- (10) [T. Sharf](#), N.P. Wang, J.W. Kevek, H. Wilson, S. Heinze, and E.D. Minot, 'Single electron charge sensitivity of liquid-gated carbon nanotube transistors', just accepted *Nano Letters* (2014)



- (9) T.DeBorde, L. Aspitarte, [T.Sharf](#), J.W. Kevek, and E.D. Minot 'Determining the chiral index of semiconducting carbon nanotubes using photoconductivity resonances', *Journal of Physical Chemistry C*, (2014)

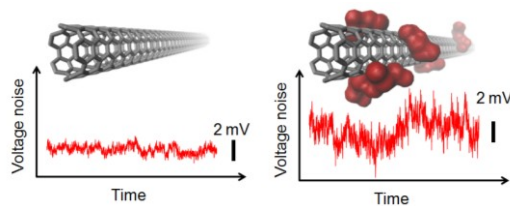
- (8) T.DeBorde, L. Aspitarte, [T.Sharf](#), J.W. Kevek, and E.D. Minot' Photothermoelectric effect in suspended semiconducting carbon nanotubes', *ACS Nano*, 8 (2014)

- (7) G. Saltzgaber, P. Wojcik, [T. Sharf](#), M. R. Leyden, J. L. Wardini, C.A. Heist, A.A. Adenuga, V. T. Remcho, and E.D. Minot, 'Scalable Graphene Field-Effect Sensors for Specific Protein Detection', *Nanotechnology*, 24 (2013)

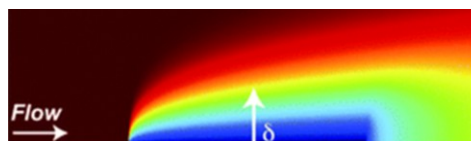


- (6) M. J. Paul, N. A. Kuhta, J. L. Tomaino, A. D. Jameson, L. P. Maizy, [T. Sharf](#), N. L. Rupesinghe, K. B. K. Teo, S. Inampudi, V. A. Podolskiy, E. D. Minot, and Y. S. Lee, 'Terahertz Transmission Ellipsometry of Vertically Aligned Multi-Walled Carbon Nanotubes', *Applied Physics Letters*, 101 (2012)

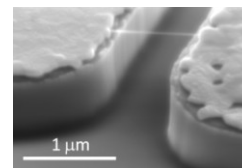
- (5) [T. Sharf](#), J. W. Kevek, T. DeBorde, J. L. Wardini, and E. D. Minot, 'Origins of Charge Noise in Carbon Nanotube Field-Effect Transistor Biosensors', *Nano Letters*, 12 (2012)



- (4) M. R. Leyden, R. J. Messinger, C. Schuman, [T. Sharf](#), V. T. Remcho, T. M. Squires, and E. D. Minot, 'Increasing the Detection Speed of an All-Electronic Real-Time Biosensor', *Lab on a Chip*, 12 (2012)

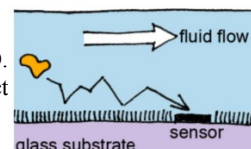


- (3) [T. Sharf](#), J.W. Kevek, and E.D. Minot, 'Fabrication of Low-Noise Carbon Nanotube Field-Effect Transistor Biosensors', *Nanotechnology (IEEE-NANO)*, 11 (2011)



- (2) T. Deborde, J.W. Kevek, [T. Sharf](#) and E.D. Minot, A Spectrally-Tunable Photocurrent Microscope for Characterizing Nanoelectronic Devices', *Nanotechnology (IEEE-NANO)*, 11 (2011)

- (1) M. R. Leyden, C. Schuman, [T. Sharf](#), J. W. Kevek, V. T. Remcho, and E.D. Minot, 'Fabrication and Characterization of Carbon Nanotube Field-Effect Transistor Biosensors', *Proc. of SPIE*, 7779 (2010)



Awards

- ❖ Oregon State University Department of Physics: Outstanding graduate research award (2014)

Conferences attended

- | | | |
|--|------------------|------|
| ❖ IEEE conference on nanotechnology (talk) | Portland, OR | 2011 |
| ❖ APS March meeting (talk) | Boston, MA | 2012 |
| ❖ MSI (poster) | Eugene, OR | 2012 |
| ❖ Biophysical society 57 th annual meeting (poster) | Philadelphia, PA | 2013 |
| ❖ TSRC (invited talk) | Telluride, CO | 2013 |
| ❖ APS March meeting (talk) | Denver, CO | 2014 |
| ❖ INC10 (poster) | Gaithersburg, MD | 2014 |

Collaborative Contributions

- ❖ Todd Squires, **UCSB** chemical engineering – Microfluidics⁵
- ❖ Vincent Remcho, **OSU** chemistry – Microfluidics^{1,5,7}
- ❖ Yun-Shik Lee, **OSU** physics – SEM characterization of carbon nanotubes⁴
- ❖ Stefan Heinze, **University of Kiel** – electron transport measurements¹⁰

Outreach

2010-2014

Summer Experience in Science and Engineering for Youth (SESEY)

- ❖ Mentoring high school youth in the science and development of carbon based nanotechnology and nanoelectronics.

BIBLIOGRAPHY

- Alivisatos, A. P., A. M. Andrews, E. S. Boyden, M. Chun, G. M. Church, K. Deisseroth, J. P. Donoghue, S. E. Fraser, J. Lippincott-Schwartz, L. L. Looger, S. Masmanidis, P. L. McEuen, A. V. Nurmikko, H. Park, D. S. Peterka, C. Reid, M. L. Roukes, A. Scherer, M. Schnitzer, T. J. Sejnowski, K. L. Shepard, D. Tsao, G. Turrigiano, P. S. Weiss, C. Xu, R. Yuste, and X. W. Zhuang. "Nanotools for Neuroscience and Brain Activity Mapping." *Acs Nano* 7, no. 3 (2013): 1850-1866.
- Alivisatos, A. P., M. Y. Chun, G. M. Church, K. Deisseroth, J. P. Donoghue, R. J. Greenspan, P. L. McEuen, M. L. Roukes, T. J. Sejnowski, P. S. Weiss, and R. Yuste. "The Brain Activity Map." *Science* 339, no. 6125 (2013): 1284-1285.
- Alivisatos, A. P., M. Y. Chun, G. M. Church, R. J. Greenspan, M. L. Roukes, and R. Yuste. "The Brain Activity Map Project and the Challenge of Functional Connectomics." *Neuron* 74, no. 6 (2012): 970-974.
- Allen, B. L., P. D. Kichambare, and A. Star. "Carbon Nanotube Field-Effect-Transistor-Based Biosensors." *Advanced Materials* 19, no. 11 (2007): 1439-1451.
- Balasubramanian, K., M. Burghard, K. Kern, M. Scolari, and A. Mews. "Photocurrent Imaging of Charge Transport Barriers in Carbon Nanotube Devices." *Nano Letters* 5, no. 3 (2005): 507-510.
- Briman, M., K. Bradley, and G. Gruner. "Source of 1/F Noise in Carbon Nanotube Devices." *Journal of Applied Physics* 100, no. 1 (2006).
- Bushmaker, A. W., V. V. Deshpande, M. W. Bockrath, and S. B. Cronin. "Direct Observation of Mode Selective Electron-Phonon Coupling in Suspended Carbon Nanotubes." *Nano Letters* 7, no. 12 (2007): 3618-3622.
- Cao, J., Q. Wang, and H. Dai. "Electron Transport in Very Clean, as-Grown Suspended Carbon Nanotubes." *Nature Materials* 4, no. 10 (2005): 745-749.
- Chan, J., B. Burke, K. Evans, K. A. Williams, S. Vasudevan, M. G. Liu, J. Campbell, and A. W. Ghosh. "Reversal of Current Blockade in Nanotube-Based Field Effect Transistors through Multiple Trap Correlations." *Physical Review B* 80, no. 3 (2009).

- Choi, Y. K., I. S. Moody, P. C. Sims, S. R. Hunt, B. L. Corso, I. Perez, G. A. Weiss, and P. G. Collins. "Single-Molecule Lysozyme Dynamics Monitored by an Electronic Circuit." *Science* 335, no. 6066 (2012): 319-324.
- Choi, Y., I. S. Moody, P. C. Sims, S. R. Hunt, B. L. Corso, D. E. Seitz, L. C. Blaszcak, P. G. Collins, and G. A. Weiss. "Single-Molecule Dynamics of Lysozyme Processing Distinguishes Linear and Cross-Linked Peptidoglycan Substrates." *Journal of the American Chemical Society* 134, no. 4 (2012): 2032-2035.
- Choi, Y., T. J. Olsen, P. C. Sims, I. S. Moody, B. L. Corso, M. N. Dang, G. A. Weiss, and P. G. Collins. "Dissecting Single-Molecule Signal Transduction in Carbon Nanotube Circuits with Protein Engineering." *Nano Letters* 13, no. 2 (2013): 625-631.
- Clement, N., K. Nishiguchi, J. F. Dufreche, D. Guerin, A. Fujiwara, and D. Vuillaume. "A Silicon Nanowire Ion-Sensitive Field-Effect Transistor with Elementary Charge Sensitivity." *Applied Physics Letters* 98, no. 1 (2011).
- Clement, N., K. Nishiguchi, A. Fujiwara, and D. Vuillaume. "One-by-One Trap Activation in Silicon Nanowire Transistors." *Nature Communications* 1, (2010).
- Collins, P. G., M. S. Fuhrer, and A. Zettl. "1/F Noise in Carbon Nanotubes." *Applied Physics Letters* 76, no. 7 (2000): 894-896.
- Cui, Y., Q. Q. Wei, H. K. Park, and C. M. Lieber. "Nanowire Nanosensors for Highly Sensitive and Selective Detection of Biological and Chemical Species." *Science* 293, no. 5533 (2001): 1289-1292.
- DeBorde, T., L. Aspirtarte, T. Sharf, J. W. Kevek, and E. D. Minot. "Photothermoelectric Effect in Suspended Semiconducting Carbon Nanotubes." *Acs Nano* 8, no. 1 (2014): 216-221.
- DeBorde, T., L. Aspirtarte, T. Sharf, J. W. Kevek, and E.D. minot. "Determining the Chiral Index of Semiconducting Carbon Nanotubes Using Photoconductivity Resonances." *Journal of physical Chemistry C*, (2014).
- Deshpande, V. V., B. Chandra, R. Caldwell, D. S. Novikov, J. Hone, and M. Bockrath. "Mott Insulating State in Ultraclean Carbon Nanotubes." *Science* 323, no. 5910 (2009): 106-110.

- Dresselhaus, M. S., G. Dresselhaus, R. Saito, and A. Jorio. "Raman Spectroscopy of Carbon Nanotubes." *Physics Reports-Review Section of Physics Letters* 409, no. 2 (2005): 47-99.
- Duan, X. J., R. X. Gao, P. Xie, T. Cohen-Karni, Q. Qing, H. S. Choe, B. Z. Tian, X. C. Jiang, and C. M. Lieber. "Intracellular Recordings of Action Potentials by an Extracellular Nanoscale Field-Effect Transistor." *Nature Nanotechnology* 7, no. 3 (2012): 174-179.
- Franklin, A. D. "Electronics the Road to Carbon Nanotube Transistors." *Nature* 498, no. 7455 (2013): 443-444.
- Franklin, A. D., S. O. Koswatta, D. B. Farmer, J. T. Smith, L. Gignac, C. M. Breslin, S. J. Han, G. S. Tulevski, H. Miyazoe, W. Haensch, and J. Tersoff. "Carbon Nanotube Complementary Wrap-Gate Transistors." *Nano Letters* 13, no. 6 (2013): 2490-2495.
- Gao, R. X., S. Strehle, B. Z. Tian, T. Cohen-Karni, P. Xie, X. J. Duan, Q. Qing, and C. M. Lieber. "Outside Looking In: Nanotube Transistor Intracellular Sensors." *Nano Letters* 12, no. 6 (2012): 3329-3333.
- Goldsmith, B. R., J. G. Coroneus, A. A. Kane, G. A. Weiss, and P. G. Collins. "Monitoring Single-Molecule Reactivity on a Carbon Nanotube." *Nano Letters* 8, no. 1 (2008): 189-194.
- Heering, H. A., K. A. Williams, S. de Vries, and C. Dekker. "Specific Vectorial Immobilization of Oligonucleotide-Modified Yeast Cytochrome C on Carbon Nanotubes." *Chemphyschem* 7, no. 8 (2006): 1705-1709.
- Heller, I., S. Chatoor, J. Mannik, M. A. G. Zevenbergen, C. Dekker, and S. G. Lemay. "Influence of Electrolyte Composition on Liquid-Gated Carbon Nanotube and Graphene Transistors." *Journal of the American Chemical Society* 132, no. 48 (2010): 17149-17156.
- Heller, I., S. Chatoor, J. Mannik, M. A. G. Zevenbergen, J. B. Oostinga, A. F. Morpurgo, C. Dekker, and S. G. Lemay. "Charge Noise in Graphene Transistors." *Nano Letters* 10, no. 5 (2010): 1563-1567.
- Heller, I., A. M. Janssens, J. Mannik, E. D. Minot, S. G. Lemay, and C. Dekker. "Identifying the Mechanism of Biosensing with Carbon Nanotube Transistors." *Nano Letters* 8, no. 2 (2008): 591-595.
- Heller, I., J. Mannik, S. G. Lemay, and C. Dekker. "Optimizing the Signal-to-Noise Ratio for Biosensing with Carbon Nanotube Transistors." *Nano Letters* 9, no. 1 (2009): 377-382.

- Hooge, F. N. "1/F Noise Sources." *Ieee Transactions on Electron Devices* 41, no. 11 (1994): 1926-1935.
- Huang, S. C. J., A. B. Artyukhin, N. Misra, J. A. Martinez, P. A. Stroeve, C. P. Grigoropoulos, J. W. W. Ju, and A. Noy. "Carbon Nanotube Transistor Controlled by a Biological Ion Pump Gate." *Nano Letters* 10, no. 5 (2010): 1812-1816.
- Ishigami, M., J. H. Chen, E. D. Williams, D. Tobias, Y. F. Chen, and M. S. Fuhrer. "Hooge's Constant for Carbon Nanotube Field Effect Transistors." *Applied Physics Letters* 88, no. 20 (2006).
- Javey, A., and J. Kong. *Carbon Nanotube Electronics*: Springer, 2009.
- Jiang, Z., Q. Qing, P. Xie, R. X. Gao, and C. M. Lieber. "Kinked P-N Junction Nanowire Probes for High Spatial Resolution Sensing and Intracellular Recording." *Nano Letters* 12, no. 3 (2012): 1711-1716.
- Jin, S. H., S. N. Dunham, J. Z. Song, X. Xie, J. H. Kim, C. F. Lu, A. Islam, F. Du, J. Kim, J. Felts, Y. H. Li, F. Xiong, M. A. Wahab, M. Menon, E. Cho, K. L. Grosse, D. J. Lee, H. U. Chung, E. Pop, M. A. Alam, W. P. King, Y. G. Huang, and J. A. Rogers. "Using Nanoscale Thermocapillary Flows to Create Arrays of Purely Semiconducting Single-Walled Carbon Nanotubes." *Nature Nanotechnology* 8, no. 5 (2013): 347-355.
- Kamimura, T., H. Hayashi, and K. Matsumoto. *Physical and Chemical Properties of Carbon Nanotubes* Control of Single-Hole Transition in Carbon Nanotube Transistor with Quantum Dot in Gate Insulator at Room Temperature, edited by S. Suzuki: InTech, 2013.
- Kim, W., A. Javey, O. Vermesh, O. Wang, Y. M. Li, and H. J. Dai. "Hysteresis Caused by Water Molecules in Carbon Nanotube Field-Effect Transistors." *Nano Letters* 3, no. 2 (2003): 193-198.
- Kittel, C. *Introduction to Solid State Physics*, Edited by S. Johnson: John Wiley & Sons, Inc., 2005.
- Kong, J., B. J. LeRoy, S. G. Lemay, and C. Dekker. "Integration of a Gate Electrode into Carbon Nanotube Devices for Scanning Tunneling Microscopy." *Applied Physics Letters* 86, no. 11 (2005).
- Kosik, K. S. "Study Neuron Networks to Tackle Alzheimer's." *Nature* 503, no. 7474 (2013): 31-32.
- Larrimore, L. "Chemical and Biological Sensing with Carbon Nanotubes in Solution." Cornell, 2008.

- Lee, J. S., S. Ryu, K. Yoo, I. S. Choi, W. S. Yun, and J. Kim. "Origin of Gate Hysteresis in Carbon Nanotube Field-Effect Transistors." *Journal of Physical Chemistry C* 111, no. 34 (2007): 12504-12507.
- Leyden, M. R., R. J. Messinger, C. Schuman, T. Sharf, V. T. Remcho, T. M. Squires, and E. D. Minot. "Increasing the Detection Speed of an All-Electronic Real-Time Biosensor." *Lab on a Chip* 12, no. 5 (2012): 954-959.
- Leyden, M. R., C. Schuman, T. Sharf, J. W. Kevek, V. T. Remcho, and E.D. Minot. "Fabrication and Characterization of Carbon Nanotube Field-Effect Transistor Biosensors." *Proc. of SPIE* 7779, no. 77790H (2010).
- Lin, Y. M., J. C. Tsang, M. Freitag, and P. Avouris. "Impact of Oxide Substrate on Electrical and Optical Properties of Carbon Nanotube Devices." *Nanotechnology* 18, no. 29 (2007).
- Liu, F., M. Q. Bao, H. J. Kim, K. L. Wang, C. Li, X. L. Liu, and C. W. Zhou. "Giant Random Telegraph Signals in the Carbon Nanotubes as a Single Defect Probe." *Applied Physics Letters* 86, no. 16 (2005).
- Liu, F., M. Q. Bao, and K. L. Wang. "Determination of the Small Band Gap of Carbon Nanotubes Using the Ambipolar Random Telegraph Signal." *Nano Letters* 5, no. 7 (2005): 1333-1336.
- Liu, F., M. Q. Bao, K. L. Wang, D. H. Zhang, and C. W. Zhou. "Coulomb Attractive Random Telegraph Signal in a Single-Walled Carbon Nanotube." *Physical Review B* 74, no. 3 (2006).
- Liu, F., and K. L. Wang. "Correlated Random Telegraph Signal and Low-Frequency Noise in Carbon Nanotube Transistors." *Nano Letters* 8, no. 1 (2008): 147-151.
- Liu, F., K. L. Wang, C. Li, and C. W. Zhou. "Study of Random Telegraph Signals in Single-Walled Carbon Nanotube Field Effect Transistors." *Ieee Transactions on Nanotechnology* 5, no. 5 (2006): 441-445.
- Mannik, J., I. Heller, A. M. Janssens, S. G. Lemay, and C. Dekker. "Charge Noise in Liquid-Gated Single-Wall Carbon Nanotube Transistors." *Nano Letters* 8, no. 2 (2008): 685-688.
- Matthews, B. W. "Determination of Position of Anomalously Scattering Heavy Atom Groups in Protein Crystals." *Acta Crystallographica* 20, (1966): 230-&.

- Minot, E. D., A. M. Janssens, I. Heller, H. A. Heering, C. Dekker, and S. G. Lemay. "Carbon Nanotube Biosensors: The Critical Role of the Reference Electrode." *Applied Physics Letters* 91, no. 9 (2007).
- Muoth, M., T. Helbling, L. Durrer, S. W. Lee, C. Roman, and C. Hierold. "Hysteresis-Free Operation of Suspended Carbon Nanotube Transistors." *Nature Nanotechnology* 5, no. 8 (2010): 589-592.
- Nyquist, H. "Thermal Agitation of Electric Charge in Conductors." *Physical Review* 32, (1928): 110.
- Peng, H. B., M. E. Hughes, and J. A. Golovchenko. "Room-Temperature Single Charge Sensitivity in Carbon Nanotube Field-Effect Transistors." *Applied Physics Letters* 89, no. 24 (2006).
- Petsko, G.A., and D. Ringe. *Protein Structure and Function*: New Science Press, 2004.
- Prisbrey, L., D. Roundy, K. Blank, L. S. Fifield, and E. D. Minot. "Electrical Characteristics of Carbon Nanotube Devices Prepared with Single Oxidative Point Defects." *Journal of Physical Chemistry C* 116, no. 2 (2012): 1961-1965.
- Purewal, M. S., B. H. Hong, A. Ravi, B. Chandra, J. Hone, and P. Kim. "Scaling of Resistance and Electron Mean Free Path of Single-Walled Carbon Nanotubes." *Physical Review Letters* 98, no. 18 (2007).
- Ralls, K. S., W. J. Skocpol, L. D. Jackel, R. E. Howard, L. A. Fetter, R. W. Epworth, and D. M. Tennant. "Discrete Resistance Switching in Submicrometer Silicon Inversion-Layers - Individual Interface Traps and Low-Frequency (1-F Questionable) Noise." *Physical Review Letters* 52, no. 3 (1984): 228-231.
- Rosenblatt, S., Y. Yaish, J. Park, J. Gore, V. Sazonova, and P. L. McEuen. "High Performance Electrolyte Gated Carbon Nanotube Transistors." *Nano Letters* 2, no. 8 (2002): 869-872.
- Saltzgaber, G., P. Wojcik, T. Sharf, M. R. Leyden, J. L. Wardini, C. A. Heist, A. A. Adenuga, V. T. Remcho, and E. D. Minot. "Scalable Graphene Field-Effect Sensors for Specific Protein Detection." *Nanotechnology* 24, no. 35 (2013).
- Sangwan, V. K., V. W. Ballarotto, M. S. Fuhrer, and E. D. Williams. "Facile Fabrication of Suspended as-Grown Carbon Nanotube Devices." *Applied Physics Letters* 93, no. 11 (2008).

- Sharf, T., J. W. Kevek, T. DeBorde, J. L. Wardini, and E. D. Minot. "Origins of Charge Noise in Carbon Nanotube Field-Effect Transistor Biosensors." *Nano Letters* 12, no. 12 (2012): 6380-6384.
- Sharf, T., J.W. Kevek, and E.D. Minot. "Fabrication of Low-Noise Carbon Nanotube Field-Effect Transistor Biosensors." *Nanotechnology (IEEE-NANO), 2011 11th IEEE Conference on* 11, (2011): 122-125.
- Shulaker, M. M., G. Hills, N. Patil, H. Wei, H. Y. Chen, H. S. PhilipWong, and S. Mitra. "Carbon Nanotube Computer." *Nature* 501, no. 7468 (2013): 526-+.
- Sims, P. C., I. S. Moody, Y. Choi, C. J. Dong, M. Iftikhar, B. L. Corso, Q. T. Gul, P. G. Collins, and G. A. Weiss. "Electronic Measurements of Single-Molecule Catalysis by Camp-Dependent Protein Kinase A." *Journal of the American Chemical Society* 135, no. 21 (2013): 7861-7868.
- Sorgenfrei, S., C. Y. Chiu, R. L. Gonzalez, Y. J. Yu, P. Kim, C. Nuckolls, and K. L. Shepard. "Label-Free Single-Molecule Detection of DNA-Hybridization Kinetics with a Carbon Nanotube Field-Effect Transistor." *Nature Nanotechnology* 6, no. 2 (2011): 125-131.
- Steele, G. A., G. Gotz, and L. P. Kouwenhoven. "Tunable Few-Electron Double Quantum Dots and Klein Tunnelling in Ultraclean Carbon Nanotubes." *Nature Nanotechnology* 4, no. 6 (2009): 363-367.
- Strano, M. S., C. B. Huffman, V. C. Moore, M. J. O'Connell, E. H. Haroz, J. Hubbard, M. Miller, K. Rialon, C. Kittrell, S. Ramesh, R. H. Hauge, and R. E. Smalley. "Reversible, Band-Gap-Selective Protonation of Single-Walled Carbon Nanotubes in Solution." *Journal of Physical Chemistry B* 107, no. 29 (2003): 6979-6985.
- Tersoff, J. "Low-Frequency Noise in Nanoscale Ballistic Transistors." *Nano Letters* 7, no. 1 (2007): 194-198.
- Wang, N. P., S. Heinze, and J. Tersoff. "Random-Telegraph-Signal Noise and Device Variability in Ballistic Nanotube Transistors." *Nano Letters* 7, no. 4 (2007): 910-913.
- Wang, N. P., and X. J. Xu. "Channel-Length Scaling for Effects of Single Defects in Carbon Nanotube Transistors." *Journal of Applied Physics* 114, no. 7 (2013).
- Wang, Z. H., J. Wei, P. Morse, J. G. Dash, O. E. Vilches, and D. H. Cobden. "Phase Transitions of Adsorbed Atoms on the Surface of a Carbon Nanotube." *Science* 327, no. 5965 (2010): 552-555.

Xu, Y. Q., A. Barnard, and P. L. McEuen. "Bending and Twisting of Suspended Single-Walled Carbon Nanotubes in Solution." *Nano Letters* 9, no. 4 (2009): 1609-1614.

APPENDICES

Appendix A. PMMA transfer of aligned CNTs

Figure A.1 illustrates how aligned CNTs can be transferred from one substrate to another using the poly(methyl methacrylate) (PMMA) assisted technique.

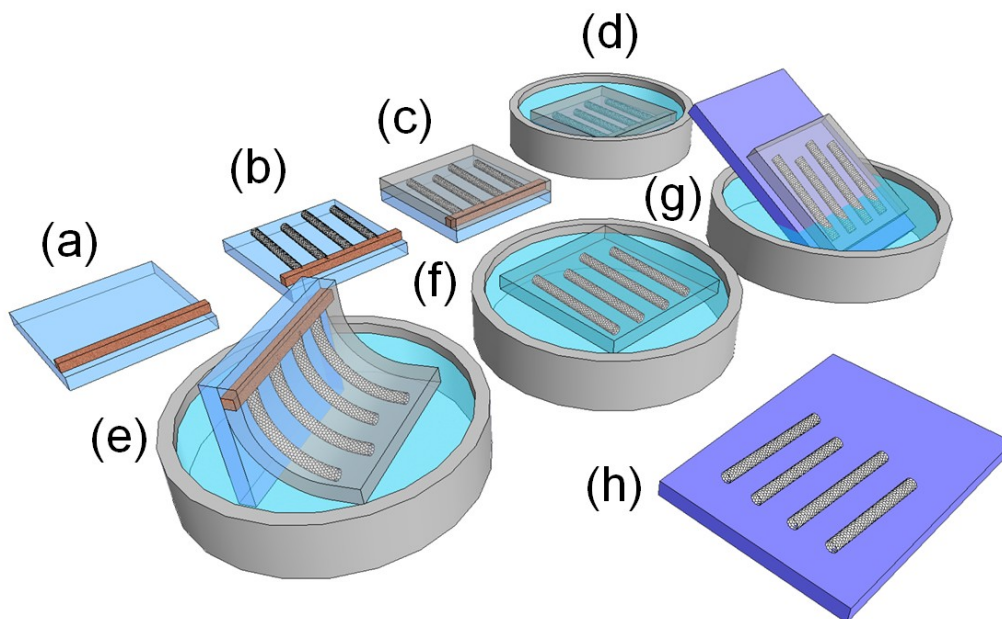


Figure A.1. (a) ST-cut quartz substrate (Hoffman materials) with Fe catalyst deposited perpendicular to the X-crystal axis. (b) CNT growth aligned to the ST-cut quartz. The CNTs grow parallel to the X-axis of the ST cut quartz. (c) PMMA film applied to the quartz wafer with aligned CNTs. (d) chip submerged in 50 mg/mL solution of KOH (99.99% purity from Alpha Aesar) at 80 C. (e) The PMMA film will separate from the underlying quartz wafer when submerged into a DI H₂O water bath at an angle ~ 45 degrees with respect to the water surface. (f) The PMMA film containing the aligned CNTs is shown floating on the water. (g) A Si/SiO₂ wafer is used to scoop up the PMMA film. (h) Aligned carbon nanotubes are left behind after removing the PMMA film with acetone vapor.

Preparation of ST-cut quartz substrate

First ~ 1 nm e-gun deposited Fe was patterned perpendicular to the X-axis of 3" ST-cut quartz wafers (Hoffman materials, wafer flat specified to be parallel to X-axis). The chips were diced ($\sim 0.5'' \times 0.7''$ rectangles work well) so they could be loaded into a 1" tube furnace (see Figure A.1.a). It is important to coat the quartz wafer in photoresist (S1813) prior to dicing to keep the surfaces clean. After dicing the chips, the photoresist should be stripped in PG remover at 70 C for ~ 12 hours.

Growth of aligned CNTs

The CNT aligned growth process is illustrated in Figure A.1.b. (see Xiao *et al.*¹ for details about the aligned growth of CNTs on ST-cut quartz) After dicing and stripping the protective photoresist layer, the quartz chips containing Fe catalyst were loaded into a 1" tube furnace with the quartz X-axis parallel to the direction of gas flow and annealed in open air at 900 C for 60 minutes. The chip was then cooled to room temperature. The furnace tube was then sealed, and purged for ~ 2 minutes flowing the CNT growth gases (0.45 slm H₂, 0.3 slm Ar bubbled methanol, 0.15 slm Ar bubbled ethanol). The tube was then flushed with 1 slm Ar for ~ 2 minutes to clear the growth gases from the chamber. The furnace was then ramped to and held at 800 C and for 15 minutes flowing 0.45 slm of H₂ to reduce the Fe catalyst on the substrate. The furnace was then ramped to 900 C in 0.45 slm H₂. The furnace was then held at 900 C for 15 minutes flowing CNT growth gases. The chip was then cooled under flowing Ar at 1 slm, and opened to atmosphere once the tube furnace reached below 200 C. This recipe produces density ~ 1 CNT per micron with Fe catalyst stripes 10 μm wide spaced at a 50 μm pitch.

PMMA CNT transfer process

Quartz chips containing aligned CNTs were then coated with a PMMA (4% 950 MW PMMA in anisole supplied by Microchem) using a spin coater

(4000 RPM for 60 seconds). PMMA covered CNTs on quartz are shown in Figure A.1.c. The PMMA film must be cut along the border of the substrate to allow it to easily detach from the quartz substrate in the next step. It is best to use a surgical scalpel and cut lines around the perimeter of the chip (~ 1 mm in from the edge of the quartz substrate). Also, cutting an additional diagonal notch on one of the corners helps to keep track of the orientation of the aligned CNTs. Next, place the PMMA coated chip in a bath of KOH (5 mg/mL) at 80 C for ~ 15 minutes as shown in Figure A.1.d. Remove the chip from the KOH bath and transfer it into a water bath at an angle of 45 degrees as shown in Figure A.1.e. The PMMA should separate easily from the underlying quartz substrate and float on the surface water (Figure A.1.f). The PMMA separation process is finicky. Gaining control of this technique requires practice and experience to gain a physical sense of what the PMMA film can handle. The PMMA film may not initially separate when entering the water bath, and will need to soak longer in the KOH solution; in some cases a 30 minute soak is required. Once the PMMA film is floating in the water bath, a piece of silicon can be used to transfer the PMMA film to a next water bath. Placing an extra pair of tweezers in the liquid near the floating PMMA film can help guide the PMMA using surface tension to a desired spot on the chip. Finally, scoop up the PMMA film with the final target substrate (Figure A.1.g) and N₂ blow dry all the water off the surface of the PMMA. This step should help smooth the film surface as the underlying water is displaced from the PMMA-substrate interface. The film should form a nice even color due to thin film interference effects

PMMA removal with acetone vapor

To remove the PMMA, bring acetone to a light boil over a hot plate (300 C works well) using a small beaker (slightly larger than the substrate). Gently lower your chip over the beaker (PMMA side facing the acetone) so that acetone vapor begins to condense on the chip surface. Gently increase the condensation rate so that the PMMA is completely dissolved from the substrate. If the vapor

condenses too rapidly, the film will dissolve too rapidly and the CNTs will not stick to your substrate. Once the PMMA is gone, lower the chip face side up into the acetone. Remove the chip from the acetone (do not let acetone dry on the chip) and spray with IPA and blow dry promptly with N₂. This process preserves the initial CNT alignment as shown in Figure A.1.h.

Fabricating a CNT top-gate using the PMMA transfer process

Figure A.2.a shows a diagram of a top-gate CNT device fabricated using the PMMA transfer process outlined above. First, ~2 nm of e-gun deposited Fe was patterned on Si/SiO₂ substrates with 500 nm of thermal oxide (Nova Electronics), with an area of 5 μm by 10 μm. Carbon nanotubes were then grown by chemical vapor deposition (1" tube furnace) using the following recipe. (1) 600 C open air anneal. (2) 5 minute H₂ (0.45 slm) anneal at 800 C. 5 minute CNT growth at 900 C flowing 0.45 slm H₂, 0.3 slm Ar bubbled methanol, 0.15 slm Ar bubbled ethanol. Electrodes were then patterned with 10 μm x 15 μm source-drain contacts (1 nm Cr / 30 nm Au) with a channel separation of 4 μm. This recipe produced ~ 10 % single CNT devices as measured by AFM.

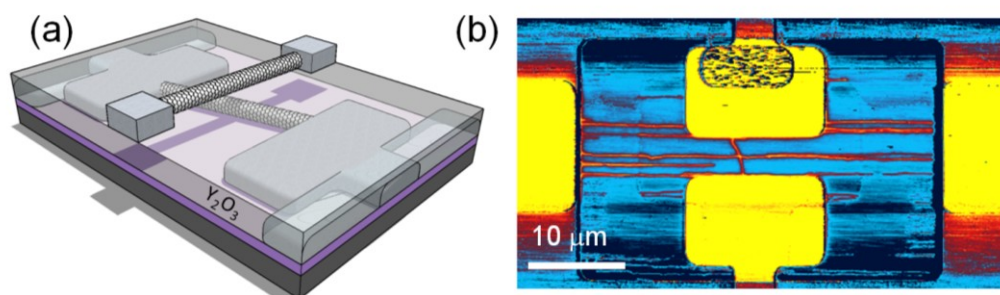


Figure A.2. (a) Diagram of a CNT top-gate placed over a CNT FET buried in Y₂O₃. (b) Image of a CNT top-gate device measured by AFM using EFM mode. The conductive Au electrodes are shown in yellow. The PMMA transferred CNTs are shown as red horizontal lines. The Y₂O₃ (~ 5 nm) buried CNT FET is shown as the vertical red line in between the source-drain contacts. The insulating oxide is shown as blue.

Single CNT circuits were then coated with ~ 3 nm of e-gun deposited yttrium (Y) and allowed to oxidize on a hot plate at 180 C for 10 minutes, forming ~ 5 nm of Y_2O_3 (see Wang *et al.*² for gate dielectric properties of Y_2O_3 coated CNTs). Aligned CNTs were transferred perpendicular to the source-drain electrodes using the method outlined above. Top-gate electrodes were then patterned (~ 2 nm Cr / 30 nm Au). A protective photoresist layer was patterned over the top-gate CNTs and source-drain electrode leads, stray CNTs were then burned off using an O_2 plasma (50 W at 150 mTorr). Figure A.2.b shows a completed CNT-top gate device measured by the AFM using EFM mode. Small source-drain probe pads and CNT top-gate pads make for easy chip design (see Tsai *et al.*³ for top-gate CNT design example). Insulated tungsten probe needles (MicroProbes part # WE30033.0B10) make it possible to directly probe small source-drain and gate electrode pads ($\sim 40\mu\text{m} \times 40\mu\text{m}$) in liquid environments. Electrochemical currents between the liquid gate and insulated MicroProbe needles remain less than 1 nA for liquid-gate voltages required to characterize CNT FETs in liquid.

Appendix B. Lysozyme conjugation to a CNT

Immobilizing proteins to the sidewall of a CNT, while preserving the electronic properties of the CNT is important for high performance biosensing applications. Chen *et al.*⁴ demonstrated that π - π stacking between the sidewall of a CNT and pyrene is strong enough to immobilize proteins to a CNT surface. Besteman *et al.*⁵ demonstrated that the collective activity of proteins functionalized to a CNT sidewall generate a doping effect CNT FETs. Choi *et al.*⁶ showed that by using this method, the catalytic activity of a single enzyme tethered to a CNT side could be observed electronically.³ Below is a protocol for conjugating T4 lysozyme to the sidewall of a CNT adapted from the work of Choi *et al.* and diagrammed in Figure B.1.a.

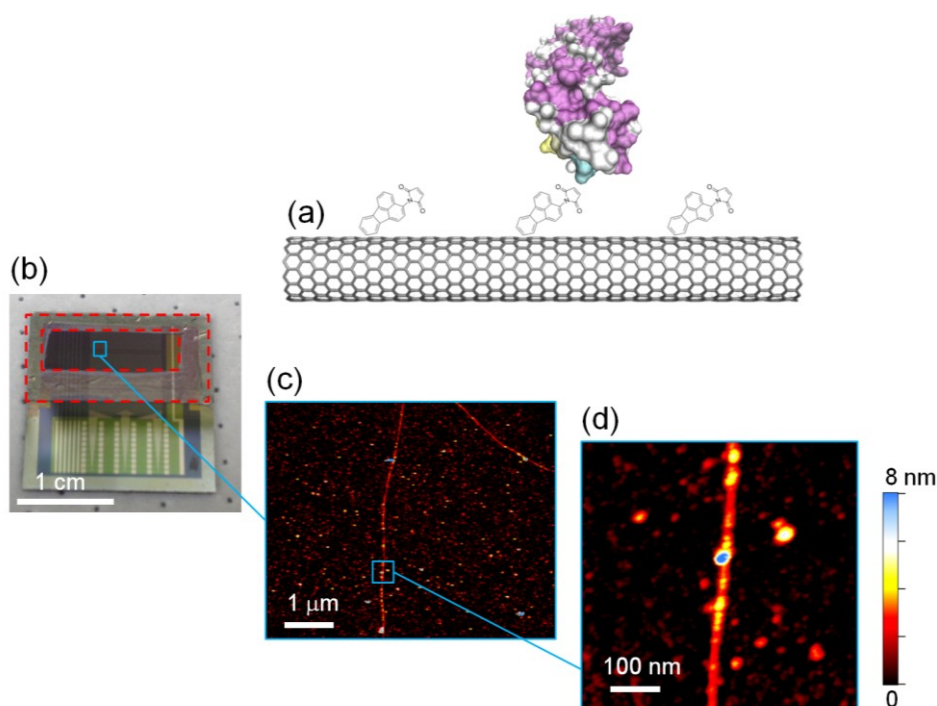


Figure B.1. (a) Diagram of T4 lysozyme conjugated to a CNT using pyrene maleimide linker molecule. (b) Image of a silicon chip containing CNT circuits.

The red dotted lines highlight the parafilm window placed on the chip. The blue square indicated where an active CNT circuit is located. (c) Surface topology map of a CNT taken by AFM after T4 lysozyme conjugation. (d) Zoomed in view of T4 lysozyme with a diameter ~ 9 nm attached to the side wall of a CNT with a diameter ~ 2 nm.

The protocol for conjugating T4 lysozyme to a CNT circuit is listed below.

- (1) Cut out a parafilm window using a surgical scalpel and place over the desired conjugation site as shown in Figure B.1.b. Tweezers work well to press smooth the film down. Place on a hot plate at 115 C for 2 minutes to seat the film. This will create a water reservoir that holds ~ 100 μ l required for the protein incubation step.
- (2) Incubate chip in 1 mM pyrene maleimide in ethanol for 30 minutes without agitation. (3 mg pyrene maleimide / 10 ml ethanol in a 10 ml petri dish)
- (3) Transfer chip to bath (0.1% tween in ethanol) on an orbital shaker for 30 minutes at 110 RPM in 10 ml petri dish. To prepare the tween 20 solution in ethanol, add 40 μ l tween 20 (tween is a viscous liquid) to 40 ml ethanol in a 50 ml centrifuge tube. Place a Teflon coated stir rod in the centrifuge tube and stir at 500 rpm for 5 minutes.
- (4) Transfer chip to bath of 5 ml 0.1% tween in ethanol + 5 ml of 20 mM phosphate buffer (PB) at pH=7.2 on orbital shaker at 100 RPM in 10 ml petri dish
- (5) Transfer chip to water bath (10 ml 18.2 M Ω -cm DI H₂O) shaking at 110 RPM in 10 ml petri dish for 2.5 minutes. Transfer to new water bath and repeat once more.
- (6) Pipette ~ 100 μ l of lysozyme (54 mM in 20 mM PB at pH = 7.2) into parafilm reservoir on chip for a 60 minute incubation. (see p.98 for protein purification protocols)

- (7) Transfer chip to a bath of 10 ml 20 mM PB (pH=7) shaking at 110 RPM in 10 ml petri dish for 2.5 minutes. Transfer to a fresh PB bath and repeat once more.
- (8) Transfer chip to a 10 ml 18.2 MΩ-cm DI H₂O bath shaking at 110 RPM in 10 ml petri dish for 5 minutes. N₂ blow dry to AFM in air. For liquid measurements, exchange the solution in the parafilm reservoir to PB with a pipette.

Protein expression and purity

The Mehl lab at OSU synthesized the s90c lysozyme variant required to tether the protein to pyrene maleimide coated CNTs. The free thiol of the cystein sidechain forms a stable thioether bond with the maleimide group.⁴ The lysozyme variant was expressed in E-coli following the recipe of Choi *et al.*,⁶ using the following amino acid sequence, the s90c mutation is highlighted red.

*MNIFEMLRIDEGRLRLKIYKDTEGYTIGIGHLLTKSPSLNAAKSELDKAIGRNTN
GVITKDEAEKLFNQDVDAAVRGILRNAKLKPVYDCLDAVRRRAALINMVFQMG
ETGVAGFTNSLRMLQQKRWDEAAVNLAKSRYWYNQTPNRAKRVITTFRTGTWD
AYKNLSHHHHHH*

Figure B.2 shows the results of a 15% SDS page gel on the T4 lysozyme s90c variant. The protein was purified in two stages upon extraction from E-coli. First stage used a 5 ml HisTrap column followed by filtration through a superdex 75 column. The gel results show a narrow T4 lysozyme band around the molecular known molecular weight of lysozyme at 18.6 kDa.

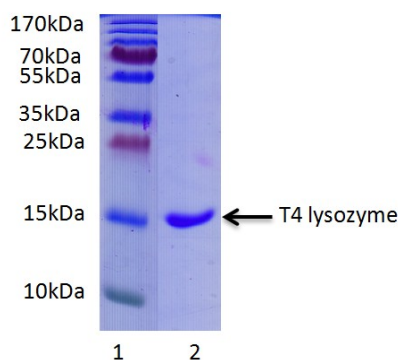


Figure B.2. 15% SDS-PAGE gel run at 180V, stained with Coomassie Blue stain. T4 lysozyme protein is 18.6 kDa. Column 1 shows the thermo pageruler plus molecular weight markers. Column 2 shows the results of the T4 elate after HisTrap and Superdex column purification runs. T4 lysozyme protein has a molecular weight of 18.6 kDa.

Additional protein filtration

Figure B.3 shows conjugation of lysozyme to a CNT chip using standard protein extraction and purification protocol outlined above (p.96). The CNT circuit is shown in Figure B.3.a prior to conjugation, and has a diameter of ~ 1.5 nm as measured by AFM. Figure B.3.b shows an AFM scan of the same after protein conjugation using HisTrap and Superdex column purified lysozyme. The CNT is no longer visible. Figure B.3.c shows an AFM scan taken after the AFM tip was dragged across the surface near the CNT with ~ 70 nN of force using 40 N/m silicon AFM tip (Budget sensors).

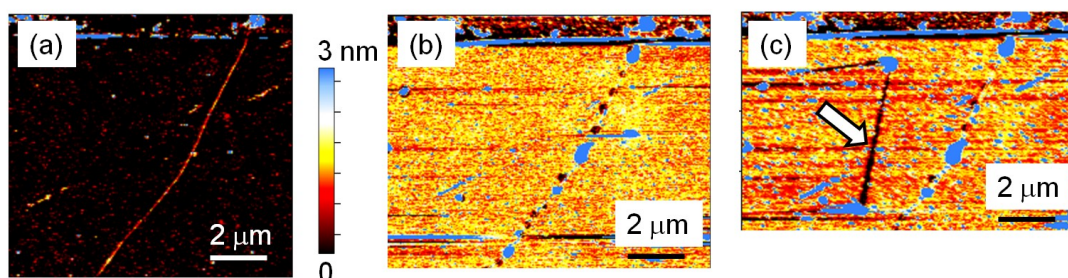


Figure B.3. (a) AFM scan of a CNT before lysozyme conjugation. (b) AFM scan of lysozyme conjugation following Choi *et al.*³ (recipe listed on p.96). Protein has completely coated the CNT. (c) AFM litho scratch (see arrow) near the CNT reveals ~ 1.5 -2 nm film coating the SiO₂ substrate.

The AFM scan reveals that the SiO₂ substrate was coated in ~1.5 – 2 nm film that has buried the CNT. These results suggest that low molecular weight contaminants (~10 kDa and below) remain after both the HisTrap and Superdex column purification steps. These low molecular weight impurities do not show up in the standard SDS- PAGE gel runs (see Figure B.2), and appear to be a major problem for protein conjugation to a CNT. To eliminate the low molecular weight contaminants, lysozyme stock solution (~ 1 ml volume at 2.1 mM lysozyme concentration in 20 mM PB at pH = 7.2) was filtered through a 10 kDa cutoff membrane filter using a centrifuge operating at 7830 RPM. When ~1/2 the volume has been pushed through the filter, PB was added to restore initial volume. Repeat this process atleast 3 times. Do not let all the buffer flush through the filter, otherwise the lysozyme may denature on the membrane surface. After the filtering, reconstitute the solution with PB back to the original volume. This filtering protocol will produce the lysozyme conjugation results shown in Figure B.1.d, and eliminate the non-specific binding of low molecular weight contaminants shown in Figure B.3.c.

Appendix C. Thermolysin conjugation to a CNT

The protocol for conjugating thermolysin to a CNT circuit is listed below.

- (1) Cut out a parafilm window using a surgical scalpel and place over the desired conjugation site as shown in Figure B.1.b. Tweezers work well to press smooth the film down. Place on a hot plate at 115 C for 2 minutes to seat the film. This will create a water reservoir that hold ~ 100 μ l required for the protein incubation step.
- (2) Incubate chip in 1 mM pyrene maleimide in acetonitrile for 30 minutes without agitation. (3mg pyrene maleimide / 10 ml acetonitrile in a 10 ml pyrex petri dish)
- (3) Dunk chip into a new acetonitrile bath.
- (4) Transfer chip to fresh acetonitrile bath (~10 ml) on orbital shaker at 110 RPM for 2 minutes.
- (5) Transfer chip to water bath (10 ml 18.2 M Ω -cm DI H₂O) shaking at 110 RPM in 10 ml petri dish for 2 minutes.
- (6) Pipette ~ 100 μ l of 400 nM thermolysin prepared in incubation buffer (incubation buffer: 10 mM MOPS pH = 7, 5 mM CaCl₂, 500 mM HPLC grade IPA) into parafilm reservoir on chip for a 30 minutes incubation.
- (7) Dunk chip in two separate DI H₂O baths. N₂ blow dry to AFM in air. For liquid measurements, exchange the protein solution in the parafilm reservoir to desired measurement buffer.

Figure C.1 (a-c) shows the results of thermolysin conjugation (p.100 recipe) to a CNT circuit as measured by AFM. Figure C.1.(d-e) show thermolysin binding to the CNT surface using the p.100 recipe, but omitting the addition of

pyrene maleimide in step 2. These results indicate that thermolysin binds non-specifically to the CNT sidewall.

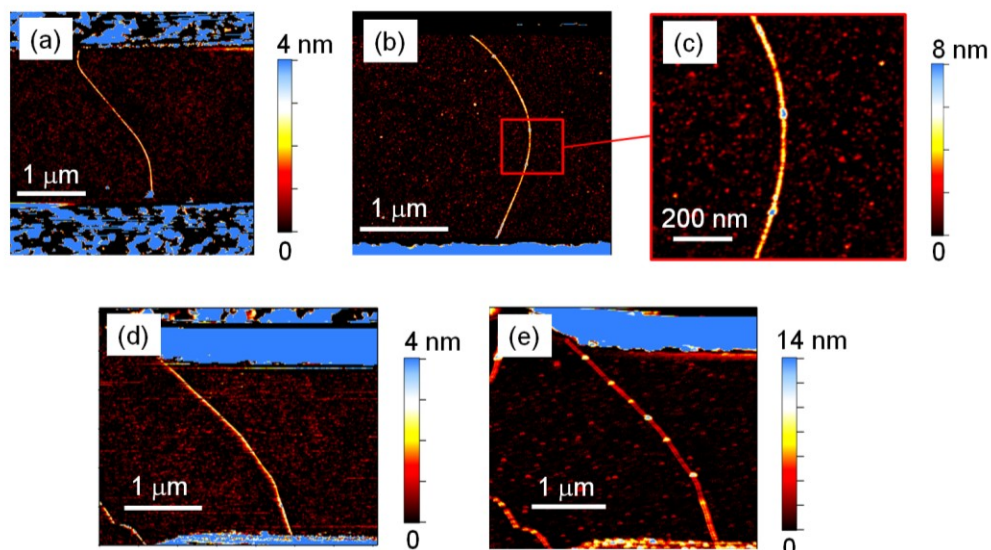


Figure C.1. AFM scans of thermolysin conjugation to a CNT circuit. (a) Clean CNT circuit prior to conjugation. (b) CNT circuit after thermolysin conjugation (recipe p.100), same circuit as (a). (c) Zoomed in scan of CNT decorated with ~ 9 nm diameter thermolysin proteins. (d) Pristine CNT circuit. (e) CNT after thermolysin conjugation (recipe p.100) omitting the pyrene incubation. Protein blobs on the CNT are ~ 9 nm in diameter.

Figure C.2 (a-c) shows the results of thermolysin conjugation (p.100 recipe using $4 \mu\text{M}$ thermolysin concentration for step 6) to a CNT circuit as measured by AFM. The CNT surface and neighboring SiO_2 substrate is coated in a ~ 2 nm film (see Figure C.2.c for an AFM scratch on the contaminating film surface). These results indicate that high concentration protein solutions contain low molecular weight impurities that can contaminate a CNT surface and surrounding substrate.

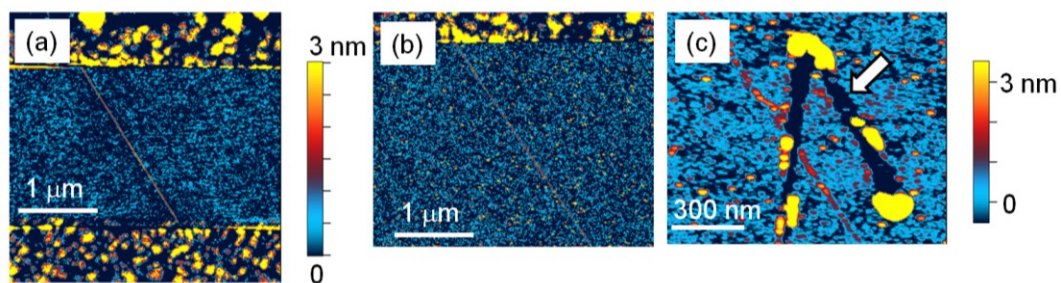


Figure C.2. AFM scans of thermolysin conjugation (p.100 recipe) to a CNT circuit using a 4 μM protein concentration. (a) Clean CNT circuit prior to conjugation. (b) CNT circuit after 4 μM thermolysin incubation. (c) AFM litho scratch (see arrow) near the CNT reveals ~ 2 nm film coating the SiO₂ substrate.

References

- 1 Xiao, J. L. *et al.* Alignment Controlled Growth of Single-Walled Carbon Nanotubes on Quartz Substrates. *Nano Lett* **9**, 4311-4319, Doi 10.1021/Nl9025488 (2009).
- 2 Wang, Z. X. *et al.* Growth and Performance of Yttrium Oxide as an Ideal High-kappa Gate Dielectric for Carbon-Based Electronics. *Nano Lett* **10**, 2024-2030, Doi 10.1021/Nl100022u (2010).
- 3 Tsai, C. L., Xiong, F., Pop, E. & Shim, M. Resistive Random Access Memory Enabled by Carbon Nanotube Crossbar Electrodes. *Acs Nano* **7**, 5360-5366, Doi 10.1021/Nn401212p (2013).
- 4 Chen, R. J., Zhang, Y. G., Wang, D. W. & Dai, H. J. Noncovalent sidewall functionalization of single-walled carbon nanotubes for protein immobilization. *J Am Chem Soc* **123**, 3838-3839, Doi 10.1021/Ja010172b (2001).
- 5 Besteman, K., Lee, J. O., Wiertz, F. G. M., Heering, H. A. & Dekker, C. Enzyme-coated carbon nanotubes as single-molecule biosensors. *Nano Lett* **3**, 727-730, Doi 10.1021/Nl034139u (2003).
- 6 Choi, Y. K. *et al.* Single-Molecule Lysozyme Dynamics Monitored by an Electronic Circuit. *Science* **335**, 319-324, DOI 10.1126/science.1214824 (2012).